EVALUATION OF CRACK TIP SINGULAR FIELDS IN SHAPE MEMORY ALLOYS

by
Gülcan Özerim
B.S., Mechanical Engineering, Boğaziçi University, 2015

Submitted to the Institute for Graduate Studies in
Science and Engineering in partial fulfillment of
the requirements for the degree of
Master of Science

Graduate Program in Mechanical Engineering
Boğaziçi University
2017

EVALUATION OF CRACK TIP SINGULAR FIELDS IN SHAPE MEMORY ALLOYS

APPROVED BY:

Prof. Günay Anlaş (Thesis Supervisor)	.....
Assoc. Prof. C. Can Aydıner	.....
Assist. Prof. Alpay Oral	.....

DATE OF APPROVAL: 24.08.2017

ACKNOWLEDGEMENTS

I would like to express my profound gratitude to my thesis supervisor Prof. Günay Anlaş for his continuous support and very important critiques of this work. I am grateful to his encouragement that always motivated me throughout my master study. I would also like to thank my committee members Assoc. Prof. C. Can Aydıner and Assist. Prof. Alpay Oral for their encouragement and valuable comments.

I am grateful to my colleagues Fatma Mutlu and Onur Yüksel for supporting me every time and their friendship. I especially would like to thank Fatma Mutlu for sharing her valuable experiences with me.

I wish to thank H. Eren Bekiloğlu who always supported and helped me during my study. I would like to thank him very much for his assistance at very critical points in my thesis.

I would also like to thank my friends Adil Han Orta, Gizem Aktaş, Mona Reissi, Nima Shafaghi, Behrouz Haghgouyan, O. Burak Eriçok and Coşkun Bilgin for their supports and helpful discussions.

Finally, I would like to thank my parents for their support and encouragement throughout my study and also to my sisters very precious to me for their love.

ABSTRACT

EVALUATION OF CRACK TIP SINGULAR FIELDS IN SHAPE MEMORY ALLOYS

In this thesis crack tip singular fields of an edge cracked shape memory alloy (SMA) plate under plane stress & Mode I are studied using similarities between loading paths of a pseudoelastic SMA and a strain hardening material. The HRR (Hutchinson-Rise-Rosengren) formulation derived for the crack tip stress field of a strain hardening material is used for the SMAs. The transformation plateau in the stress-strain relation of a pseudoelastic SMA is formulated by Ramberg-Osgood relation which represents the stress-strain relation of a strain hardening material. Crack tip fields of a NiTi compact tension (CT) fracture specimen are evaluated using asymptotic equations of HRR, and they are compared to the results obtained from asymptotic equations of Williams. It is found that the HRR formulation represents better the crack tip conditions in the case of SMAs. In addition, transformation region around the crack tip is evaluated using a phenomenological transformation function of an SMA model together with asymptotic stress equations. The transformation function provided reasonable results for the transformation region size; with the size of the full martensitic region which is better evaluated when HRR method is used. The HRR method is also tested with a CT specimen modeled in ABAQUS using a UMAT that includes thermomechanical coupling. Crack tip fields and transformation region size are compared to the results obtained computationally. It is observed that the crack tip fields in the transformation region of pseudoelastic SMAs can be evaluated reasonably using HRR method. In addition, energy dissipation and the contour dependence of J-integral are studied and the distribution of energy is discussed to complement the study.

ÖZET

ŞEKİL HAFIZALI ALAŞIMLARDA ÇATLAK UCU TEKİL ALANLARIN HESAPLANMASI

Bu tezde gerinim sertleşmesi gösteren malzemeler ile şekil hafızalı alaşımlar (ŞHA) arasındaki benzerliklerden faydalanılarak kenar çatlaklı ŞHA'ların düzlem gerilmesi ve Mod I yükleme altında çatlak ucu tekillik dağılımları incelenmiştir. Gerinim sertliği gösteren malzemelerin çatlak ucu gerilme dağılımını yaklaşık veren HRR yöntemi ŞHA'lar için kullanılmış ve süper elastik özellik gösteren ŞHA'ların gerilim-gerinme grafiğindeki transformasyon platosu gerinim sertleşmesi gösteren malzemeler için kullanılan Ramberg-Osgood denklemi ile gösteril-miştir. NiTi CT (Compact Tension) çatlaklı nümunesinin çatlak ucu alan dağılımları HRR asimtotik denklemleri ile incelenmiş ve sonuçlar Williams'ın asimtotik denklemleri kullanılarak elde edilen sonuçlarla kıyaslanmıştır. ŞHA'larda çatlak ucu dağılımlarının HRR yaklaşımı ile daha doğru yansıtıldığı görülmüştür. Ek olarak, çatlak ucu etrafındaki transformasyon bölgesi ŞHA'larda transformasyonu tanımlayan termodinamik kuvvet denklemi ve asimtotik gerilim denklemleri birlikte kullanılarak çizilmiştir. Transformasyon denklemleri transformasyon bölgesi miktarı için makul sonuçlar vermiş, tam martenzitik bölgenin miktarı ise HRR metod ile daha doğru değerlendirilmiştir. HRR metodun ŞHA'larda kullanılması ayrıca ABAQUS sonlu elemanlar modelinde bir CT çatlaklı numune modellenerek de test edilmiştir. ABAQUS'te ŞHA'ların davranışını modellemek için termomekanik etkileşim içeren bir altprogram (UMAT) kullanılmıştır. Sonlu elemanlar modelinin çatlak ucu alanları ve transformasyon bölgesi için verdiği sonuçlar da asimtotik denklemden elde edilen sonuçlarla kıyaslanmış ve süper elastik ŞHA'larda transformasyon bölgesi içinde çatlak ucu dağılımlarının HRR yöntemi kullanılarak değerlendirilebileceği sonucuna varılmıştır. Konuyu tamamlamak için enerji kaybı ve J integralinin alana bağlı davranışı çalışılmış ve enerjinin paylaşımı tartışılmıştır.

TABLE OF CONTENTS

ACKNOWLEDGEMENTS . . . iii
ABSTRACT . . . iv
ÖZET . . . v
LIST OF FIGURES . . . viii
LIST OF TABLES . . . xv
LIST OF SYMBOLS . . . xvi
LIST OF ACRONYMS/ABBREVIATIONS . . . xix
1. INTRODUCTION . . . 1
1.1. Shape Memory Alloys . . . 1
1.1.1. Pseudoelastic Behavior . . . 4
1.2. Nitinol . . . 6
1.3. Fracture Studies on SMAs . . . 6
1.3.1. Crack Tip Fields . . . 7
1.4. Objectives . . . 11
2. CRACK TIP SINGULARITY . . . 14
2.1. Introduction . . . 14
2.2. Williams' Eigenfunction Solution . . . 14
2.2.1. Stress Intensity Factor, K_I . . . 17
2.3. HRR Formulation . . . 22
2.3.1. Ramberg-Osgood Model . . . 23
2.3.2. Application of Ramberg-Osgood Model to Transformation in SMAs 24
2.3.3. Stress Function Formulation of Hutchinson using Ramberg-Osgood 24
2.3.4. Amplitude of Stress Function . . . 28
3. EVALUATION OF CRACK TIP FIELDS IN SMAs USING HRR . . . 32
3.1. Problem Statement . . . 32
3.2. Evaluation of Mechanical Constants, α and n, of Ramberg-Osgood Equation . . . 33
3.3. Fracture Parameters . . . 37
3.4. Crack Tip Fields . . . 38

3.5. Applicability of HRR Formulation 46
4. EVALUATION OF THE TRANSFORMATION REGION AROUND CRACK TIP 50
4.1. The Transformation Function Governing the Forward Phase Transformation 50
4.2. Calculation of the Transformation Region 53
4.3. Results and Discussion 55
5. COMPUTATIONAL EVALUATION OF CRACK TIP FIELDS AND TRANSFORMATION REGION 59
5.1. Computational Modeling of Tensile Tests Specimen 61
5.2. Computational Modeling of The Edge Cracked Specimen 64
5.2.1. Evaluation of Fracture Parameters 65
5.2.2. Evaluation of Crack Tip Fields 65
5.2.3. Evaluation of Transformation Regions 70
5.2.3.1. The Effect of Thermomechanical Coupling on Transformation Region 72
5.2.4. Sensitivity of Transformation Region Estimation on Mechanical Constant n 74
6. ON J-INTEGRAL AND ENERGY DISSIPATION IN SUPERELASTIC SHAPE MEMORY ALLOYS 77
6.1. Path Independent J Integral 77
6.2. Energy Dissipation in SMAs 82
6.3. Calculation of Energy Dissipation in a Loading-Unloading Cycle 85
6.4. J-Integral and Energy Release Rate 87
7. SUMMARY AND CONCLUSION 93
REFERENCES 97
APPENDIX A: STRESS FUNCTION FORMULATION 103

LIST OF FIGURES

Figure 1.1. Austenite (A) and martensite (M) crystal structure in a Ni-Ti SMA: cubic A on the left and monoclinic M martensite on the right (Only Ti atoms are shown) [1] 1

Figure 1.2. Different variants of martensite in tetragonal lattice [1] 2

Figure 1.3. Stress-temperature diagram of SMAs [2] 3

Figure 1.4. Stress-strain-temperature diagram of an SMA describing shape memory effect [2] 4

Figure 1.5. Pseudoelastic stress-strain diagram [2]. 5

Figure 1.6. Modified stress field as a result of martensitic transformation [3] . 8

Figure 2.1. Notched infinite 2D domain [4] 14

Figure 2.2. Edge cracked plate under tensile loading [5] 18

Figure 2.3. J-integral vs contour number for a nonlinearly elastic material and an SMA 19

Figure 2.4. Opening stress distribution of an SMA ahead of crack tip, $\theta = 0$. 20

Figure 2.5. Irwin's correction to predict the stress distribution in the austenitic region [6] 21

Figure 2.6. Stress-strain relations of non-linearly elastic and elastic-plastic materials [5] 22

Figure 2.7. Ramberg-Osgood type stress-strain relation [7] 23

Figure 2.8. Distribution of the θ dependent parts of stresses for $n = 5$ 27

Figure 2.9. Distribution of the θ dependent parts of stresses for $n = 15$ 27

Figure 2.10. Distribution of the θ dependent parts of the stresses in LEFM . . 28

Figure 2.11. Contour of J around a crack [5] 29

Figure 2.12. I_n vs n [7] 31

Figure 3.1. Geometry of edge cracked specimen 32

Figure 3.2. Stress-strain relation of NiTi [8] 33

Figure 3.3. Stress vs plastic strain in log-log scale 34

Figure 3.4. Stress-strain relation showing the yield offset [9] 35

Figure 3.5. Ramberg-Osgood equation fit to loading path 36

Figure 3.6. Distribution of θ dependent part of stresses for $n = 28$ 37

Figure 3.7. σ_{rr} (MPa) distribution around crack tip using HRR, x is measured from crack tip 39

Figure 3.8. $\sigma_{\theta\theta}$ (MPa) distribution around crack tip using HRR, x is measured from crack tip 40

Figure 3.9. $\sigma_{r\theta}$ (MPa) distribution around crack tip using HRR, x is measured from crack tip 40

Figure 3.10. σ_{eqv} (MPa) distribution around crack tip using HRR, x is measured from crack tip 41

Figure 3.11. Comparison of σ_{rr} (MPa) distribution (HRR vs Williams), x is measured from crack tip 41

Figure 3.12. Comparison of σ_{rr} (MPa) distribution near the crack tip (HRR vs Williams), x is measured from crack tip 42

Figure 3.13. Comparison of $\sigma_{\theta\theta}$ (MPa) distribution (HRR vs Williams), x is measured from crack tip 42

Figure 3.14. Comparison of $\sigma_{\theta\theta}$ (MPa) distribution near the crack tip (HRR vs Williams), x is measured from crack tip 43

Figure 3.15. Comparison of $\sigma_{r\theta}$ (MPa) distribution (HRR vs Williams), x is measured from crack tip 43

Figure 3.16. Comparison of $\sigma_{r\theta}$ (MPa) distribution near the crack tip (HRR vs Williams), x is measured from crack tip 44

Figure 3.17. Comparison of σ_{eqv} (MPa) distribution (HRR vs Williams), x is measured from crack tip 44

Figure 3.18. Comparison of σ_{eqv} (MPa) distribution near the crack tip (HRR vs Williams), x is measured from crack tip 45

Figure 3.19. Comparison of opening stress distribution ahead of the crack tip . 45

Figure 3.20. $\frac{\sigma_{rr}}{\sigma_{\theta\theta}}$ distribution near crack tip according to HRR 47

Figure 3.21. $\frac{\epsilon_{rr}^{pl}}{\epsilon_{rr}^{el}}$ near crack tip, x is measured from crack tip 48

Figure 3.22. $\frac{\epsilon_{\theta\theta}^{pl}}{\epsilon_{\theta\theta}^{el}}$ near crack tip, x is measured from crack tip 49

Figure 3.23. $\frac{\epsilon_{r\theta}^{pl}}{\epsilon_{r\theta}^{el}}$ near crack tip, x is measured from crack tip 49

Figure 4.1. Transformation stresses σ^{MS}, σ^{MF}, σ^{AS} and σ^{AF} 54

Figure 4.2. En of transformation zone ($z = 0$) and size of martensitic region ($z = 1$) estimations using F_z^{HRR} (red points) and F_z^{LEFM} (blue points) 55

Figure 4.3. Volume fraction contours calculated using F_z^{HRR} 56

Figure 4.4. DIC measured contour plot of ϵ_{eqv} [8] 57

Figure 4.5. ϵ_{eqv} distribution around crack tip (HRR vs Williams) 57

Figure 5.1. Dimension (mm) of the dog-bone specimen 61

Figure 5.2. Stress-strain diagram of the 1^{st} material 62

Figure 5.3. Stress-strain diagram of the 2^{nd} material 62

Figure 5.4. Stress-strain diagram of the 3^{rd} material 63

Figure 5.5. Geometry of the finite element model for fracture tests 64

Figure 5.6. Mesh on CT specimen 64

Figure 5.7. Comparison of equivalent stress distribution around the crack tip of the 1^{st} model 66

Figure 5.8. Comparison of equivalent stress distribution around the crack tip of the 2^{nd} model 66

Figure 5.9. Comparison of equivalent stress distribution around the crack tip of the 3^{rd} model 67

Figure 5.10. Comparison of opening stress distribution ahead of the crack tip, 1^{st} model 68

Figure 5.11. Comparison of opening stress distribution ahead of the crack tip, 2^{nd} model 68

Figure 5.12. Comparison of opening stress distribution ahead of the crack tip, 3^{rd} model 69

Figure 5.13. Crack tip dominant zones in an elastic-plastic material [5] 70

Figure 5.14. Crack tip dominant zones in an SMA 70

Figure 5.15. Comparison of the transformation and martensitic regions around the crack tip, 1^{st} model (green lines indicate finite element results) 71

Figure 5.16. Comparison of the transformation and martensitic regions around the crack tip, 2^{nd} model (green lines indicate finite element results) 72

Figure 5.17. Comparison of the transformation and martensitic regions around the crack tip, 3^{rd} model (green lines indicate finite element results) 72

Figure 5.18. Heat flux (mW/mm^2) around the crack tip with $h = 0.05\ W/m^2K$ 73

Figure 5.19. Heat flux (mW/mm^2) around the crack tip with $h = 100\ W/m^2K$ 73

Figure 5.20. Ramberg-Osgood curve fit (solid lines) to stress-strain curve of the second model (dashed line) with different n's 76

Figure 6.1. Closed J-integral contour around a crack tip [5] 78

Figure 6.2. Mesh distribution on edge cracked specimen 79

Figure 6.3. J-integral vs contour number in a linearly elastic material 79

Figure 6.4. J-integral vs contour number in a nonlinearly elastic material . . . 80

Figure 6.5. J-integral vs contour number in an SMA modeled with thermomechanically coupled ZM and uncoupled Auricchio models 81

Figure 6.6. J-integral vs contour number in an elastic-plastic material 82

Figure 6.7. Geometry of NiTi rod modeled in ABAQUS 85

Figure 6.8. Stress-strain diagram of NiTi bar 86

Figure 6.9. Temperature vs time 87

Figure 6.10. Strain energy per unit thickness vs crack length [10] 89

Figure 6.11. Geometry of the edge cracked specimen 90

Figure 6.12. Free energy vs crack length 91

LIST OF TABLES

Table 4.1. Transformation and martensitic region estimations (mm) according to ϵ_{eqv} 58

Table 5.1. Mechanical properties of Nitinol used 59

Table 5.2. Material properties used in the ZM model for the 1^{st} material . . . 60

Table 5.3. Material properties used in the ZM model for the 2^{nd} material . . . 60

Table 5.4. Material properties used in the ZM model for the 3^{rd} material . . . 60

Table 5.5. Fracture parameters 65

Table 5.6. Effect of thermomechanical coupling on transformation region size 74

Table 5.7. Transformation and martensitic region sizes calculated with different n values for the first model ($n = 20$ was used) 75

Table 5.8. Transformation and martensitic region sizes calculated with different n values for the second model ($n = 8$ was used) 75

Table 6.1. Material properties used in the ZM model for the NiTi rod 85

Table 6.2. Energy calculations on the edge cracked specimen with different crack lengths 92

LIST OF SYMBOLS

a	Crack Length
a_e	Effective Crack Length
A	Austenite
A_1, u_{0y}	Rigid Body Parameters
A_f	Austenite Finish Temperature
A_f^0	Austenite Finish Temperature at Zero Stress
A_s	Austenite Start Temperature
B	Specimen Thickness
C_p	Specific Heat Capacity
D	Dissipation
D_1	Intrinsic Dissipation
D_2	Thermal Dissipation
E	Young's Modulus
E_A	Young's Modulus of Austenite
E_M	Young's Modulus of Martensite
F	External Work
F_z	Transformation Function
F_z^{HRR}	Transformation Function with Equations of Hutchinson
F_z^{LEFM}	Transformation Function with Equations of Williams
G	Energy Release Rate
h	Convection Coefficient
I_n	Integration Constant in HRR Solution
J	J-Integral
J^{tip}	J-Integral at Crack Tip
J^{∞}	Far-Field J-Integral
K	Stress Intensity Factor
$\boldsymbol{K}$	Elastic Moduli Tensor
$\boldsymbol{K}_A$	Elastic Moduli Tensor of Austenite

$\boldsymbol{K}_M$	Elastic Moduli Tensor of Martensite
K_I	Mode-I Stress Intensity Factor
M	Martensite
M_f	Martensite Finish Temperature
M_s	Martensite Start Temperature
n	Hardening Coefficient
P	Applied Load
q	Heat Flux
r	Radial Polar Coordinate or Heat Genetation
r_m	Full Martensitic Region Size
r_{tr}	Phase Transformation Region Size
s	Constant Determining Singularity or Entropy Density
S	Deviatoric Stress
T	Temperature
T_0	Reference Temperature
$T-$stress	Stress Component Parallel to Crack Plane
u	Displacement
u_x, u_y	Displacement Field Components
U	Stored (Strain) Energy
V_0	Initial Volume
W	Specimen Width
x, y	Rectangular Coordinates
z	Martensite Volume Fraction
α	Constant Determining Yield-Offset
Γ	$J-$Integral Contour
δ	Kronecker Delta
$\boldsymbol{\epsilon}_A$	Deformation Tensor of Austenite
ϵ_{el}	Elastic Strain
ϵ_{eqv}	Equivalent Strain
$\boldsymbol{\epsilon}_M$	Deformation Tensor of Martensite
ϵ_{MF}	Martensite Transformation Finish Strain

ϵ_{MS}	Martensite Transformation Start Strain
ϵ_{pl}	Plastic Strain
$\boldsymbol{\epsilon}_{tr}$	Orientation Tensor of Martensite
$\epsilon_{xx}, \epsilon_{yy}, \epsilon_{xy}$	Strain Field Components in Rectangular Coordinates
ϵ_y	Yield Strain
$\epsilon_{rr}, \epsilon_{\theta\theta}, \epsilon_{r\theta}$	Strain Field Components in Polar Coordinates
θ	Angular Polar Coordinate
κ	Amplitude of Stress Function
λ	Eigenvalue
μ	Shear Modulus
ν	Poisson's Ratio
π	Pi Number
Π	Potential Energy
ρ	Density
σ^A	Stress in Austenite Region
σ^{AF}	Austenite Transformation Finish Stress
σ^{AS}	Austenite Transformation Start Stress
σ^M	Stress in Martensite Region
σ^{MF}	Martensite Transformation Finish Stress
σ^{MS}	Martensite Transformation Start Stress
σ_{RF}	Orientation Finish Stress
σ_{RS}	Orientation Start Stress
σ_{tr}	Transformation Stress
σ_y	Yield Stress
$\sigma_{xx}, \sigma_{yy}, \sigma_{zz}$	Stress Field Components in Rectangular Coordinates
$\sigma_{rr}, \sigma_{\theta\theta}, \sigma_{r\theta}$	Stress Field Components in Polar Coordinates
$\tau_{xy}, \tau_{xz}, \tau_{yz}$	Shear Stresses
σ^∞	Far-Field Stress
ϕ	Stress Function
ψ	Helmholtz Free Energy

LIST OF ACRONYMS/ABBREVIATIONS

2D	Two Dimensional
3D	Three Dimensional
ASTM	American Society for Testing and Material
CT	Compact Tension
C-D	Clausius Duhem
DIC	Digital Image Correlation
FE	Finite Elements
HRR	Hutchinson-Rise-Rosengren
LEFM	Linear Elastic Fracture Mechanics
NiTi	Nickel Titanium
SMA	Shape Memory Alloy
SME	Shape Memory Effect
ŞHA	Şekil Hafızalı Alaşım
UMAT	User Defined Material Subroutine
ZM	Zaki-Moumni

1. INTRODUCTION

1.1. Shape Memory Alloys

Shape memory alloys (SMAs) are a special group of materials that recover back to their original shapes when subjected to certain loading and temperature. They are mainly present at two different solid phases, namely austenite (A) and martensite (M). These phases differ from each other by their crystal structure which gives them different mechanical properties. Austenite, referred to as the parent phase, is the high temperature phase typically present in a cubic structure; while martensite, the low temperature phase, is in tetragonal, orthorhombic or monoclinic structure as shown in Figure 1.1 [2].

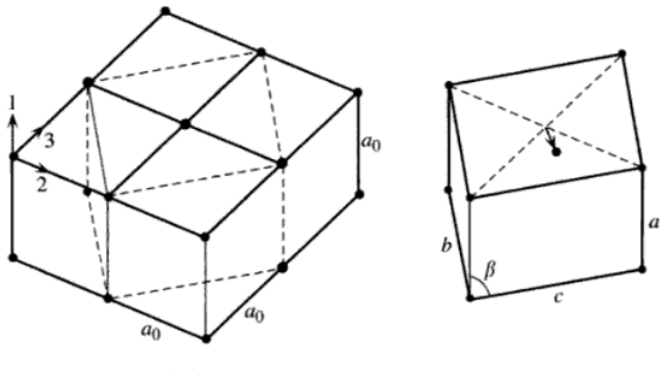

Figure 1.1. Austenite (A) and martensite (M) crystal structure in a Ni-Ti SMA: cubic A on the left and monoclinic M martensite on the right (Only Ti atoms are shown) [1]

In the case of an SMA, the mechanism behind the ability of sustaining large deformation and shape recovery is the solid-to-solid phase transformation called "martensitic phase transformation". The martensitic transformation occurs as a result of a movement of many atoms in the alloy [2, 11]. Each martensitic crystal formed can be oriented in a different direction; called a variant [1, 2].

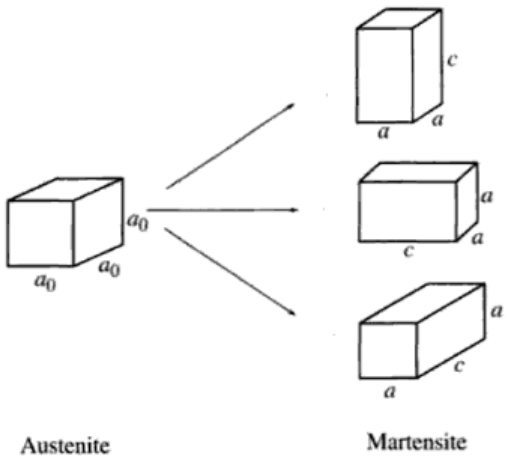

Figure 1.2. Different variants of martensite in tetragonal lattice [1]

Figure 1.2 shows the possible variants of a martensite as a result of transformation from cubic austenite to tetragonal martensite [1]. The martensite that consists of different variants in the lattice is called twinned martensite.

In the absence of loading, martensitic transformation occurs as a result of temperature change. There are four important temperature points in the process which are characteristics of the alloy. The forward transformation, from austenite to martensite, starts with the martensite start temperature (M_s) and completes at the mastensite finish temperature (M_f). Similarly, the reverse transformation, from martensite to austenite, initiates at the austenite start temperature (A_s) and finishes at austenite finish temperature (A_f) [2]. In the case of a martensitic transformation under mechanical loading, transformation stresses are determined by the characteristic temperatures M_s, M_f, A_s and A_f as shown in Figure 1.3.

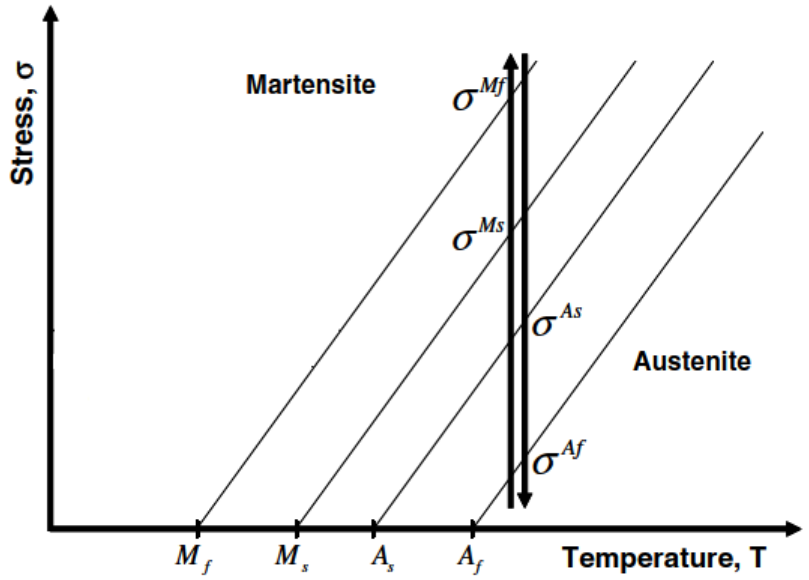

Figure 1.3. Stress-temperature diagram of SMAs [2]

Decreasing temperature below the forward transformation temperatures (M_s and M_f) without loading results in a transformation from austenite to twinned martensite as shown in Figure 1.4. If a mechanical load is applied to the twinned martensite, it is possible to obtain detwinned martensite in which the atoms are oriented in a single direction. If the mechanical loading is released, the detwinned martensite is unloaded elastically. A reverse phase transformation, from martensite to asutenite, is initiated by reincreasing the temperature. The phenomenon described above is called the shape memory effect which enables a complete recovery of the shape.

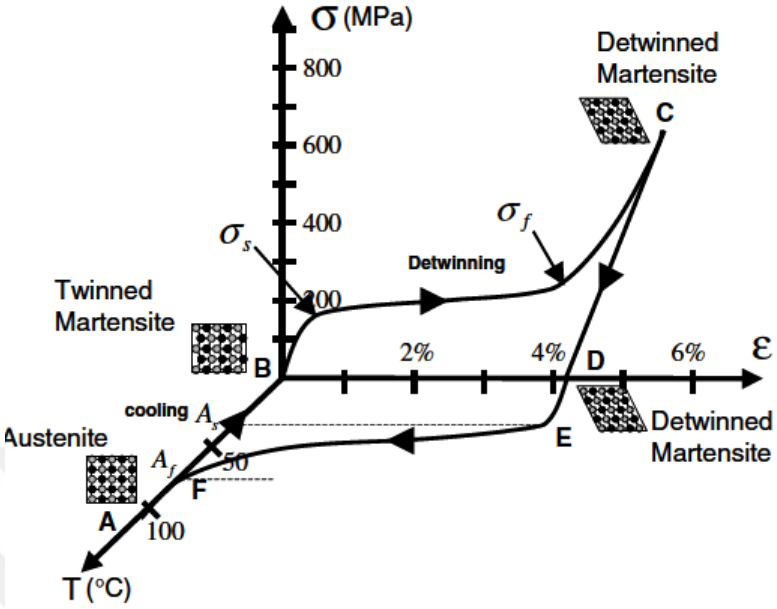

Figure 1.4. Stress-strain-temperature diagram of an SMA describing shape memory effect [2]

The phase transformation under mechanical loading is named pseudoelasticity [2]. In addition to shape recovery, the pseudoelastic behavior enables the sustaining of large amount of deformation. The pseoduelastic loading path of an SMA is explained in the next section.

1.1.1. Pseudoelastic Behavior

Pseudoelasticity is a very interesting behavior of an SMA which makes it desirable in many technological applications. Pseudoelastic SMAs can resist large amount of deformations upon loading. When the load is released, the deformation is recovered and the material goes back to its original shape [2].

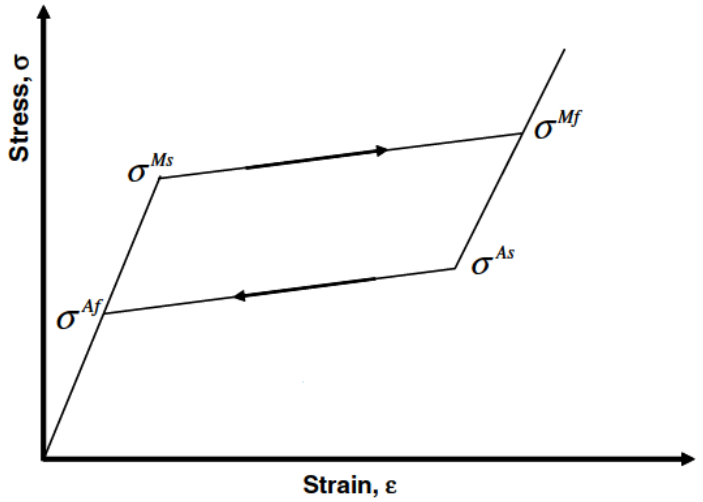

Figure 1.5. Pseudoelastic stress-strain diagram [2].

The pseudoelastic behavior is observed under stress induced transformation of austenite into martensite given that temperature of the material is higher than the austenite finish temperature (A_f). Above A_f, austenite phase starts to be deformed elastically upto a certain stress value after which the phase transformation starts and continues until the full martensite phase is obtained. The stresses indicating the start and the end of the transformation are martensite start (σ^{MS}) and finish (σ^{MF}) stresses. Between these stress levels, the material resists high strain values compared to other engineering materials even though the stress does not increase much. In this region, the slope of the stress-strain curve is very low under quasi-static loading conditions. After σ^{MF}, the material that is in full martensite phase continues to be deformed elastically; further increase in the loading results in plastic deformation of martensite. During the unloading process, the martensite phase initially follows a linear path until austenite start stress (σ^{AS}) is reached; at that point, the reverse transformation initiates, the transformation is completed at a certain stress value which is called the austenite finish stress (σ^{AF}). After σ^{AF}, the austenite phase follows the same path with loading until zero stress is obtained. Although total deformation is recovered, the loading and unloading paths differ from each other as shown in Figure 1.5. For that reason, this behavior is named pseudoelastic, not elastic. In addition, the hysteresis loop indicates that there is some energy dissipation as a result of phase transformation [2].

There is a strong temperature dependence in the mechanical behavior of an SMA. The reason for that is explained by the formation of the transformation strains and the associated work spent for it [2]. Theoretically, a linear relation is shown between the transformation stresses and the temperature with the Clausius-Clapeyron relation [2]. Figure 1.3 shows the relation between stress and temperature relation schematically [2].

1.2. Nitinol

Shape memory alloys are present in Nickel-Titanium, Copper, Iron, Silver and Gold based forms. Among various compositions, Nickel-Titanium (NiTi) based shape memory alloys are widespread [2,12,13]. Shape memory effect (SME) in an equiatomic NiTi alloy is discovered in early 1960s by Buehler and his coworkers [2]. Athough it was expensive, it was highly used due to its strong SME behavior.

Nickel rich Nitinol exhibits pseudoelastic behavior over a wide range of temperature. It is observed that a pseudoelastic NiTi can sustain and recover approximately 8% strain [13]. Important characteristics of NiTi such as SME and pseudoelasticity make it an attractive material in many technological applications. They have a wide range of applications in the aerospace and bio-medical applications. Due to its bio-compatibility and high resistance to corrosion, NiTi is especially preferred in bio-medical applications. NiTi is used predominantly in cardiovascular and orthodontic applications such as dental braces and cardiovascular stents. Because of its important characteristics, the SMA studied in this thesis is also chosen to be a pseudoelastic NiTi.

1.3. Fracture Studies on SMAs

Martensitic phase transformation in SMAs has considerable effects on its fracture behavior. Since the phase transformation starts immediately around the crack tip due to high stresses, the crack tip fields cannot be evaluated using classical methods. In the literature, the number of studies directly on crack tip fields are limited. In most of the studies, transformation region size around the crack tip and its effects on fracture parameters are studied by experimental, numerical or analytical methods but results

still require further discussion and improvement. In the following section, a summary of these studies performed by previous researchers are given.

1.3.1. Crack Tip Fields

Maletta and Furgiuele [6] investigated the extent of the transformation region and the stress distribution around the crack tip analytically neglecting plastic yielding of the martensite phase. They calculated the stress distribution using a piecewise formulation and analyzed the martensitic and austenitic regions separately. In the austenitic region where the material is linearly elastic, the asymptotic stress equation of Williams [14] with Irwin's correction was used:

$$\sigma^A(r) = \frac{K_{Ie}}{\sqrt{2\pi(r-\Delta r)}} \tag{1.1}$$

K_{Ie} is the stress intensity factor calculated as $K_{Ie} = \sigma^\infty\sqrt{\pi a_e}$ and a_e is the effective crack length calculated with Irwin's correction, $a_e = a + \Delta r$. A constant stress is assumed in the transformation region and this limitation is overcome in a later work [15]. Stress distribution in the martensitic region is calculated by using the modified constitutive relations for bilinear materials:

$$\sigma^M = \frac{1}{2(1-\nu)+(\alpha^{-1}-1)}\left[2(1-\nu)\frac{K_{Ie}}{\sqrt{2\pi r}} + (\alpha^{-1}-1)\sigma^{tr} - \epsilon_l E_A\right] \tag{1.2}$$

where $\alpha = \frac{E_M}{E_A}$, ν is the Poisson's ratio, E_A and E_M are the elastic modules of austenite and martensite and ϵ_l is the transformation strain. To use Equations 1.1 and 1.2, transformation region size should be calculated as well. In a later work, Maletta and Furgiuele [16] proposed two different stress intensity factors, K_{IA} and K_{IM}, calculated with stress distributions in the austenitic and martensiteic regions. They compared the values of K_{IA} and K_{IM} normalized by K_I^∞ (stress intensity factor calculated with the far field stress, $K_I^\infty = \sigma^\infty\sqrt{\pi a}$) and observed that the ratio of $\frac{K_{IA}}{K_{I\infty}}$ is always greater than unity while the ratio of $\frac{K_{IM}}{K_{I\infty}}$ is smaller. Because fracture always occurs in the martensitic region, they considered K_{IM} as a more suitable fracture control

parameter. A toughening effect of phase transformation is observed by Maletta and Furgiuele. It was previously noted by Birman [17] that the effect of martensitic phase transformation on stress intensity factor was relatively small. According to his studies, mechanical properties of the austenite is adequate to obtain the stress intensity factor approximately, however stress redistribution due to phase transformation was not included in his study.

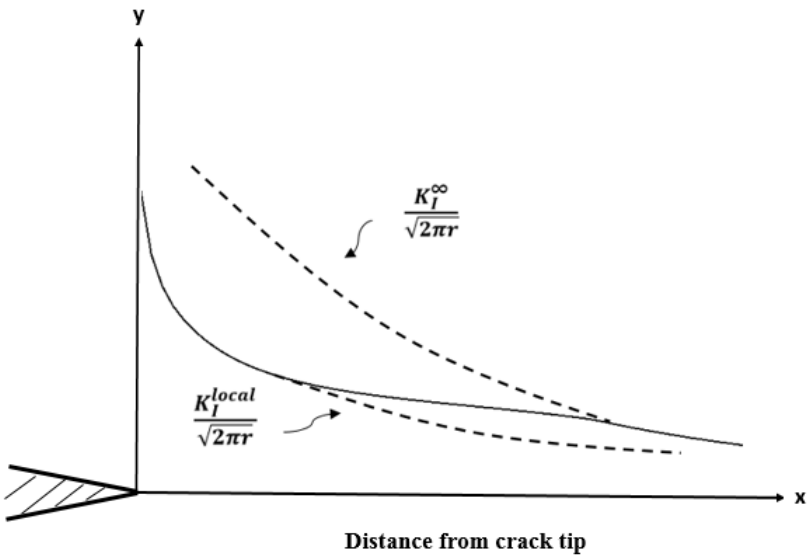

Figure 1.6. Modified stress field as a result of martensitic transformation [3]

Fracture toughening is one of the most important effects of the martensitic phase transformation that is observed by some other researchers as well. this is discussed earlier by McMeeking and Evans [3]. They noted that stress induced martensitic transformation increased the toughness as a result of a residual strain field that restricts crack opening. They showed this effect calculating the change in the stress intensity factor as a result of martensitic transformation using Eshelby's technique, see Figure 1.6. Yi and Gao [18] analytically analyzed the the effect of martensitic transformation on stress intensity of the crack tip. They first observed the shape and the size of the transformation region using Williams' asymptotic stress equations and the constitutive model of Sun and Hwang. Next, they calculated the change in stress intensity factor using Eshelby's inclusion and weight function method. They observed a reduction in the crack tip stress intensity as a result of martensitic transformation around the

crack tip and an increase in toughness. The same effect is also studied by Freed and Banks-Sills [19] numerically. who reported that the energy dissipation results in transformation toughening in SMAs. They calculated the transformation region in a way similar to Yi and Gao using the constitutive model of Panoskaltsis *et al.* and modeled the crack propagation using a cohesive zone model.

Fracture toughening was also observed by Haghgouyan *et al.* [8] in their experimental and computational investigation on fracture behavior of an edge cracked NiTi plate. They compared the critical stress intensity factor calculated for the edge cracked specimen to that of a transformation suppressed NiTi tested at $100°C$. Their results clearly showed the toughening occurred as a result of martensitic transformation.

Baxevanis and Lagoudas [20] studied a center cracked infinite SMA plate under Mode I in which they included phase transformation and plasticity. In their analysis, constant stress and temperature was assumed during phase transformation. Dugdale-Barenblatt model developed for non-hardening elastic-plastic materials was used in a strip like region assumed for the transformation and plastic zones extending along the line of crack. Effective crack length was calculated adding transformed and plastically deformed regions to the physical length of the crack. In Dugdale-Barenblatt model, it is assumed that the crack surfaces are loaded by the remote stress σ^{∞} and also by a normal cohesive traction. These two loadings create the same amount of stress intensity factor of opposite signs. As a result, there is no singularity observed at the crack tip which means stresses are bounded everywhere in the strip-like region.

There are some numerical works on crack tip fields in shape memory alloys: Wang [21] used finite elements to study the evolution of stress-strain and martensitic transformation in front of a notch in a NiTi plate using a phenomenological model developed by Auricchio *et al.* They concluded that the transformation increases the required stress for the plastic deformation in front of the crack tip.

Baxevanis *et al.* [22] worked on crack tip fields for a plane strain problem of a pseudoelastic SMA using phenomenological model of Lagoudas *et al.* in finite elements. The problem was formulated with the boundary layer approach introduced by Rice [23]. A displacement boundary condition was implied on the outer boundary with the displacement field equations associated with the stress intensity factor. They included plastic yielding of the martensite phase near the crack tip; the stress distribution in plastically deformed martensitic region is observed using formulation of Hutchinson for strain hardening materials. In their study, transformation and plastically deformed region boundaries were observed. According to their numerical results, plastic zone size decreases substantially as a result of the phase transformation. They also observed the path-dependence of the J-integral. However, they claimed that the difference between J-integrals calculated on different contours were very small compared to the elastic-plastic materials. Additionally, they observed the effect of the elastic modulus, transformation strain and the temperature on mechanical fields around the crack tip.

Falvo *et al.* [24] also studied the evolution of the martensitic phase transformation near the crack tip in a NiTi alloy. They used the classical LEFM stress intensity factor calculation and the modified version based on Irwin's correction. They concluded that the calculations done with Irwin's correction yielded closer results to the ones they obtained from finite elements.

Hazar *et al.* [25] calculated the transformation region around the crack tip of an SMA plate using asymptotic stress equations of Williams and the transformation function proposed by Zaki and Moumni [26]. They compared the results to experimental, analytical and numerical predictions in the literature for plane stress and plane strain conditions. They stated that, their analytical result gives a reasonable estimate for the shape and the size of the transformation region once the stress intensity factor is calculated properly.

There are some experimental investigations on fracture of pseudoelastic NiTi as well: Wang *et al.* [27] analyzed the fracture behavior experimentally and computationally and calculated the transformation toughness following the procedure described by

ASTM standard E399 [28], and conducted fracture tests using a compact tension (CT) specimen.

Daly *et al.* [29] used digital image correlation (DIC) to observe the strain distribution in an edge cracked thin NiTi under Mode I. They calculated the fracture toughness using an analytic approach based on LEFM and obtained an empirical relation between the stress intensity factor and the transformation region.

Robertson *et al.* [30] used X-ray diffraction to obtain the strain field around the crack tip of an edge cracked thin NiTi under Mode I and observed the crystallography of the transformation zone. In their results, they concluded that stress redistribution as a result of the phase transformation reduces the crack tip stresses and increases the fracture resistance.

Gollerthan *et al.* [31] also performed fracture experiments on a NiTi CT specimen. They calculated the fracture toughness using empirical relation in the form $K = \frac{P}{B\sqrt{W}} f(\frac{a}{W})$ where B, W and $f(\frac{a}{W})$ are calculated according to the ASTM standard [28]. The transformation zone estimation was performed using the calculated stress intensity factor and Irwin's correction.

Mutlu [32] did fracture tests on thin NiTi plates under different loading rates and Mode I. She [32] obtained the displacement field around the crack tip using DIC and used the displacement field in the calculation of the critical stress intensity factor. Transformation region was also evaluated using equivalent strain distribution around the crack tip. Her results showed that thermomechanical coupling observed in the NiTi affects the displacement distribution and the size of the transformation region around the crack tip.

1.4. Objectives

It is clear that crack tip fields need be analyzed in more detail to understand fracture behavior of SMAs. Studies in the literature show that martensitic transformation

in the vicinity of a crack tip has significant effects on the fracture parameters. There has been a number of attempts to evaluate crack tip fields in SMAs using analytical, computational or experimental methods. However, most of them are not capable in representing the exact behavior. In most of the studies, the classical stress intensity factor, K, is used to characterize the crack tip stress field. Although it works properly for linearly elastic materials, it is only possible to characterize a very small region with the stress intensity factor in case of SMAs. Therefore, there is still a need for further analyze on crack tip fields in SMAs.

The aim of this thesis is to investigate the crack tip singular fields of a thin edge cracked SMA plate under Mode I using an analytical model originally developed for elastic-plastic materials. Ramberg-Osgood stress-strain relation for strain hardening materials is used to represent the stress plateau during the martensitic transformation in pseudoelastic SMAs which cannot be represented using linear stress-strain relation. The crack tip fields are analyzed using asymptotic equations of HRR which are derived from the Ramberg-Osgood model. HRR equations are also used to estimate the transformation region around the crack tip. In addition, energy dissipation and path dependence of J-integral are studied to understand the physical interpretation of the J-integral in the SMAs.

The outline of the thesis is as follows: In Chapter 2, the eigenfunction solution of Williams and HRR solution for crack tip singular fields are summarized. For the HRR formulation, first Ramberg-Osgood constitutive relation is presented. In Chapter 3, crack tip fields in a thin edge cracked Nitinol plate under Mode I loading are evaluated by using both asymptotic equations of Williams and HRR. The geometry is chosen to be the same as the one studied experimentally by Haghgouyan *et al.* [8]. A comprehensive comparison of the asymptotic equations are done together with the experimental results, and the application of HRR to SMAs are discussed. In Chapter 4, transformation and full martensitic regions around the crack tip are estimated analytically. The asymptotic stress equations are used together with the phenomenological model proposed by Zaki and Moumni [26]. Additionally, transformation region is evaluated using the equivalent strain and the results are compared to the experimental ones. Chapter

5 is devoted to the computational analysis of the crack tip fields and the phase transformation region using finite elements. Three set of NiTi specimens obtained from Mutlu [32] and Gou [33] are used. Uniaxial tensile and fracture tests are simulated in ABAQUS using a separate UMAT sobroutine written to account for thermomechanical coupling. Computational results are compared to the analytical evaluations obtained in this work. In Chapter 6, path-dependence of J-integral in the SMAs and energy dissipation during the martensitic phase transformation are studied. A computational analysis is performed on an edge cracked SMA plate using thermomechanically coupled ZM model [26] to understand the physical meaning of the J-integral in the SMAs.

2. CRACK TIP SINGULARITY

2.1. Introduction

Stress-strain relations in shape memory alloys are mostly formulated with some phenomenological constitutive models which are then implemented into finite element programs as UMATs. In the study of fracture mechanics, crack tip fields are the focus, and the phase transformation that occurs in the vicinity of the crack that affects the field of interest becomes an important issue as well. In the literature, mostly asymptotic equations of LEFM are used in the evaluation of the crack tip fields [6, 8, 20, 25].

Asymptotic equations of LEFM are developed by Williams [14] as a set of equations to observe the stress distribution around the crack tip of an elastic body. Although it is derived for only linearly elastic materials, Williams' solution constructs a solid base in the analysis of fracture of other types of materials such as non-linearly elastic or elastic-plastic. Using a similar method, Hutchinson [7] analyzed the crack tip fields of elastic-plastic materials. In the following sections, both solutions are presented.

2.2. Williams' Eigenfunction Solution

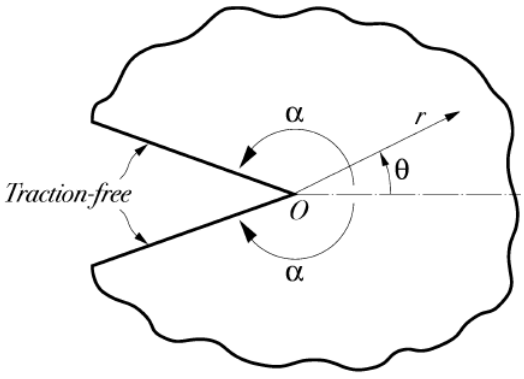

Figure 2.1. Notched infinite 2D domain [4]

Williams [34] analyzed the stress singularity in a notched infinite 2D domain as shown in Figure 2.1, and used an eigenfunction formulation. The cracked medium is a special form of this geometry when $\alpha = \pm\pi$. To analyze the stress field near the crack tip, he proposed a stress function which satisfies the following biharmonic equation:

$$\bigtriangledown^4 \phi = 0 \tag{2.1}$$

where ϕ is the Airy stress function which is related to the stresses in polar coordinates as follows:

$$\begin{aligned} \sigma_{rr} =& \frac{1}{r^2}\frac{\partial^2\phi}{\partial\theta^2} + \frac{1}{r}\frac{\partial\phi}{\partial r} \\ \sigma_{\theta\theta} =& \frac{\partial^2\phi}{\partial\theta^2} \\ \sigma_{r\theta} =& -\frac{1}{r}\frac{\partial^2\phi}{\partial r\partial\theta} + \frac{1}{r^2}\frac{\partial\phi}{\partial\theta} \end{aligned} \tag{2.2}$$

Williams assumed a stress function of the following form:

$$\begin{aligned} \phi &= r^{\lambda+2} f(\theta, \lambda) \\ &= r^{\lambda+2}[A_\lambda cos\lambda\theta + C_\lambda sin\lambda\theta + B_\lambda cos(\lambda+2)\theta + D_\lambda sin(\lambda+2)\theta] \end{aligned} \tag{2.3}$$

where A_λ, B_λ, C_λ and D_λ are constants to be determined and λ's are the eigenvalues of the stress function. Williams' stress function is in a separable form in terms of r and θ. Stress components σ_{rr}, $\sigma_{\theta\theta}$ and $\sigma_{r\theta}$ are derived from the stress function using Equation 2.2, and using the symmetry in the geometry following stresses are obtained:

$$\begin{aligned} \sigma_{\theta\theta} &= (\lambda+1)(\lambda+2)r^\lambda(A_\lambda cos\lambda\theta + B_\lambda cos(\lambda+2)\theta) \\ \sigma_{rr} &= r^\lambda[A_\lambda(\lambda+2) - \lambda^2]cos\lambda\theta + r^\lambda[B_\lambda(\lambda+2)(1-(\lambda+2))]cos(\lambda+2)\theta \\ \sigma_{r\theta} &= (\lambda+1)r^\lambda[A_\lambda\lambda sin\lambda\theta + B_\lambda(\lambda+2)sin(\lambda+2)\theta] \end{aligned} \tag{2.4}$$

It is obvious from Equations 2.4 that λ should be smaller than zero in order to have a stress singularity as r goes to zero. On the other hand, strain energy should be bounded which requires that $\lambda > -1$ should be satisfied as well [4, 5].

In order to find the eigenvalues (λs) of the stress function, boundary conditions are used:

$$\sigma_{\theta\theta} = \sigma_{r\theta} = 0 \quad ; \quad \theta = \pm\pi \tag{2.5}$$

The boundary conditions are only satisfied when:

$$\lambda = 0, \pm\frac{1}{2}, \pm 1, ... \tag{2.6}$$

Therefore, as r goes to zero, the leading term is $\lambda = -\frac{1}{2}$ which yields the famous square root singularity for the stress field near the crack tip. Using the second boundary condition, $\sigma_{r\theta}(\pi) = 0$, the relation $A = 3B$ is obtained, and the stresses took the following form as r goes to zero:

$$\begin{aligned}
\sigma_{\theta\theta} &= \frac{A}{r^{\frac{1}{2}}}[\frac{3}{4}cos\frac{\theta}{2} + \frac{1}{4}cos\frac{3\theta}{2}] \\
\sigma_{r\theta} &= \frac{A}{r^{\frac{1}{2}}}[\frac{1}{4}sin\frac{\theta}{2} + \frac{1}{4}sin\frac{3\theta}{2}] \\
\sigma_{rr} &= \frac{A}{r^{\frac{1}{2}}}[\frac{5}{4}cos\frac{\theta}{2} - \frac{1}{4}cos\frac{3\theta}{2}]
\end{aligned} \tag{2.7}$$

From Equations 2.7, it is observed that all stress components near the crack tip are proportional to a constant, A, which is to be determined.

2.2.1. Stress Intensity Factor, K_I

The constant A in Equations 2.7 is replaced with the stress intensity factor for Mode I, K_I, as follows:

$$A = \frac{K_I}{\sqrt{2\pi}} \tag{2.8}$$

The stress intensity factor determines the amplitude of the crack tip singular stresses which means stress and strain components near the crack tip increase in proportion to K_I. Replacing A with K_I, asymptotic stress equations of Williams are written as follows:

$$\begin{aligned}
\sigma_{rr} &= \frac{K_I}{\sqrt{2\pi r}}\left[\frac{5}{4}cos(\frac{\theta}{2}) - \frac{1}{4}cos(\frac{3\theta}{2})\right] \\
\sigma_{\theta\theta} &= \frac{K_I}{\sqrt{2\pi r}}\left[\frac{3}{4}cos(\frac{\theta}{2}) + \frac{1}{4}cos(\frac{3\theta}{2})\right] \\
\tau_{r\theta} &= \frac{K_I}{\sqrt{2\pi r}}\left[\frac{1}{4}sin(\frac{\theta}{2}) + \frac{1}{4}sin(\frac{3\theta}{2})\right]
\end{aligned} \tag{2.9}$$

To evaluate crack tip fields, K_I should be determined. In a very large edge cracked plate under tensile loading as shown in Figure 2.2, the relation between K_I, remote loading and the geometry is as follows [5]:

$$K_I = \sigma^{\infty}\sqrt{\pi a} \tag{2.10}$$

where a is the half-crack length, W is the width of the cracked plate and σ^{∞} is the remote stress.

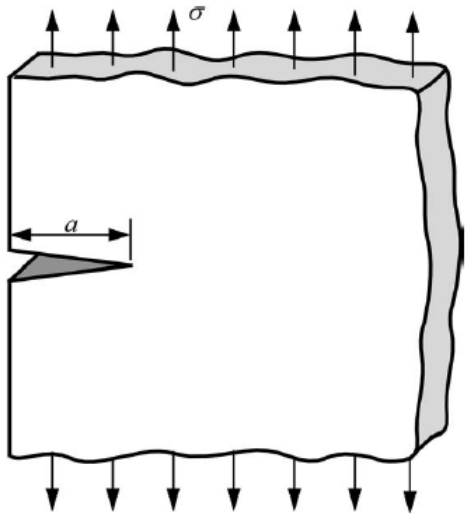

Figure 2.2. Edge cracked plate under tensile loading [5]

All stress intensity factors cannot be evaluated using Equation 2.10. For complex geometries other ways should be found. Irwin has shown that for an elastic material, there is a relation between K_I and the energy release rate, G, as shown below [5]:

$$\begin{aligned} G =& \frac{K_I^2}{E'} \\ E' =& E \quad (for \quad plane-stress) \\ E' =& \frac{E}{1-\nu^2} \quad (for \quad plane-strain) \end{aligned} \tag{2.11}$$

Once G is found K_I can be calculated from J. For a homogeneous elastic material G is equal to Rice's path-independent J-integral [5]:

$$\int_{\Gamma}(Wdy - \sigma_{ij}n_j u_{i,x}ds) \tag{2.12}$$

where Γ represents the contour of the integral, W is the strain energy density, σ_{ij} are the components of the stress tensor, n_j is the unit normal of the contour line and u_i represents the displacement vector components. J-integral is path independent for a homogeneous elastic material. It is shown in Figure 2.3 that J-integral reaches a constant value after a few contours from the crack tip in a nonlinearly elastic material

as well. Therefore, for an elastic body, K_I can be determined from the J-integral calculated on any contour around the crack tip using the following relation:

$$J = G = \frac{K_I^2}{E'} \tag{2.13}$$

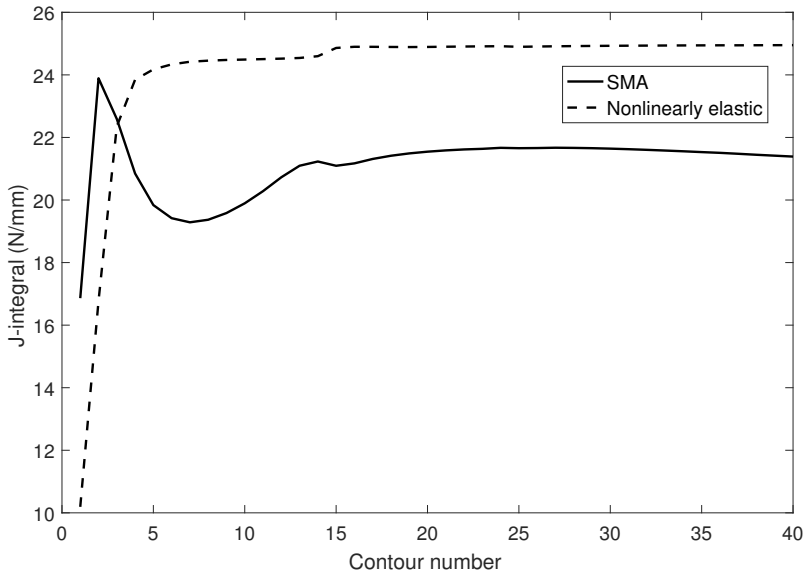

Figure 2.3. J-integral vs contour number for a nonlinearly elastic material and an SMA

In most studies, asymptotic equations of Williams have been used for crack tip fields of pseudoelastic SMAs. However, application of Equation 2.13 is problematic in the case an SMA. In Figure 2.3, it is seen that J-integral is not contour independent where the phase transformation takes place. Therefore, it is not clear which value of J should be used in the case of an SMA. In some studies, the use of far-field J-integral (J^{∞}) together with the elastic modulus of austenite is proposed to calculate K_I. Figure 2.4 shows the opening stress distribution ahead of the crack tip in an edge cracked SMA plate and corresponding stress distribution calculated using the equations of Williams. It is observed that the phase transformation in SMAs results in a redistribution of stresses in the vicinity of the crack tip and consequently actual stress distribution in the transformation zone is different than the predictions obtained using Williams' solution.

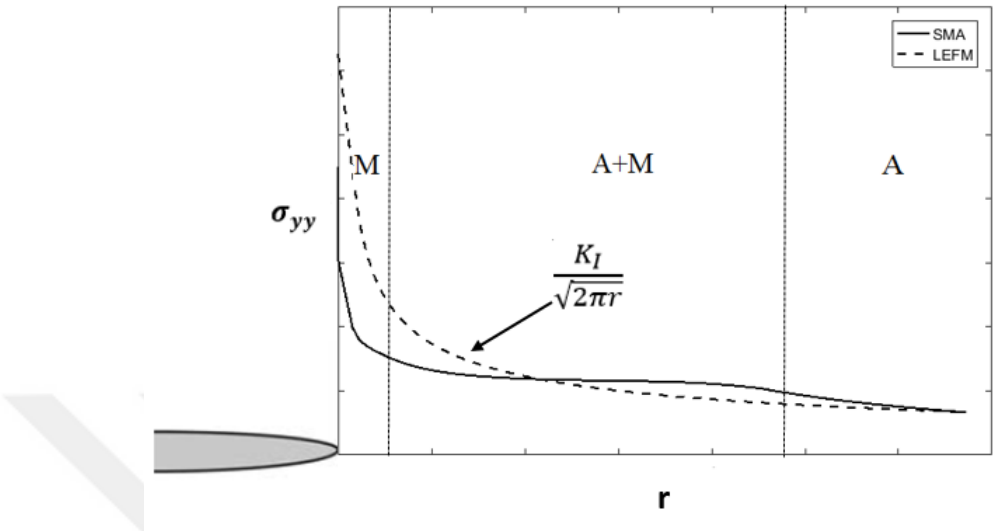

Figure 2.4. Opening stress distribution of an SMA ahead of crack tip, $\theta = 0$

Although the singular solution of Williams does not characterize crack tip fields of an SMA completely, it is still used to estimate the transformation region size, r_{tr}. On $\theta = 0$, along crack line, r_{tr} is estimated as follows [5]:

$$r_{tr} = \frac{1}{2\pi}\left(\frac{K_I}{\sigma_{tr}}\right)^2 \tag{2.14}$$

where σ_{tr} is the transformation stress.

There are also some studies on crack tip fields in SMAs that use the solution of Williams with modifications. For example, Maletta and Furgiuele [6] used Irwins's correction that is normally used for plastic zone effect near crack tip. Irwin accounted for the constant stress distribution in the plastic zone by defining an effective crack length which is larger than the physical length of the crack [5]. The stress intensity factor is calculated using the effective crack length, a_e which is shown in Figure 2.5. The stress distribution in the austenitic region is calculated then as follows:

$$\sigma_A = \frac{K_{Ie}}{\sqrt{2\pi(r - \triangle r)}} \tag{2.15}$$

where

$$K_{Ie} = \sigma^{\infty}\sqrt{\pi a_e} \tag{2.16}$$

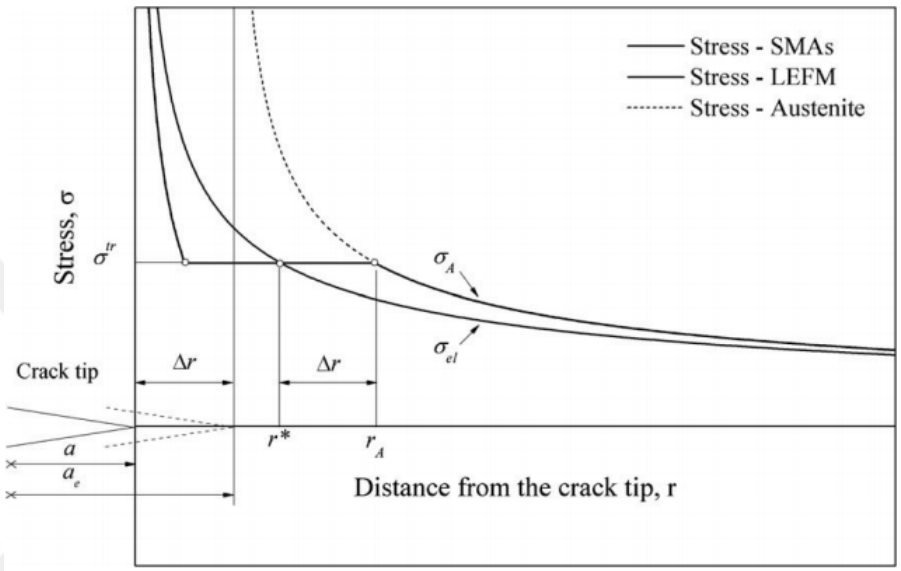

Figure 2.5. Irwin's correction to predict the stress distribution in the austenitic region [6]

There is also an approach developed by Hazar *et al.* [25] to determine the transformation zone using the asymptotic equations of Williams in a phenomenological SMA model. They inserted the asymptotic equations into the thermodynamic driving force for the martensitic transformation. Their results were in a good agreement with the results of experimental studies.

Although linear elastic fracture mechanics is a reasonable approach to start with, it is inadequate to evaluate fracture properties of SMAs. In order to characterize the crack tip fields in an SMA plate, it may be good idea to start with equations of elastic-plastic behavior. In case of an elastic-plastic material, the crack tip fields are more complex than these in linearly elastic materials since there is a more complicated relation between stress and strain. Figure 2.6 shows the stress-strain relation of

non-linearly elastic and elastic-plastic materials. As shown in the figure, there is no difference between the loading paths of both materials. Therefore, as long as unloading is not included, deformation of an elastic-plastic material can be analyzed with deformation theory of plasticity using nonlinear elasticity [5, 35].

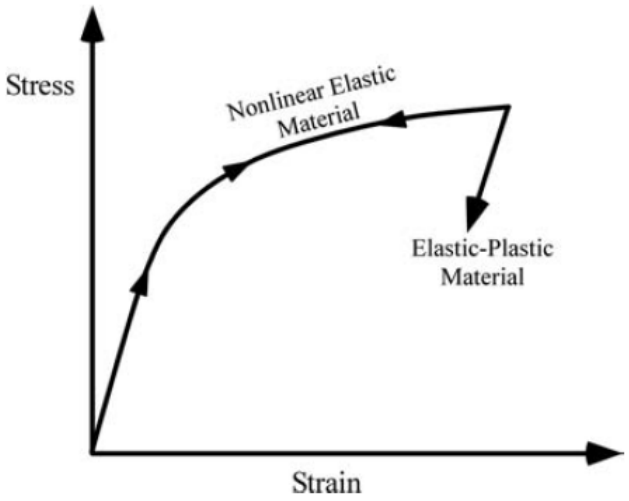

Figure 2.6. Stress-strain relations of non-linearly elastic and elastic-plastic materials [5]

2.3. HRR Formulation

Hutchinson, Rice and Rosengren have independently analyzed crack tip conditions using the constitutive relation of Ramberg and Osgood and formulated the behavior at the crack tip [7, 36]. The formulation is named as HRR in honor of them. In order to understand the HRR formulation, firstly Rmaberg-Osgood model should be investigated.

2.3.1. Ramberg-Osgood Model

Ramberg-Osgood [5] equation defines the stress-strain relation for hardening materials with no clear yield point as shown below:

$$\frac{\epsilon}{\epsilon_y} = \frac{\sigma}{\sigma_y} + \alpha(\frac{\sigma}{\sigma_y})^n \tag{2.17}$$

where σ_y is the yield strength, ϵ_y is the strain value at the yield point, α and n are the material constants which are obtained from the uni-axial tension test of the material. The first term on the right hand side represents the elastic part while the second term stands for the plastic one. In this study, the following non-dimensionalization is used [7]:

$$\bar{\sigma} = \frac{\sigma}{\sigma_y} \quad , \quad \bar{\epsilon} = \frac{\epsilon}{\epsilon_y} \quad and \quad \bar{l} = \frac{l}{a} \tag{2.18}$$

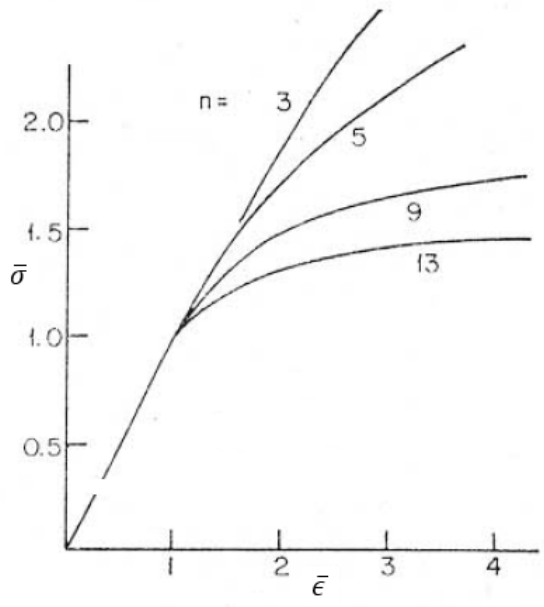

Figure 2.7. Ramberg-Osgood type stress-strain relation [7]

It is seen in Figure 2.7 that n increases as the level of hardening in the material decreases. Additionally, α determines the yield off-set.The three dimensional stress-strain relation based on the Ramberg-Osgood equation is as follows:

$$\bar{\epsilon}_{ij} = (1+\nu)\bar{S}_{ij} + \frac{1-2\nu}{3}\bar{\sigma}_{pp}\delta_{ij} + \frac{3}{2}\alpha\bar{\sigma}_{eqv}^{n-1}\bar{S}_{ij} \tag{2.19}$$

where S is the deviatoric stress tensor and σ_{eqv} is the von Mises equivalent stress. In plane stress, the non-zero strain components are calculated as [7]:

$$\begin{aligned} \bar{\epsilon}_r &= \bar{\sigma}_r - \nu\bar{\sigma}_\theta + \alpha\bar{\sigma}_{eqv}^{n-1}(\bar{\sigma}_r - \frac{1}{2}\bar{\sigma}_\theta) \\ \bar{\epsilon}_\theta &= \bar{\sigma}_\theta - \nu\bar{\sigma}_r + \alpha\bar{\sigma}_{eqv}^{n-1}(\bar{\sigma}_\theta - \frac{1}{2}\bar{\sigma}_r) \\ \bar{\epsilon}_{r\theta} &= (1+\nu)\bar{\sigma}_{r\theta} + \frac{3}{2}\alpha\bar{\sigma}_{eqv}^{n-1}\bar{\sigma}_{r\theta} \end{aligned} \tag{2.20}$$

2.3.2. Application of Ramberg-Osgood Model to Transformation in SMAs

In hardening materials, stress is proportional to strain until yielding. After yielding, there is a non-linear relation and nearly constant stress is observed with a substantial increase in strain. In that sense, the martensitic phase transformation of a pseudo-elastic SMA resembles to the plastic deformation in elastic-plastic materials; up to the end of transformation, a pseudoelastic SMA follows a similar loading path. Using this similarity, the transformation plateau in the stress-strain diagram of a pseudoelastic SMA is represented by the Ramberg-Osgood relation. The term yielding will indicate the start of phase transformation in the case of an SMA.

2.3.3. Stress Function Formulation of Hutchinson using Ramberg-Osgood

As in the case of eigenfunction solution of Williams, stresses are derived from a stress function using Equation 2.2 [7]. The strain field should be compatible with a kinematically admissible displacement field in order to satisfy the equilibrium under applied loading [35]; therefore, Ramberg-Osgood relation will be used in the compatibility

equation together with Equation 2.2. As a result, the following equation governing the stress function is obtained [7]:

$$\begin{aligned}\nabla^4\phi + \frac{\alpha}{2}\{r^{-1}\frac{\partial^2}{\partial r^2}[\sigma_e^{n-1}(2r\frac{\partial^2\phi}{\partial r^2} - \frac{\partial\phi}{\partial r} - r^{-1}\frac{\partial^2\phi}{\partial\theta^2})] + 6r^{-2}\frac{\partial^2}{\partial r\partial\theta}[\sigma_e^{n-1}r\frac{\partial}{\partial r}(r^{-1}\frac{\partial\phi}{\partial\theta})] \\ +r^{-1}\frac{\partial}{\partial r}[\sigma_e^{n-1}(-2r^{-1}\frac{\partial\phi}{\partial r} - 2r^{-2}\frac{\partial^2\phi}{\partial\theta^2} + \frac{\partial^2\phi}{\partial r^2})] \\ +r^{-2}\frac{\partial^2}{\partial\theta^2}[\sigma_e^{n-1}(-\frac{\partial^2\phi}{\partial r^2} + 2r^{-1}\frac{\partial\phi}{\partial r} + 2r^{-2}\frac{\partial^2\phi}{\partial\theta^2})]\} = 0\end{aligned} \tag{2.21}$$

In the case of a linearly elastic, isotropic and homogeneous medium, the equation that governs the stress function is only the first term of Equation 2.21 [5].

To obtain the stress field around the crack tip, the solution to the stress function is assumed to be in the following form [7],

$$\phi(r,\theta) = \kappa r^s\tilde{\phi}(\theta) \tag{2.22}$$

where κ is the amplitude of the stress function, s is a constant determining the singularity and $\tilde{\phi}(\theta)$ is the θ dependent part of the stress function which are all to be determined. Using Equation 2.2, asymptotic stresses are derived from the stress function as follows [7]:

$$\begin{aligned}\sigma_{rr} =&\kappa r^{s-2}(s\tilde{\phi} + \frac{d^2\tilde{\phi}}{d\theta^2}) = \kappa r^{s-2}\tilde{\sigma}_r(\theta) \\ \sigma_{\theta\theta} =&\kappa r^{s-2}s(s-1)\tilde{\phi} = \kappa r^{s-2}\tilde{\sigma}_\theta(\theta) \\ \sigma_{r\theta} =&\kappa r^{s-2}(1-s)\frac{d\tilde{\phi}}{d\theta} = \kappa r^{s-2}\tilde{\sigma}_{r\theta}(\theta) \\ \sigma_{eqv} =&\kappa r^{s-2}(\tilde{\sigma}_r^2 + \tilde{\sigma}_\theta^2 - \tilde{\sigma}_r\tilde{\sigma}_\theta + 3\tilde{\sigma}_{r\theta}^2)^{\frac{1}{2}} = \kappa r^{s-2}\tilde{\sigma}_{eqv}(\theta)\end{aligned} \tag{2.23}$$

For the sake of simplicity, bar icons will not be used in the remaining parts of this thesis without forgetting however that field functions are all non-dimensionalized as previously explained. In order to obtain $\tilde{\phi}(\theta)$, Equation 2.21 must be solved with the

traction free boundary conditions on the crack faces, $\sigma_{\theta\theta}(\pm\pi) = \sigma_{r\theta}(\pm\pi) = 0$, which are satisfied with,

$$\tilde{\phi}(\pm\pi) = \frac{\partial\tilde{\phi}}{\partial\theta}(\pm\pi) = 0 \tag{2.24}$$

The solution of the governing equation with given boundary conditions is obtained numerically; a fourth order Runge-Kutta method is applied to obtain the solution, the boundary value problem is converted into an initial value problem. Using the symmetry of the crack, the boundary conditions can be also represented as follows [7]:

$$\frac{\partial^3\tilde{\phi}}{\partial\theta^3}(0) = \frac{\partial\tilde{\phi}}{\partial\theta}(0) = 0 \tag{2.25}$$

As it is stated by Hutchinson [7], $\tilde{\phi}(0)$ is set to be one and the remaining initial value, $\frac{\partial^2\tilde{\phi}}{\partial\theta^2}(0)$, is found by using shooting method (different values are tried to find the correct initial value which satisfies the constraints in Equation 2.24). s is calculated from the following relation [7],

$$s = \frac{2n+1}{n+1} \tag{2.26}$$

which will be explained at a later point. The problem is solved in MATLAB for different n values. It is important that theta dependent parts of stresses are normalized with the maximum value of $\tilde{\sigma}_{eqv}$ because maximum of $\tilde{\sigma}_{eqv}$ should be one as stated by Hutchinson [7]. Distributions of the θ dependent parts of the asymptotic stresses are plotted below for $n = 5$ and $n = 15$.

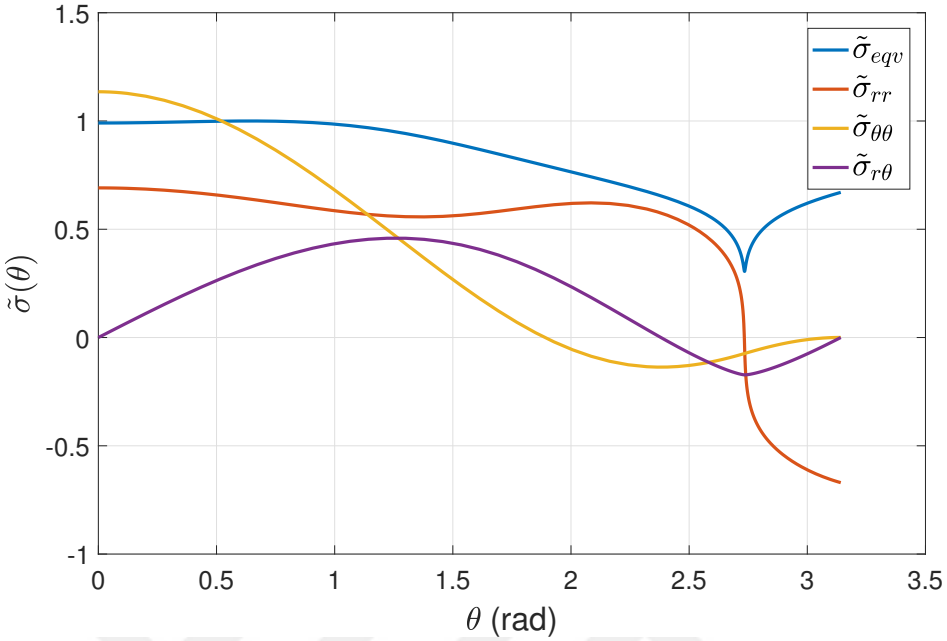

Figure 2.8. Distribution of the θ dependent parts of stresses for $n = 5$

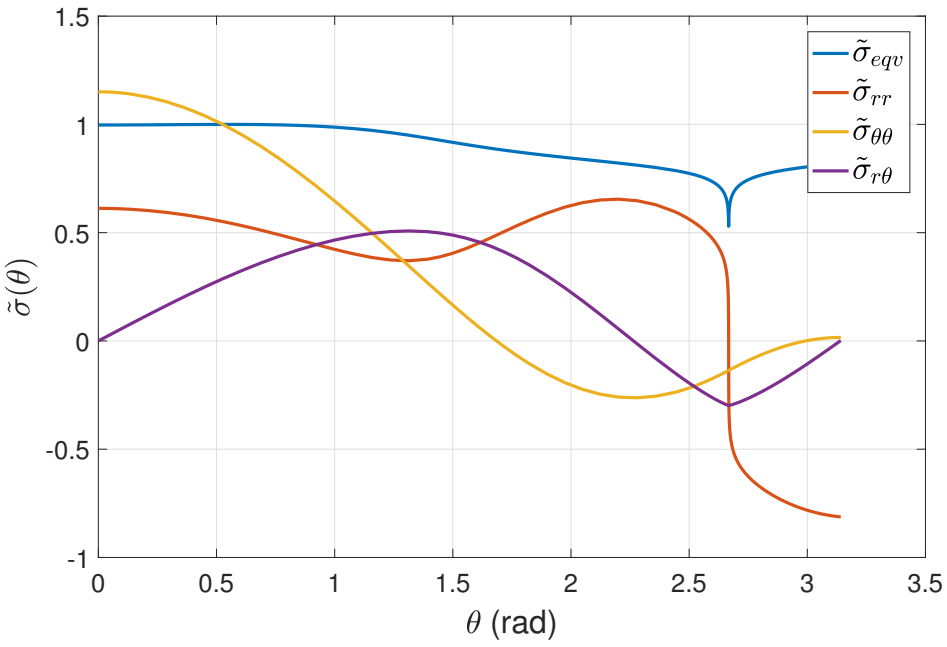

Figure 2.9. Distribution of the θ dependent parts of stresses for $n = 15$

From the figures above it is seen that the values of $\tilde{\sigma}_{rr}$, $\tilde{\sigma}_{tt}$, $\tilde{\sigma}_{rt}$ and $\tilde{\sigma}_{eqv}$ change with n. It should be also noted that the numerical method gives precise results up to around $n = 20$. With increasing n, the error in the numerical solution increases which

is also observed by Hutchinson [7].

Because the governing equations are totally different, $\tilde{\phi}(\theta)$ part of HRR solution is different than that of the stress function of Williams. Under the same loading, distribution of the asymptotic stresses around the crack tip vary with the material property in the case of HRR. While it is always the same for the linearly elastic case as shown in Figure 2.10. It is also interesting that, the stress singularity depends on n, in other words, on the mechanical behavior of the material while the square root singularity is constant in the formulation of Williams.

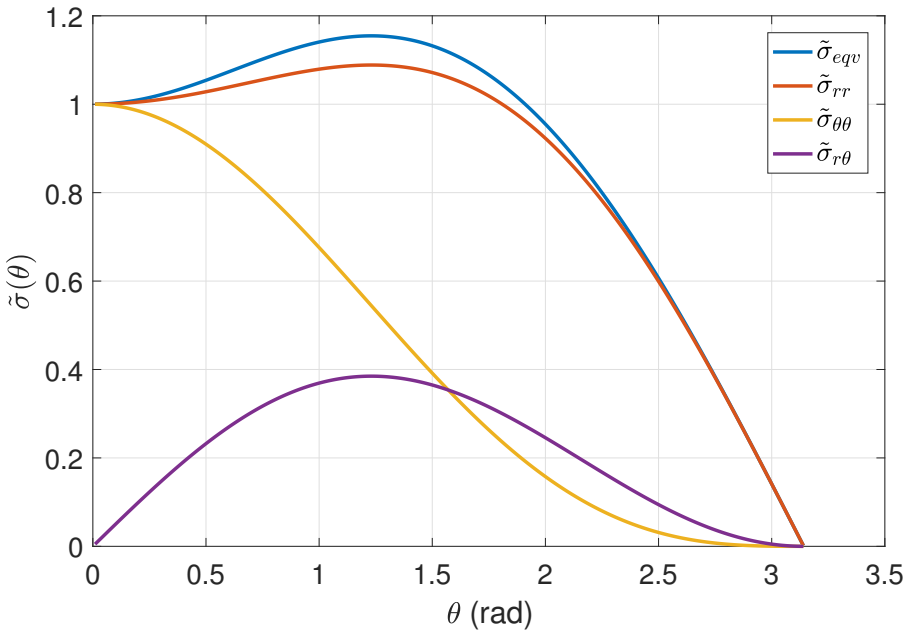

Figure 2.10. Distribution of the θ dependent parts of the stresses in LEFM

2.3.4. Amplitude of Stress Function

In order to identify the amplitude of the stress function, κ, Hutchinson has used Rice's J-integral [23]:

$$\int_{\Gamma}(W dy - \sigma_{ij} n_j u_{i,x} ds) \tag{2.27}$$

where Γ represents the contour of the integral as shown in Figure 2.11, W is the strain energy density written below:

$$W = \int_0^{\epsilon_{ij}} \sigma_{ij} d\epsilon_{ij} \tag{2.28}$$

u_i represents the displacement vector components.

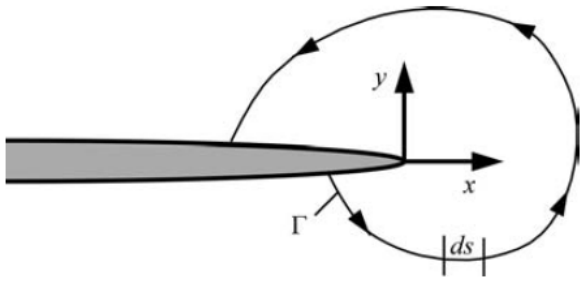

Figure 2.11. Contour of J around a crack [5]

Hutchinson has calculated the J-integral using the asymptotic stress equations in Equation 2.23 and finally obtained the non-dimensional J-integral as follows [7]:

$$J = \alpha \kappa^{n+1} r^{(n+1)(s-2)+1} I_n \tag{2.29}$$

where I_n is an integration constant which is calculated as follows:

$$\begin{aligned} I_n = \int_{-\pi}^{+\pi} \{ \frac{n}{n+1} \tilde{\sigma}_{eqv}^{n+1} cos\theta - [sin\theta \{ \tilde{\sigma}_{rr}(\tilde{u}_\theta - \tilde{u}_r^{\cdot}) - \tilde{\sigma}_{r\theta}(\tilde{u}_r + \tilde{u}_\theta^{\cdot}) \} \\ + cos\theta(n(s-2)+1)(\tilde{\sigma}_{rr}\tilde{u}_r + \tilde{\sigma}_{\theta\theta}\tilde{u}_\theta)] \} d\theta \end{aligned} \tag{2.30}$$

Rice previously showed that, for linearly or non-linearly elastic materials, J-integral is path-independent in a homogeneous body [23]. Using the path-independence of the J-integral, Hutchinson has equated Equation 2.29 to the J-integral calculated

in the elastic region and obtained the following relation [7]:

$$\alpha\kappa^{n+1}r^{(n+1)(s-2)+1}I_n = \pi(\sigma^{\infty})^2 \tag{2.31}$$

The right hand side of the equation comes from the well known relation between the J-integral and the stress intensity factor for the elastic materials, namely [5]:

$$J = \frac{K_I^2}{E} \tag{2.32}$$

In order to satisfy the path-independence of the J-integral, r should be removed from Equation 2.31 which is only satisfied by the relation in Equation 2.26. Finally, the amplitude of the stress function, κ, is obtained as [7]:

$$\kappa = (\frac{1}{\alpha})^{\frac{1}{1+n}}(\frac{\pi}{I_n})^{\frac{1}{n+1}}(\sigma^{\infty})^{\frac{2}{n+1}} \tag{2.33}$$

or in terms of the J-integral,

$$\kappa = \big(\frac{J}{\alpha I_n}\big)^{\frac{1}{1+n}} \tag{2.34}$$

As a result, stresses (normalized by yield stress) can be calculated using the equation below:

$$\sigma_{ij}(r,\theta) = \big(\frac{J}{\alpha I_n r}\big)^{\frac{1}{1+n}}\tilde{\sigma}_{ij}(\theta) \tag{2.35}$$

where the values of I_n are evaluated by Hutchinson [7] as shown in Figure 2.12.

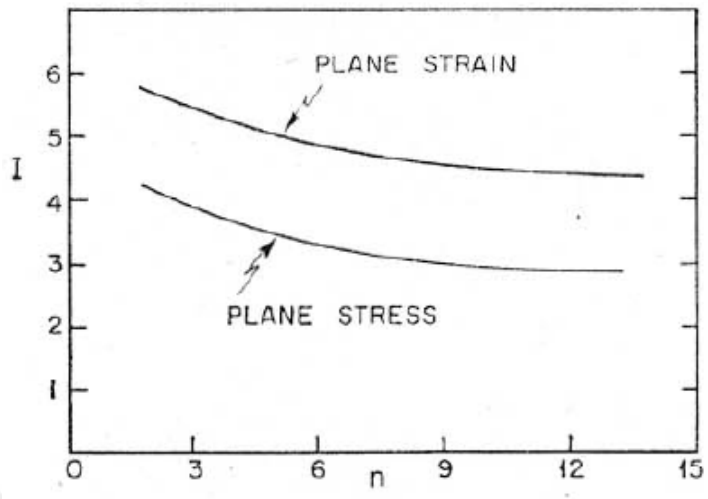

Figure 2.12. I_n vs n [7]

3. EVALUATION OF CRACK TIP FIELDS IN SMAs USING HRR

3.1. Problem Statement

In this chapter, crack tip fields in an edge cracked NiTi plate are evaluated using both Williams' [14] and HRR solutions. A compact tension specimen (CT), made of NiTi as the one in the experimental study of Haghgouyan *et al.* [8], is modeled (fracture tests at room temperature were performed on fatigue pre-cracked CT specimens). Geometry of the plate is as shown in Figure 3.1. Dimensions of the specimen are $W = 26$ mm, $h = 15.6$ mm and the thickness (B) is 1 mm. In fracture tests, the displacements u_x and u_y were found using digital image correlation (DIC) and using numerical differentiation with central difference formulas strains which were used to evaluate the transformation region around the crack tip were calculated.

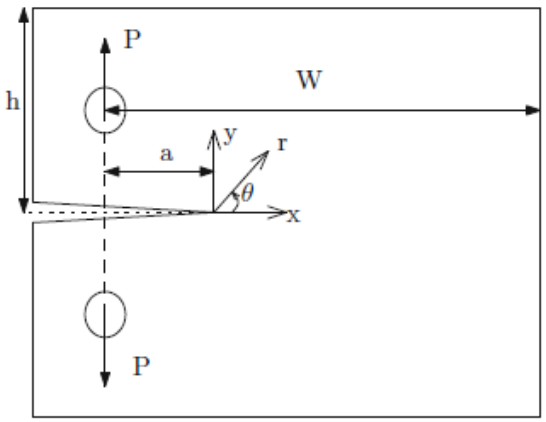

Figure 3.1. Geometry of edge cracked specimen

A comprehensive discussion on approaches of Williams and Hutchinson will be presented and their results will be compared to the experimental ones. A closed form formulation of the transformation region will be given in Chapter 4.

3.2. Evaluation of Mechanical Constants, α and n, of Ramberg-Osgood Equation

In order to evaluate the crack tip fields using HRR method, one has to determine the material constants of the Ramberg-Osgood equation, namely α and n which are obtained using the stress-strain diagram of the material. In this section, mechanical properties of the NiTi experimentally obtained by Haghgouyan *et al.* [8] are used. 1 mm thick NiTi dog-bone samples (Ni: 55.99 wt.%) with $A_f^0 = 16.1°C$ were tested by Haghgouyan *et al.* [8] at room temperature. Stress-strain diagram was obtained as shown in Figure 3.2. Elastic modulus of austenite and martensite were reported as $E_A = 47.8$ GPa and $E_M = 32$ GPa. Transformation start and finish strains were determined to be around 1% and 5.8% and marked as A and B on the stress-strain diagram.

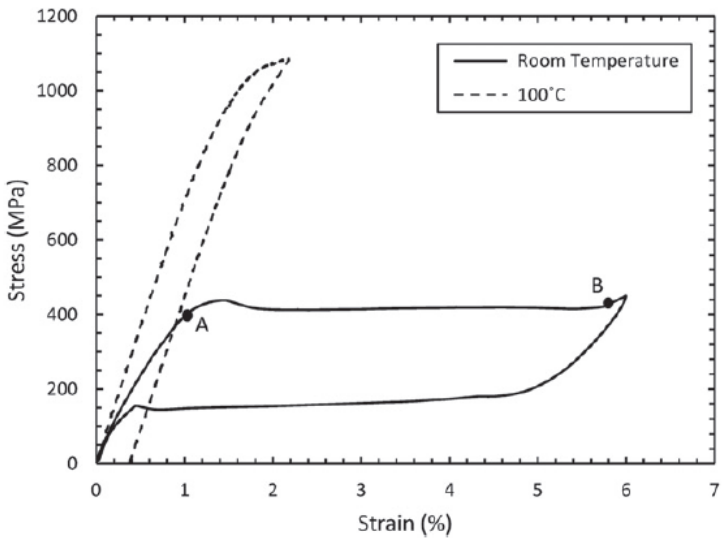

Figure 3.2. Stress-strain relation of NiTi [8]

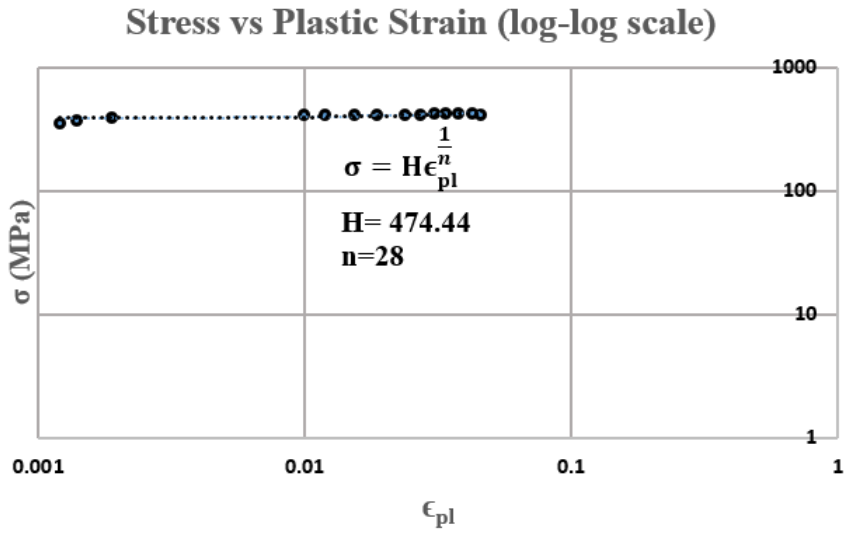

Figure 3.3. Stress vs plastic strain in log-log scale

Mechanical constants in the Ramberg-Osgood equation for this specific material are determined following the procedure described by Dowling [9]. Because the main focus is on the inelastic part of the strain, the elastic deformation is neglected, resulting in a power-hardening relation:

$$\sigma = H{\epsilon_{pl}}^{\frac{1}{n}} \tag{3.1}$$

where H is the value of σ at $\epsilon_{pl} = 1$ and $\frac{1}{n}$ is the slope in the log-log plot of the stress vs plastic strain as shown in Figure 3.3. In Ramberg-Osgood stress-strain relation, the yield strength may be defined according to the offset strain as shown in Figure 3.4. The most widely used offset strain for common engineering materials is 0.002 [9]. As a result

$$\sigma_y = H{0.002}^{\frac{1}{n}} \tag{3.2}$$

is used and the yield strength is found to be $\sigma_y = 380$ MPa .

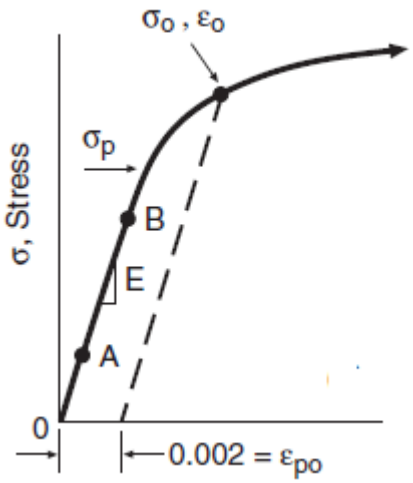

Figure 3.4. Stress-strain relation showing the yield offset [9]

At the yield point:

$$\epsilon = \frac{\sigma}{E} + \alpha\epsilon_y \tag{3.3}$$

Therefore $\alpha\epsilon_y$ determines the yield offset and α is calculated from the following equation:

$$\alpha = \frac{0.002}{\epsilon_y} \tag{3.4}$$

As a result, $n = 28$ and $\alpha = 0.2$ are calculated fitting a curve to the Ramberg-Osgood equation as shown in Figure 3.5.

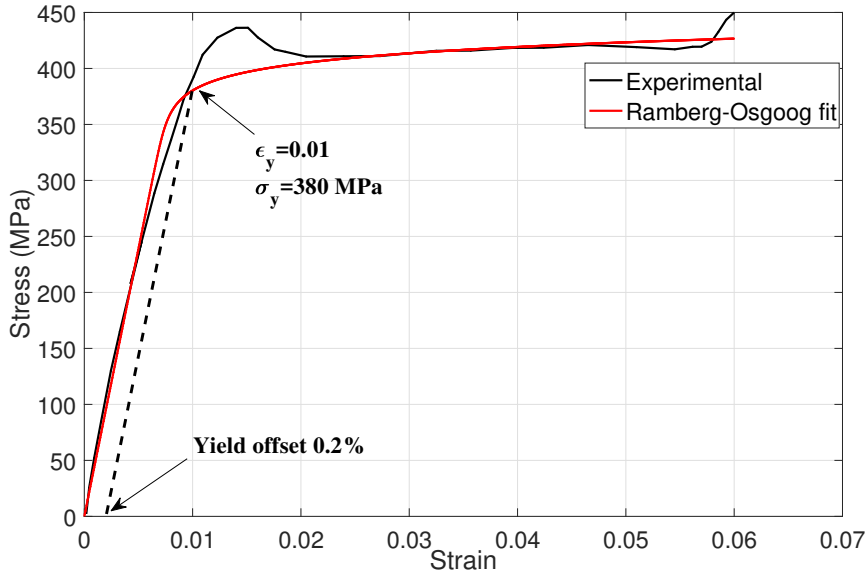

Figure 3.5. Ramberg-Osgood equation fit to loading path

As shown in Figure 3.5, the loading path of the NiTi plate could be successfully represented with the Ramberg-Osgood equation until the end of the transformation, when $n = 28$, $I_n = 2.68$ is used [7]. Distribution of the θ dependent parts of the stresses are obtained as explained in section 2.3.3 and plotted in Figure 3.6. As a result, all material parameters to be used in the asymptotic equations of Hutchinson are obtained. To calculate the crack tip fields, one has also to determine the amplitude of the stress function κ which depends on α and n.

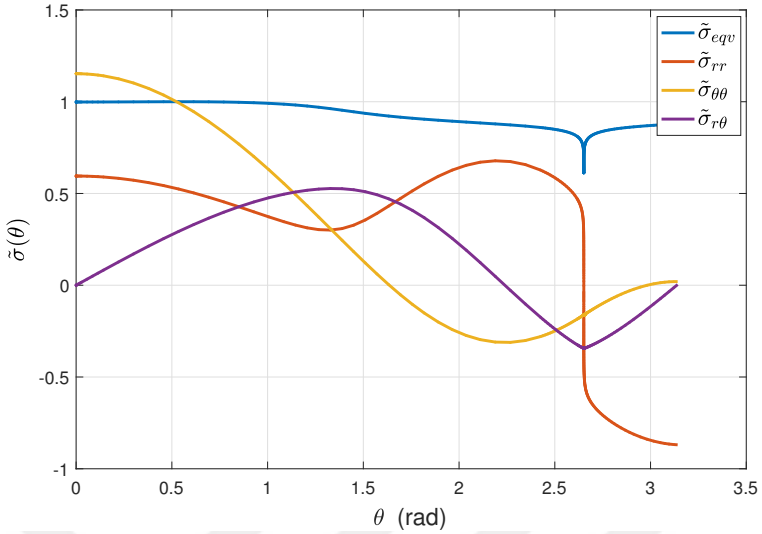

Figure 3.6. Distribution of θ dependent part of stresses for $n = 28$

3.3. Fracture Parameters

To use both asymptotic equations, K_I and κ should be determined. Haghgouyan *et al.* [8] calculated the stress intensity factor, K_I, using two different approaches. First, the asymptotic near-tip opening displacement equation is fit to the y-component of the displacement field (u_y) obtained from DIC using a least-square fit as done by Oral *et al.* [37]:

$$u_y = \underbrace{\frac{K_I}{2\mu}\left(\frac{r}{2\pi}\right)^{\frac{1}{2}} sin\frac{\theta}{2}\left(\frac{3-\nu_{tip}}{1+\nu} - cos\theta\right) - \frac{T\nu_{tip}}{2\mu(1+\nu_{tip})} rsin\theta}_{\text{Mode I loading}}$$
$$+ \underbrace{\frac{K_{II}}{4\mu}\left(\frac{r}{2\pi}\right)^{\frac{1}{2}}\left(\frac{5\nu-3}{1+\nu}cos\frac{\theta}{2} - cos\frac{3\theta}{2}\right)}_{\text{Mode II loading}} + \underbrace{A_1 rcos\theta + u_{0y}}_{R.B.} \tag{3.5}$$

In the equation above, T is the stress component parallel to the crack plane, A_1 and u_{0y} are the rigid body rotation and translation, ν is the Poisson's ratio and μ is the shear modulus. From DIC, the data which essentially encompass elastically deformed region, were used. Therefore, austenite shear modulus and $\nu = 0.33$ were inserted into the equation. As a result, K_I was calculated as $K_I = 35.5$ MPa$\sqrt{m}$ [8].

Another approach to obtain K_I is to use the equation given by ASTM E399 standard [28]:

$$K_I = \frac{P}{B\sqrt{W}} f(\frac{a}{W}) \tag{3.6}$$

where

$$f\left(\frac{a}{W}\right) = \frac{\left(2+\frac{a}{W}\right)\left[0.886+4.64\left(\frac{a}{W}\right)-13.32\left(\frac{a}{W}\right)^2+14.72\left(\frac{a}{W}\right)^3-5.6\left(\frac{a}{W}\right)^4\right]}{\left(1-\frac{a}{W}\right)^{\frac{3}{2}}} \tag{3.7}$$

and P is the applied load, B is the thickness and W is the width. Using Equation 3.6, K_I was calculated to be 31.9 MPa$\sqrt{m}$ for $P = 387$ N, $\frac{a}{W} = 0.6$, $B = 1$ mm and $W = 26$ mm [8].

In order to calculate κ for the equations of Hutchinson, Equations 2.32 and 2.34 are used with $K_I = 31.9$ MPa$\sqrt{m}$ and κ is found to be 0.985.

3.4. Crack Tip Fields

Stress distribution around the crack tip is calculated using the asymptotic equations of Williams and HRR. Fracture parameters, K_I and κ, specified in the previous section are used in the calculations. In Figures 3.7-3.10, stresses which are evaluated using HRR are plotted. In the following figures, HRR results are compared to the results obtained using Williams's equations. Crack tip is located at the origin and crack faces lie on the negative x-axis. Because the transformation region size is evaluated to be around 1 mm by Haghgouyan *et al.* [8], contours up to $1-2$ mm are investigated.

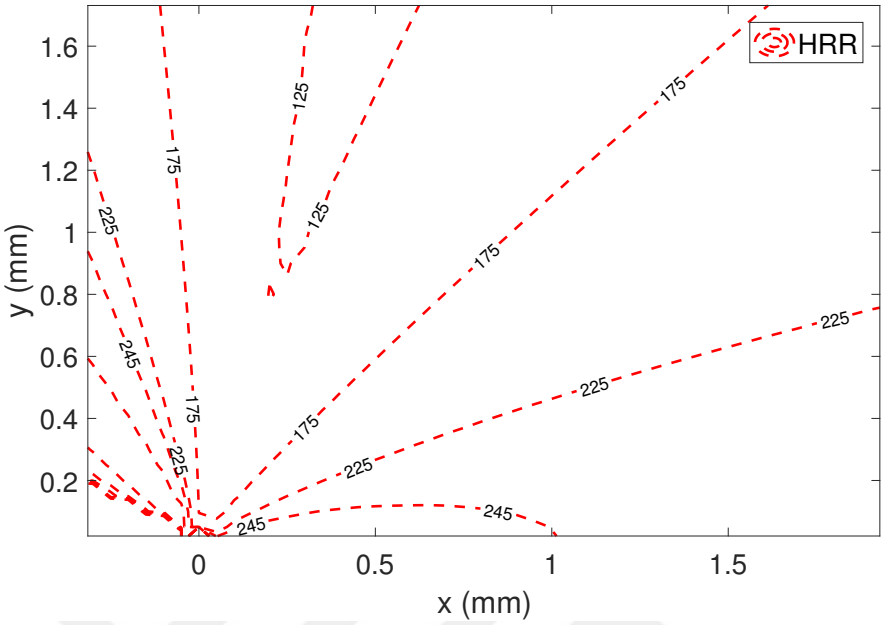

Figure 3.7. σ_{rr} (MPa) distribution around crack tip using HRR, x is measured from crack tip

It is observed that there is a significant difference in the shapes and values of the stress contours especially very near the crack tip. Stresses calculated using asymptotic equations of Williams increase abruptly through the crack tip which are 2-3 times the values calculated using HRR. In SMAs, martensitic transformation limits the increase in the stress which cannot be represented with linear elastic stress-strain relation. It is clearly shown especially in Figures 3.17 and 3.18 that equivalent stresses calculated using HRR increase slowly as expected. Additionally, the opening stresses ahead of the crack tip calculated using asymptotic equations are plotted in Figure 3.19. It is again observed that HRR stresses increase very slowly around the crack tip which is not the case for values calculated using asymptotic equation of Williams.

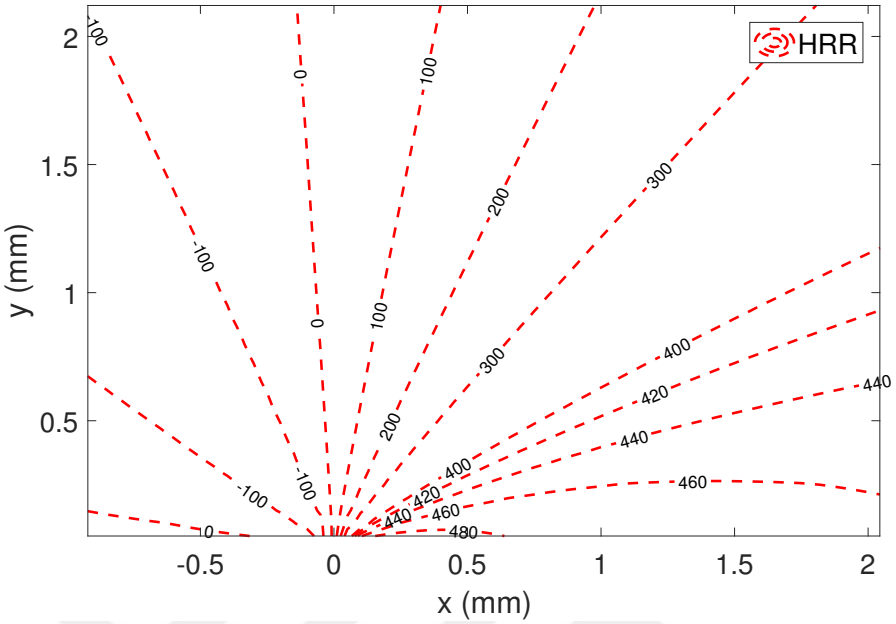

Figure 3.8. $\sigma_{\theta\theta}$ (MPa) distribution around crack tip using HRR, x is measured from crack tip

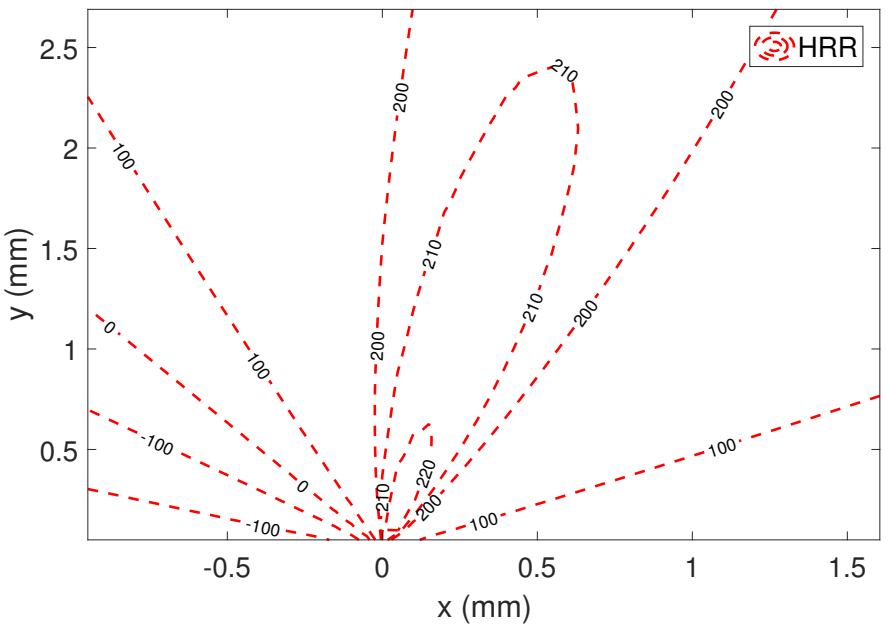

Figure 3.9. $\sigma_{r\theta}$ (MPa) distribution around crack tip using HRR, x is measured from crack tip

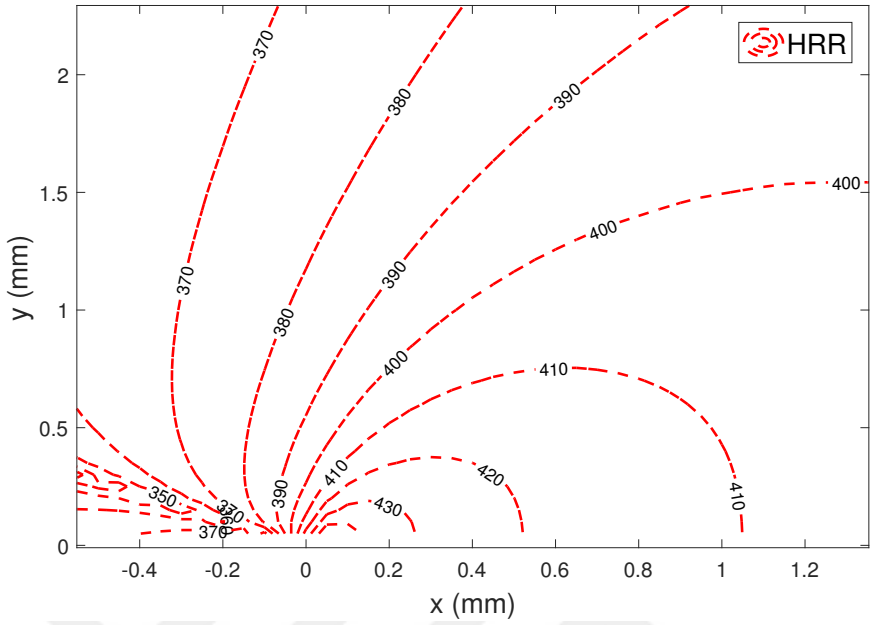

Figure 3.10. σ_{eqv} (MPa) distribution around crack tip using HRR, x is measured from crack tip

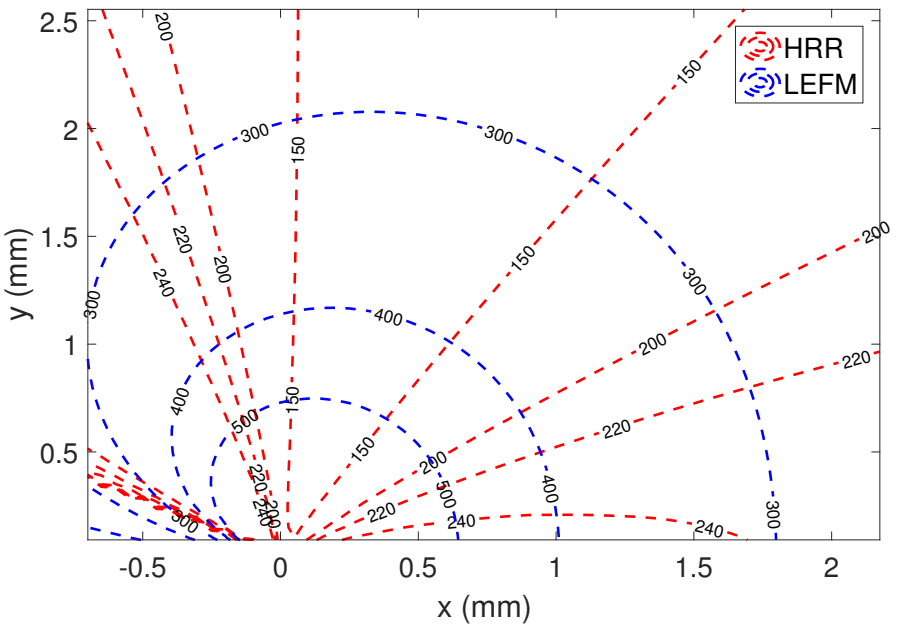

Figure 3.11. Comparison of σ_{rr} (MPa) distribution (HRR vs Williams), x is measured from crack tip

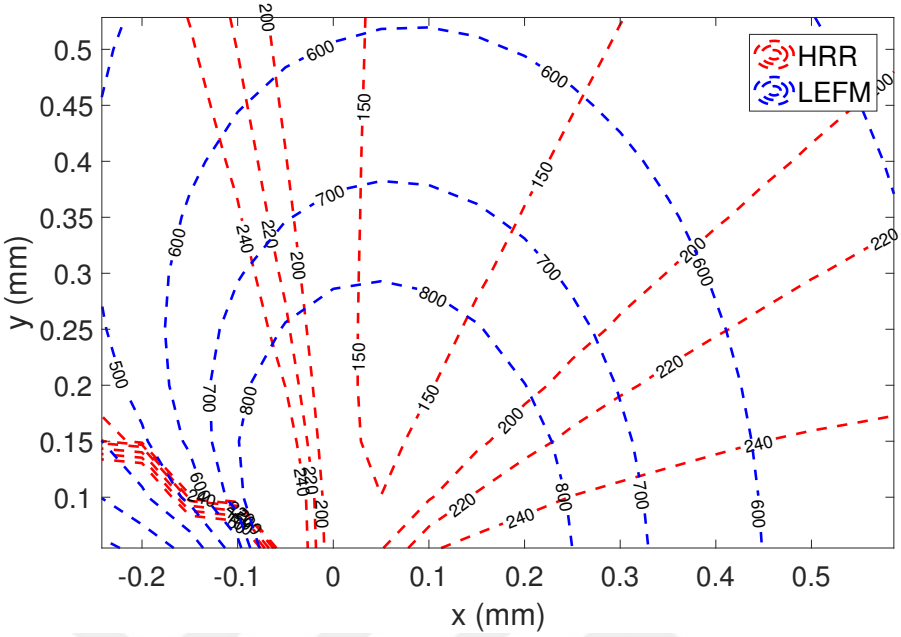

Figure 3.12. Comparison of σ_{rr} (MPa) distribution near the crack tip (HRR vs Williams), x is measured from crack tip

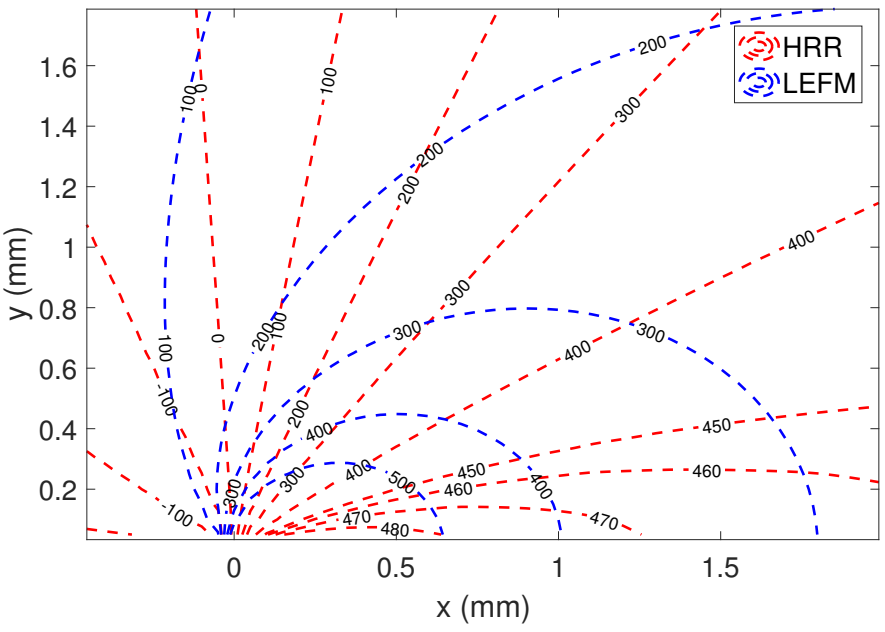

Figure 3.13. Comparison of $\sigma_{\theta\theta}$ (MPa) distribution (HRR vs Williams), x is measured from crack tip

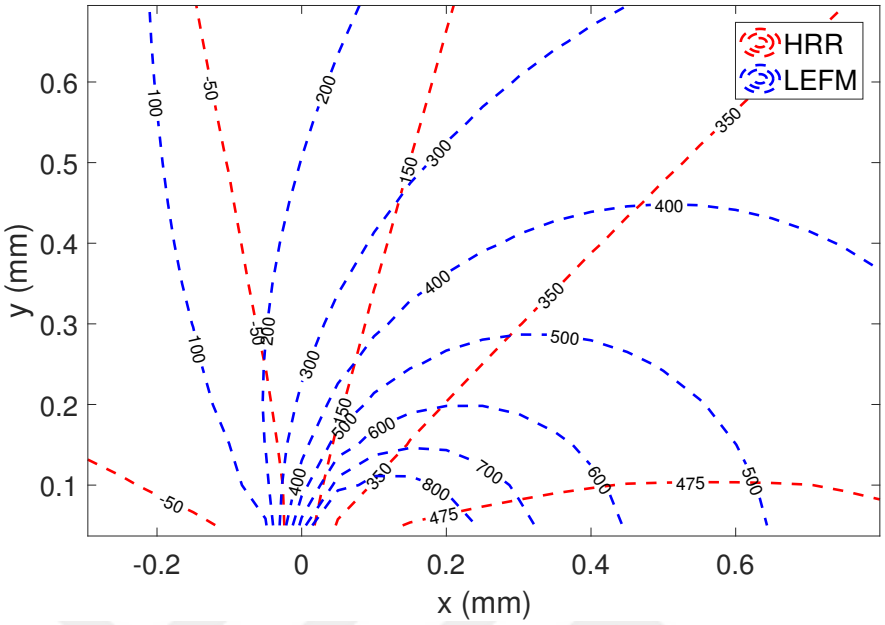

Figure 3.14. Comparison of $\sigma_{\theta\theta}$ (MPa) distribution near the crack tip (HRR vs Williams), x is measured from crack tip

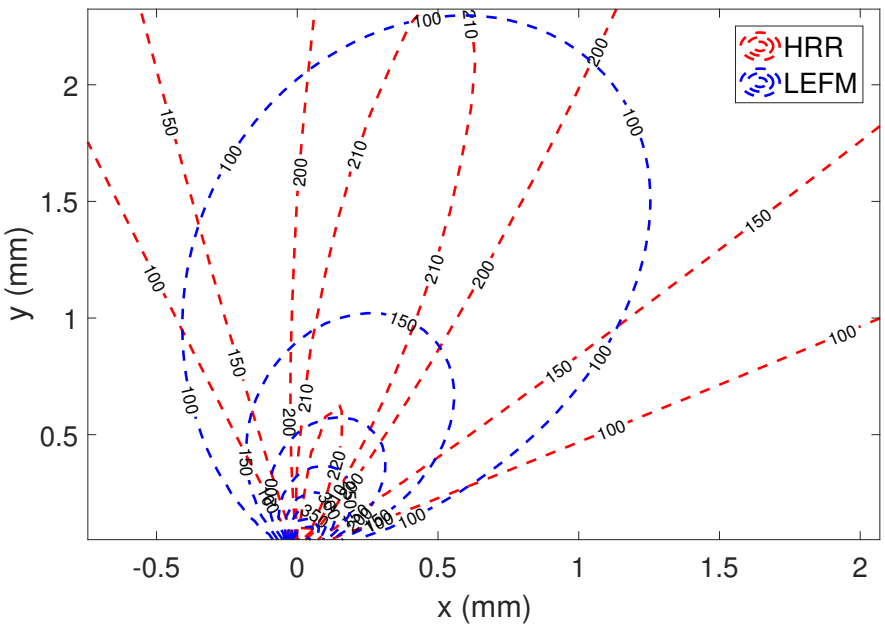

Figure 3.15. Comparison of $\sigma_{r\theta}$ (MPa) distribution (HRR vs Williams), x is measured from crack tip

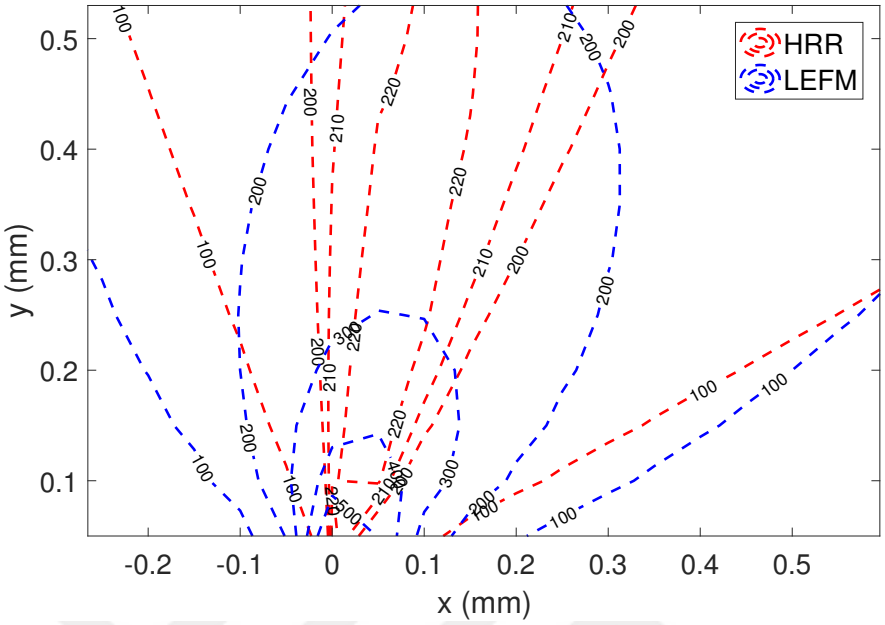

Figure 3.16. Comparison of $\sigma_{r\theta}$ (MPa) distribution near the crack tip (HRR vs Williams), x is measured from crack tip

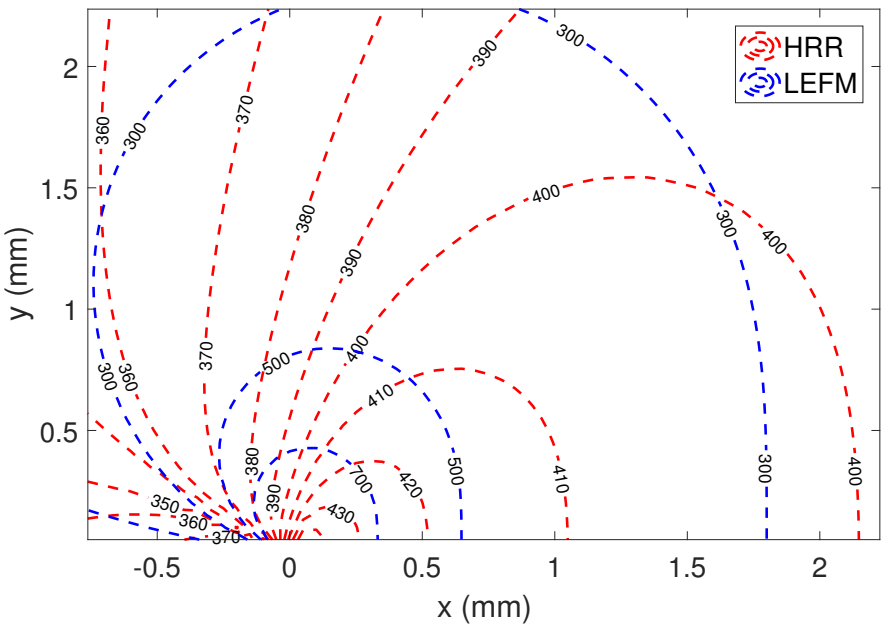

Figure 3.17. Comparison of σ_{eqv} (MPa) distribution (HRR vs Williams), x is measured from crack tip

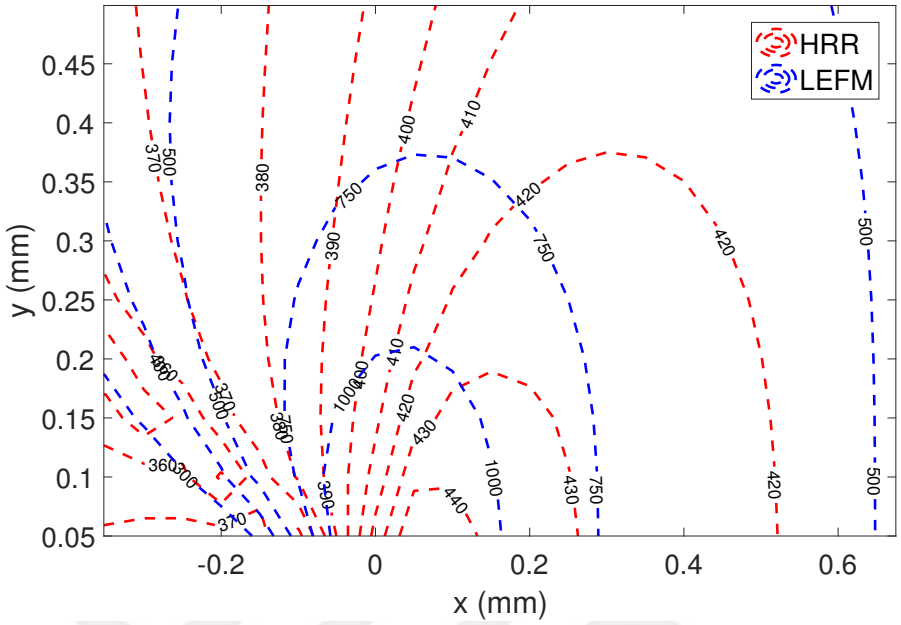

Figure 3.18. Comparison of σ_{eqv} (MPa) distribution near the crack tip (HRR vs Williams), x is measured from crack tip

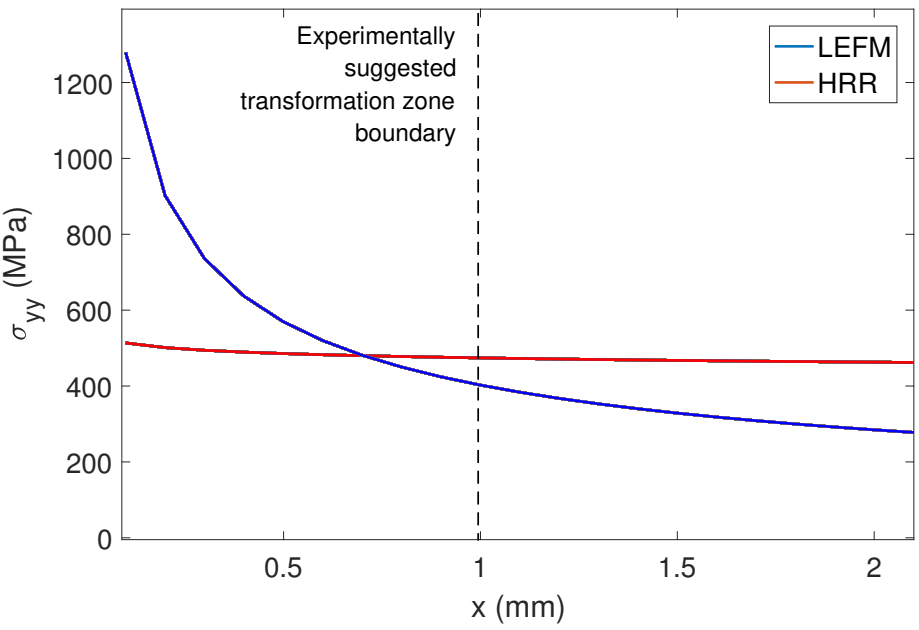

Figure 3.19. Comparison of opening stress distribution ahead of the crack tip

Figure 3.19 clearly shows that the increase in stress calculated using the asymptotic equation of Williams is not feasible due to the effect of phase transformation in SMAs. On the other hand, almost constant stress is calculated using the HRR method. HRR method seems to be more suitable to evaluate the crack tip fields of SMAs. It should be noted that HRR method cannot represent higher stresses very near the crack tip as a result of the elastic deformation of martensite; however, the martensitic region is very small as it is reported by many researchers [8, 32]. Although HRR does not represent the SMA behavior completely, it will be shown in the following chapters that HRR method will be very successful in evaluation of the transformation, even for the fully martensite region sizes.

3.5. Applicability of HRR Formulation

Application of the Ramberg-Osgood formula to fracture problems is restricted to some conditions since it is based on the deformation theory of plasticity. Deformation theory of plasticity assumes that plastic strains are functions of the current state of stress. On the other hand, in the incremental plasticity theory it is believed that plastic strains depend on the history of loading. For plasticity, incremental theory is more realistic, however, at the same time it's application is very complex. For uniaxial loading, both theories coincide unless there is no unloading. Although it is not simple for multiaxial loading, deformation theory of plasticity is quite a reasonable approximation in some special cases [35]. For multiaxial loading, deformation theory of plasticity and the incremental theory coincide when the deviatoric stress components are proportional to the effective stress such that,

$$S_{ij} = w_{ij}\sigma_e \tag{3.8}$$

where w is a constant tensor. Proportional loading physically means that all stress components increase in proportion to each other [38]. When plane-stress or plane-strain problems are considered, it is shown that the requirement of proportional deviatoric stress is approximately satisfied [5].

On the other hand, validity of deformation theory of plasticity does not guarantee the single parameter representation of the crack tip fields, like K_I or J. Single parameter assumption enables the evaluation of the structural behavior from small-scale laboratory tests, in other words, it means that fracture toughness in independent of specimen size. For single-parameter fracture mechanics, total stress components should be proportional near the crack tip [5]. In both solutions of Williams and Hutchinson, stresses near the crack tip are derived from a stress function such as in Equation 2.22. Equation 2.22 implies that at a certain point near the crack tip, all stress components are proportional to a constant and proportional to one another which guarantees a single parameter representation of the crack tip fields [5]. In Figure 3.20, it is seen that at a certain angle around the crack tip, there is a constant ratio between σ_{rr} and $\sigma_{\theta\theta}$ according to the stress function of Hutchinson (only where $\frac{\pi}{2} > \theta > 0$ is shown due to overlapping of data in other regions).

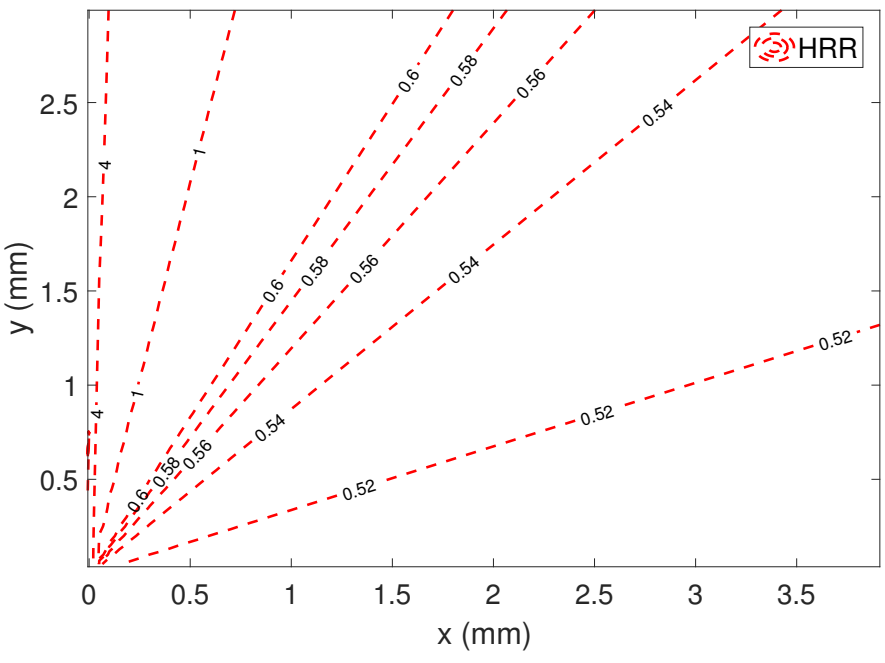

Figure 3.20. $\frac{\sigma_{rr}}{\sigma_{\theta\theta}}$ distribution near crack tip according to HRR

There is another important restriction on the application of the J-integral: in order to use the path-independent behavior of the J-integral, small scale yielding condition around the crack tip should be satisfied in an elastic-plastic material [5,7,23,39].

In other words, plastically deformed region where finite strains occur should be very small compared to geometric dimensions such as notch geometry and unnotched specimen width [23]. In the literature, strain values up to 0.1 (10%) are accepted in the limits of small scale yielding [5]. For the edge cracked problem in this study, 0.1 strain values are observed only in the full martensite region which is very small in size.

In derivation of HRR equations, it is assumed that the elastic strains are very small compared to plastic strains near the crack tip: $\frac{\epsilon_{pl}}{\epsilon_{el}}$ ratio is calculated for components of the strain tensor and plotted in Figures 3.21, 3.22, 3.23. It is observed that the ratio is much greater than 1 in the domain of interest except for ϵ_{rr}. Even for ϵ_{rr}, there is a substantial amount of region in which the ratio is greater than 1. Therefore it is concluded that, the assumption of small elastic strains is valid for this problem. Consequently, it is observed that characterization of the crack tip fields in SMAs by HRR singularity is a reasonable approach if the martensitic region is kept small compared to the transformation region.

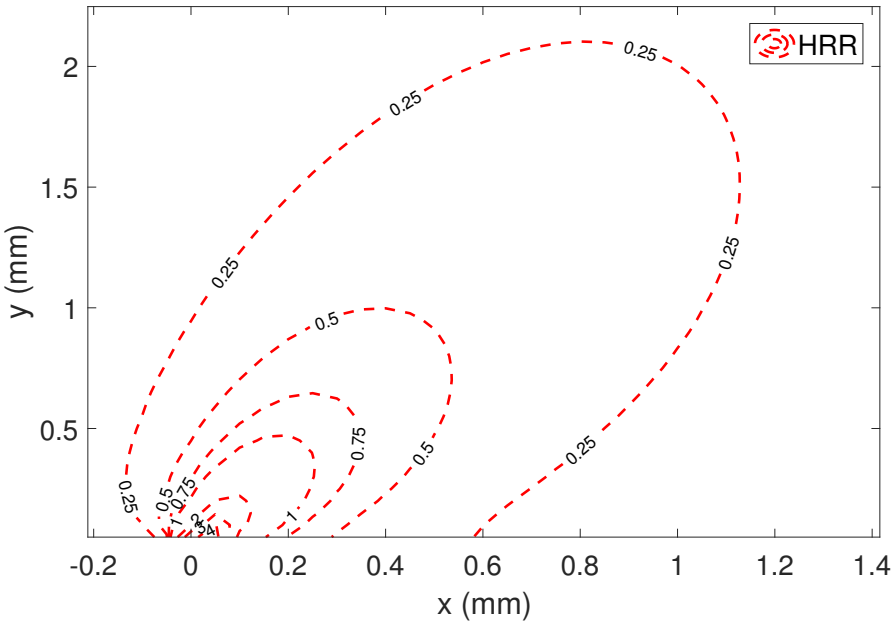

Figure 3.21. $\frac{\epsilon_{rr}^{pl}}{\epsilon_{rr}^{el}}$ near crack tip, x is measured from crack tip

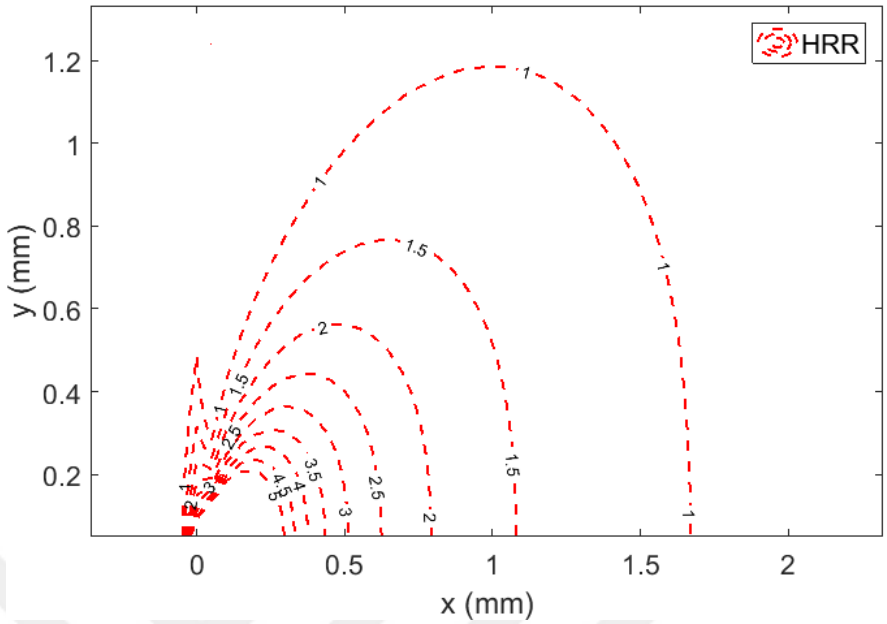

Figure 3.22. $\frac{\epsilon_{\theta\theta}^{pl}}{\epsilon_{\theta\theta}^{el}}$ near crack tip, x is measured from crack tip

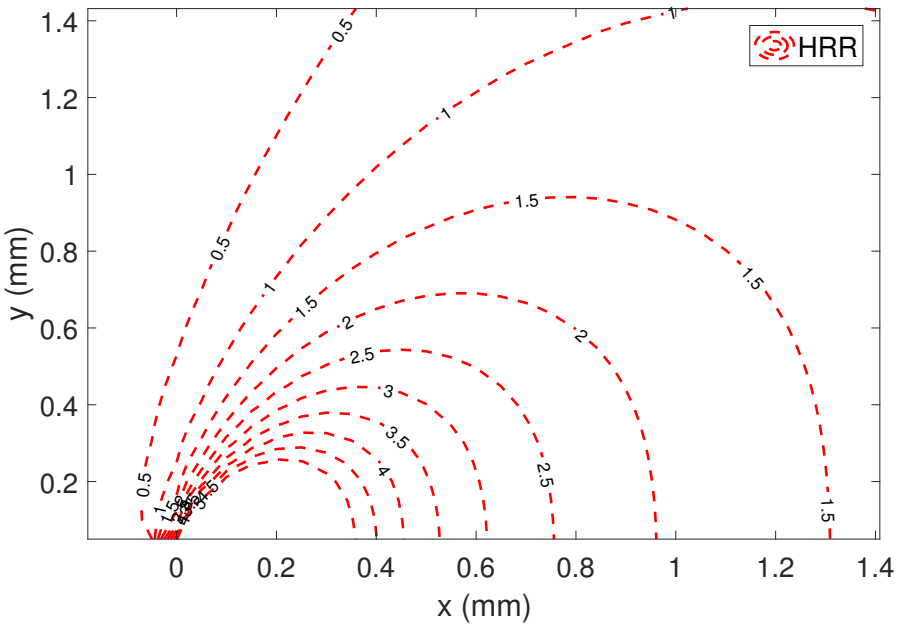

Figure 3.23. $\frac{\epsilon_{r\theta}^{pl}}{\epsilon_{r\theta}^{el}}$ near crack tip, x is measured from crack tip

4. EVALUATION OF THE TRANSFORMATION REGION AROUND CRACK TIP

Martensitic transformation has a significant effect on crack tip fields, and the evaluation of the transformation region is important in studying the fracture behavior of SMAs. In this chapter, an analytical estimation of the transformation region will be performed following the method used by Hazar *et al.* [25]. Asymptotic equations of Williams and HRR will be used together in a phenomenological model developed by Z. Moumni and W. Zaki [26]. Transformation region obtained in section 3.4 will be reevaluated using this method and the results will be compared to the experimental ones.

4.1. The Transformation Function Governing the Forward Phase Transformation

The phenomenological model for SMAs developed by W. Zaki and Z. Mounmi [26] considers two phases, namely austenite (elastic) and single variant martensite (inelastic). The free energy density of the material can be written as follows:

$$\psi(T, \boldsymbol{\epsilon_A}, \boldsymbol{\epsilon_M}, z, \boldsymbol{\epsilon_{tr}}) = (1-z)\big(\frac{1}{2}\boldsymbol{\epsilon_A} : \boldsymbol{K_A} : \boldsymbol{\epsilon_A}\big) + z\big[\frac{1}{2}(\boldsymbol{\epsilon_M} - \boldsymbol{\epsilon_{tr}}\big) : \boldsymbol{K_M} : (\boldsymbol{\epsilon_M} - \boldsymbol{\epsilon_{tr}}\big) + C(T)\big] + G\frac{z^2}{2} + \frac{z}{2}[\alpha z + \beta(1-z)]\big(\frac{2}{3}\boldsymbol{\epsilon_{tr}} : \boldsymbol{\epsilon_{tr}}\big) \tag{4.1}$$

where $\boldsymbol{\epsilon_A}$ and $\boldsymbol{\epsilon_M}$ are the local deformation tensors of austenite and martensite, $\boldsymbol{\epsilon_{tr}}$ is the orientation strain tensor of martensite, z is the volume fraction of martensite, $C(T)$ is the latent heat density as a result of phase transformation, $\boldsymbol{K_A}$ and $\boldsymbol{K_M}$ are elastic moduli tensors of austenite and martensite. α, β and G are determined from the orientation and superelastic experiments of the material [26].

The constraints of the model are:

$$\begin{aligned} (1-z)\boldsymbol{\epsilon_A} + z\boldsymbol{\epsilon_M} - \boldsymbol{\epsilon} = 0 \\ z \geq 0 \quad and \quad (1-z) \geq 0 \\ \epsilon_0 - \sqrt{\frac{2}{3}\boldsymbol{\epsilon_{tr}} : \boldsymbol{\epsilon_{tr}}} \geq 0 \end{aligned} \tag{4.2}$$

where ϵ_0 is a material limit for the equivalent inelastic strain. State equations are obtained using the Lagrange multipliers method. Using the Lagrange multipliers method with the constraints above, following Lagrangian is established:

$$\begin{aligned} L = (1-z)\big(\frac{1}{2}\boldsymbol{\epsilon_A} : \boldsymbol{K_A} : \boldsymbol{\epsilon_A}\big) + z\big[\frac{1}{2}(\boldsymbol{\epsilon_M} - \boldsymbol{\epsilon_{tr}}\big) : \boldsymbol{K_M} : (\boldsymbol{\epsilon_M} - \boldsymbol{\epsilon_{tr}}\big) \\ +C(T)\big] + G\frac{z^2}{2} + \frac{z}{2}[\alpha z + \beta(1-z)]\big(\frac{2}{3}\boldsymbol{\epsilon_{tr}} : \boldsymbol{\epsilon_{tr}}\big) - \boldsymbol{\lambda} : \big[(1-z)\boldsymbol{\epsilon_A} + z\boldsymbol{\epsilon_M} - \boldsymbol{\epsilon}\big] \\ -\mu\big(\epsilon_0 - \sqrt{\frac{2}{3}\boldsymbol{\epsilon_{tr}} : \boldsymbol{\epsilon_{tr}}}\big) - \nu_1 z - \nu_2(1-z) \end{aligned} \tag{4.3}$$

where $\boldsymbol{\lambda}$, μ, ν_1 and ν_2 are Lagrange multipliers. Taking the derivative of the Lagrangian with respect to strain, stress-strain relation is obtained as follows:

$$\boldsymbol{\sigma} = \boldsymbol{K} : (\boldsymbol{\epsilon} - z\boldsymbol{\epsilon_{tr}}) \tag{4.4}$$

where

$$\boldsymbol{K} = \big[(1-z)\boldsymbol{K_A}^{-1} + z\boldsymbol{K_M}^{-1}\big]^{-1} \tag{4.5}$$

Evolution of martensitic region is evaluated by using a transformation function derived using the state equations and a pseudo-potential of dissipation. In an isotropic, pseudoelastic SMA, the transformation function, in other words the thermodynamic force driving the forward phase transformation is given by Zaki and Moumni [26] as shown

below:

$$F_z = \{E^{'}\frac{\sigma_{eqv}^2}{3} + \frac{1}{2}(\frac{1}{3}E^{'} + \nu^{'})\sigma_{ii}^2 - C(T)\} + \sigma_{ij}\epsilon_{ij}^{ori} - (\Gamma + b)z - a(1-z) \\ -[(\alpha - \beta)z + \frac{\beta}{2}](\frac{2}{3}\epsilon^{ori}\epsilon^{ori}) \tag{4.6}$$

where

$$E^{'} = \frac{(1+\nu)(E_A - E_M)}{E_A E_M} \quad , \quad \nu^{'} = \frac{\nu(E_M - E_A)}{E_A E_M} \tag{4.7}$$

$$\epsilon_{ij}^{ori} = \frac{3}{2}\epsilon_0\frac{\sigma_{ij}^d}{\sigma_{eqv}} \tag{4.8}$$

where σ_{ij}^d is the deviatoic part of the stress tensor, and

$$a = \frac{1}{2}\big[(\frac{1}{E_M} - \frac{1}{E_A})\frac{(\sigma^{MS})^2 - (\sigma^{AF})^2}{2} + (\sigma^{MS} - \sigma^{AF})\epsilon_0\big] \\ b = \frac{1}{2}\big[(\frac{1}{E_M} - \frac{1}{E_A})\frac{(\sigma^{MF})^2 - (\sigma^{AS})^2}{2} + (\sigma^{MF} - \sigma^{AS})\epsilon_0\big] \tag{4.9}$$

α, β, Γ, ζ, and $C(T)$ are calculated as follows:

$$\alpha = \frac{\sigma^{RF} - \sigma^{RS}}{\epsilon_0} \tag{4.10}$$

$$\beta = \frac{\sigma^{RF}}{\epsilon_0} \tag{4.11}$$

$$\Gamma = \frac{1}{2}\big[(\frac{1}{E_M} - \frac{1}{E_A})\frac{(\sigma^{MF})^2 - (\sigma^{MS})^2 + (\sigma^{AS})^2 - (\sigma^{AF})^2}{2} \\ +(\sigma^{MF} - \sigma^{MS} + \sigma^{AS} - \sigma^{AF})\epsilon_0 - 2(\alpha - \beta)\epsilon_0^2\big] \tag{4.12}$$

$$C(T) = \zeta(T - A_f^0) + \kappa \tag{4.13}$$

σ^{RS} and σ^{RF} are start and finish stresses for the orientation of the martensite phase, and

$$\kappa = \alpha - \beta\frac{\epsilon_0^2}{2} \tag{4.14}$$

$$\zeta = \frac{C(T_0)-\kappa}{T_0 - A_f^0} \tag{4.15}$$

with

$$C(T_0) = \frac{1}{2}\big[\big(\frac{1}{E_M} - \frac{1}{E_A}\big)\frac{(\sigma^{MS})^2 + (\sigma^{AF})^2}{2} + (\sigma^{MS} + \sigma^{AF})\epsilon_0 - \beta\epsilon_0^2\big] \tag{4.16}$$

4.2. Calculation of the Transformation Region

Hazar *et al.* [25] used the transformation function in Equation 4.6 together with the asymptotic stress equations of Williams to estimate the extent of the transformation region. The function used by Hazar *et al.* is given below [25]:

$$F_z^{LEFM} = E^{'}\frac{K_I^2}{12\pi r}[1 + cos(\theta) + \frac{3}{2}sin^2(\theta)] + \frac{1}{2}(\frac{1}{3}E^{'} + \nu^{'})\frac{K_I^2}{\pi r}(1 + cos(\theta)) - C(T)$$
$$+\epsilon_0\frac{K_I}{2\sqrt{\pi r}}\sqrt{[1 + cos\theta + \frac{3}{2}sin^2(\theta)]} - (\Gamma + b)z - a(1 - z) - ((\alpha - \beta)z + \frac{\beta}{2})\epsilon_0^2 = 0 \tag{4.17}$$

Although the equations of Williams have problems in representing the stress distribution in a transformed region, the proposed method provided a relatively good approximation to the transformation region size. Because HRR solution seems to be more suitable to characterize the crack tip fields in an SMA, a similar approach is followed using the asymptotic equations of HRR. Also, using HRR, a more successful evaluation of the full martensitic region is expected.

Stresses in Equation 2.23 are inserted into Equation 4.6 and the following transformation function, F_z is obtained:

$$\begin{aligned} F_z^{HRR} &= K^2\sigma_y^2(r^{s-2})^2[\frac{E^{'}\tilde{\sigma}_{eqv}^2}{3}+\frac{1}{2}(\frac{1}{3}E^{'}+\nu^{'})(\tilde{\sigma}_{rr}+\tilde{\sigma}_{tt})^2]-C(T) \\ &+K\sigma_y\frac{3}{2}\frac{\epsilon_0}{\tilde{\sigma}}_{eqv}[\tilde{\sigma}_{rr}^2+2\tilde{\sigma}_{rt}^2+\tilde{\sigma}_{tt}^2-\frac{1}{3}(\tilde{\sigma}_{rr}+\tilde{\sigma}_{tt})^2]-(\Gamma+b)z-a(1-z) \\ &-[(\alpha-\beta)z+\frac{\beta}{2}]\frac{3}{2}\frac{\epsilon_0^2}{\tilde{\sigma}_{eqv}^2}[\tilde{\sigma}_{rr}^2+2\tilde{\sigma}_{rt}^2+\tilde{\sigma}_{tt}^2-\frac{1}{3}(\tilde{\sigma}_{rr}+\tilde{\sigma}_{tt})^2]=0 \end{aligned} \tag{4.18}$$

During the phase transformation, $F_z = 0$; to evaluate the boundaries of martensitic transformation, Equations 4.17 and 4.18 will be solved for r using MATLAB: $z = 0$ is used to calculate the radius of transformation region (r_{tr}) and $z = 1$ is used for the radius of full martensite region (r_m).

Transformation stresses σ^{MS}, σ^{MF}, σ^{AS} and σ^{AF} are determined following the method proposed by Maletta and Furgiuele [40] as shown in Figure 4.1. As a result, $\sigma^{MS} = 412$ MPa, $\sigma^{MF} = 424$ MPa, $\sigma^{AS} = 185$ MPa and $\sigma^{AF} = 135$ MPa are obtained. Additionally, $\epsilon_0 = 4\%$ is calculated.

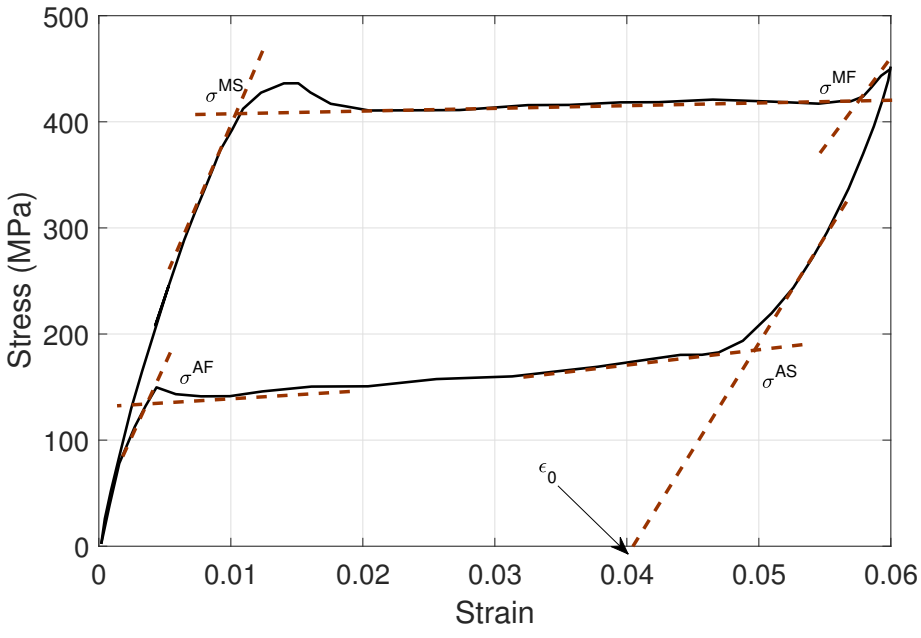

Figure 4.1. Transformation stresses σ^{MS}, σ^{MF}, σ^{AS} and σ^{AF}

It is shown in some numerical and experimental studies in the literature [41, 42] that the ratio of axial and transverse strains approaches 0.5 during the martensitic transformation similar to volume preserving plastic deformation. Because the inelastic strains are dominant in the transformation zone, $\nu = 0.5$ is used in F_z^{HRR}. On the other hand, $\nu = 0.33$ is used in F_z^{LEFM} because it is based on the linear portion of the stress-strain relation where Poisson's ratio is observed to be around 0.33 in general [41, 42].

4.3. Results and Discussion

Transformation region estimations obtained using F_z^{HRR} and F_z^{LEFM} are plotted in Figure 4.2 and Figure 4.3. Transformation region size on the x-axis is estimated to be around 1 mm from both approaches. The result overlaps with the experimental observation of Haghgouyan *et al.* [8]. On the other hand, estimations of the full martensite region using F_z^{HRR} and F_z^{LEFM} are quite different. It is observed that the full martensite region estimated by using F_z^{LEFM} is extremely large. It is almost equal to the transformation region size. Although it could not be measured exactly, it is observed by Haghgouyan *et al.* [8] that full martensite region is very small compared to the trasnformation region.

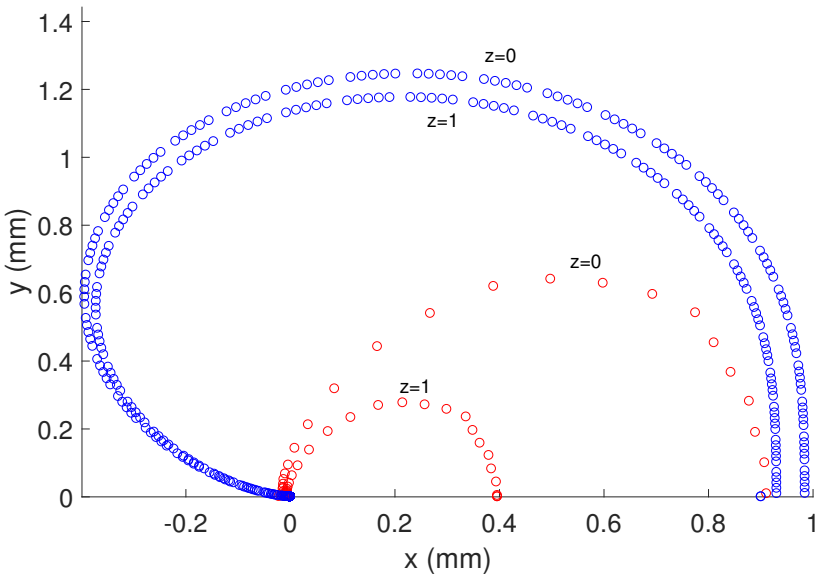

Figure 4.2. En of transformation zone ($z = 0$) and size of martensitic region ($z = 1$) estimations using F_z^{HRR} (red points) and F_z^{LEFM} (blue points)

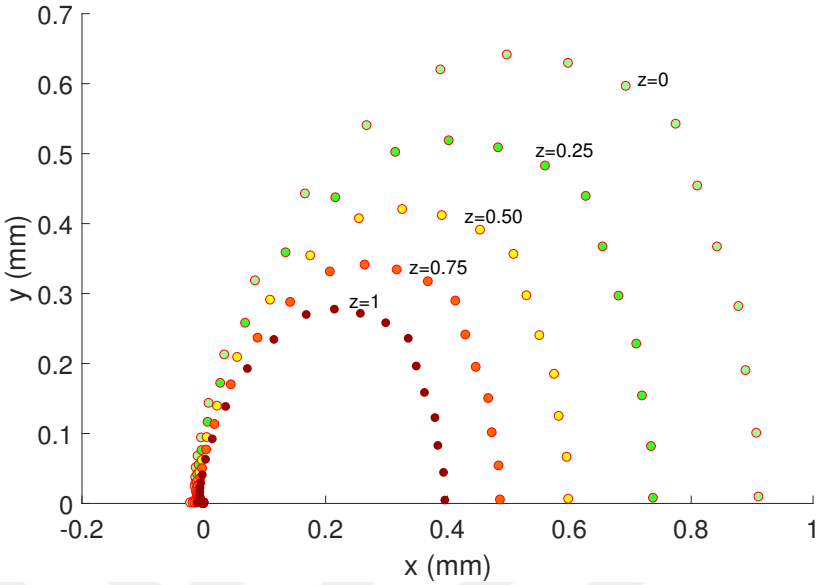

Figure 4.3. Volume fraction contours calculated using F_z^{HRR}

In order to investigate the transformation region, Haghgouyan *et al.* [8] used the equivalent strain around the crack tip obtained as follows:

$$\epsilon_{eqv} = \sqrt{\frac{2}{3}\boldsymbol{e} : \boldsymbol{e}} \tag{4.19}$$

where $\boldsymbol{e}$ is the deviatoric strain tensor calculated using the displacement field obtained from DIC. Using Equation 4.19, Haghgouyan *et al.* obtained the equivalent strain contour plots as shown in Figure 4.4. Maximum measurable strain was around 4% due to the resolution of the measurement devices while 5.8% strain was required to estimate the fully transformed region size. They reported 0.18 mm full martensite region suggested by complementary FE analysis performed using Auricchio's built-in model in ABAQUS.

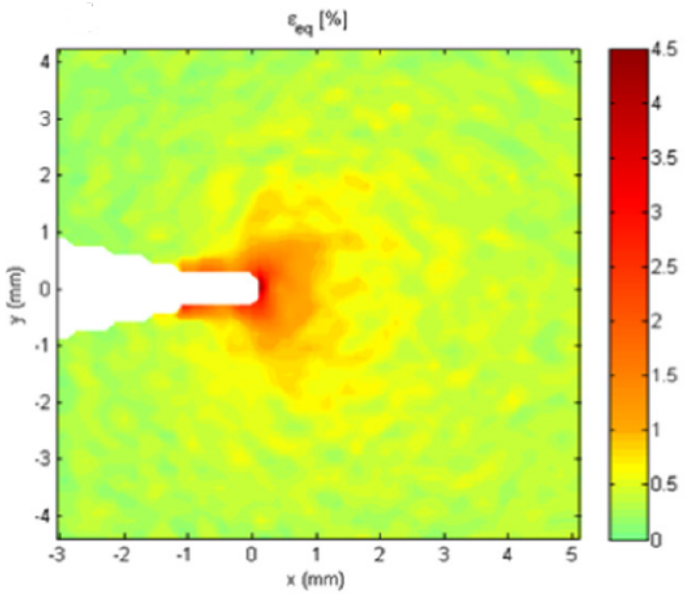

Figure 4.4. DIC measured contour plot of ϵ_{eqv} [8]

Similar to Haghgouyan *et al.* [8], transformation region size is also estimated from equivalent strain using the asymptotic equations of Williams and HRR. Strains are calculated from stresses according to the constitutive relations: Hooke's law for Williams and Ramberg-Osgood relation for HRR. Equivalent strain contours are plotted in Figure 4.5.

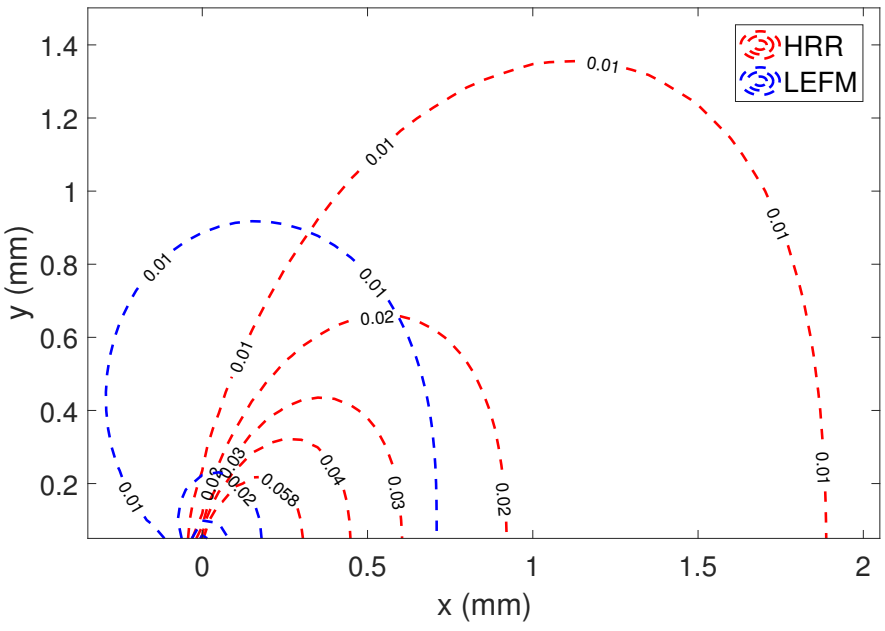

Figure 4.5. ϵ_{eqv} distribution around crack tip (HRR vs Williams)

According to the asymptotic equations of Williams, transformation region is estimated to be around 0.7 mm, on the other hand, no fully transformed region is detected since strain values do not reach 5.8%. This indicates that the asymptotic equations of Williams are not suitable to evaluate the strain distribution inside the transformation region. According to HRR, a larger transformation region is estimated which is around 1.9 mm. Additionally, around 0.3 mm full martensite region is estimated.

Transformation region estimations obtained using the transformation functions and ϵ_{eqv} are listed in Table 4.1. In general, the estimation of full martensitic region using HRR equations gives more reasonable results than those of Williams. On the other hand, asymptotic equations of Williams provide closer results to the experimental ones for the transformation region.

Table 4.1. Transformation and martensitic region estimations (mm) according to ϵ_{eqv}

		r_{tr} (mm)	r_m (mm)
F_z	HRR	0.9	0.4
	Williams	1	0.9
ϵ_{eqv}	HRR	1.9	0.3
	Williams	0.7	-

5. COMPUTATIONAL EVALUATION OF CRACK TIP FIELDS AND TRANSFORMATION REGION

In this chapter, the edge cracked problem is studied using finite elements. Crack tip singularity fields and the transformation region are obtained using the built-in Auricchio model and a separate UMAT written to implement the ZM model in ABAQUS. The stress distribution, the size of the transformation and martensitic regions around the crack tip are obtained from finite elements and the results are compared to the results obtained from asymptotic equations. Three different Nitinol properties, each having different transformation stresses as shown in Table 5.1 are modeled. The material properties are taken from experimental works of Mutlu [32] and Gou [33].

Table 5.1. Mechanical properties of Nitinol used

	E_A (GPa)	E_M (GPa)	σ^{MS} (MPa)	σ^{MF} (MPa)
Material 1	62	45	501	549
Material 2	62	45	523	684
Material 3	30.34	18	411	663

ZM Model requires additional properties; corresponding material properties used in the ZM model are listed in Tables 5.2, 5.3 and 5.4. First, the uni-axial tensile tests are simulated in ABAQUS to check the model, the fracture tests are simulated afterwards.

Table 5.2. Material properties used in the ZM model for the 1^{st} material

Parameter	Value	Parameter	Value
E_A	62000 MPa	a	11.2129 MPa
E_M	45000 MPa	b	11.3576 MPa
ν	0.33	ϵ_0	0.06
Y	110 MPa	G	9.4889 MPa
α	1833.3 MPa	β	3666.7 MPa
ζ	4.1994 MPa K^{-1}	κ	4.6129 MPa
A_f^0	297.15 K	T_0	299.15 K

Table 5.3. Material properties used in the ZM model for the 2^{nd} material

Parameter	Value	Parameter	Value
E_A	62000 MPa	a	14.8138 MPa
E_M	45000 MPa	b	16.5156 MPa
ν	0.33	ϵ_0	0.06
Y	110 MPa	G	15.1503 MPa
α	1833.3 MPa	β	3666.7 MPa
ζ	1.2928 MPa K^{-1}	κ	8.2138 MPa
A_f^0	297.15 K	T_0	299.15 K

Table 5.4. Material properties used in the ZM model for the 3^{rd} material

Parameter	Value	Parameter	Value
E_A	30340 MPa	a	5.16 MPa
E_M	18000 MPa	b	6.36 MPa
ν	0.33	ϵ_0	0.04
Y	30 MPa	G	13.17 MPa
α	500 MPa	β	1250 MPa
ζ	0.20 MPa K^{-1}	κ	4.16 MPa
A_f^0	300 K	T_0	340 K

5.1. Computational Modeling of Tensile Tests Specimen

The dog-bone tensile test specimen of Nitinol is modeled using a UMAT subroutine written for the ZM model to account for thermomechanical coupling. The geometry and the dimensions of the specimen are shown in Figure 5.1. The specimen is fixed from one side, and around 5 mm displacement is applied quasi-statically to the other side. The analyses are performed with eight-node thermally coupled brick, tri-linear elements. Since the asymptotic equations do not include the effect of temperature, an exagerated convection coefficient ($h = 100\ W/m^2K$) is used in order to transfer the latent heat from the material immediately. In this way, the temperature of the material is kept constant.

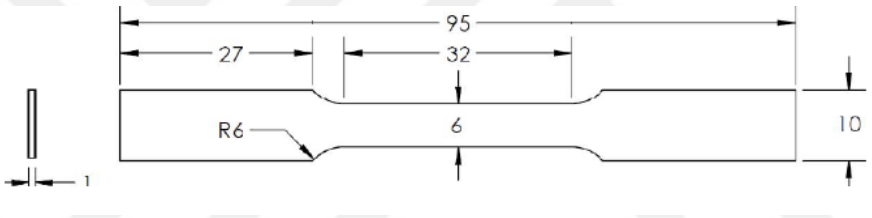

Figure 5.1. Dimension (mm) of the dog-bone specimen

Stress-strain diagrams are plotted using the data obtained from nodes in the fully transformed region of the model. Because temperature is kept constant, a sharp transformation point is observed in stress-strain diagrams; in other words, there is no yield off-set. For that reason, the mechanical constants, α and n, in the Ramberg-Osgood equation are obtained by trying to find the best curve fit. Stress-strain diagrams of the materials and the curves fitted are shown in Figures 5.2, 5.3 and 5.4. $n = 20$, $n = 8$ and $n = 4$ are used in the Ramberg-Osgood equation.

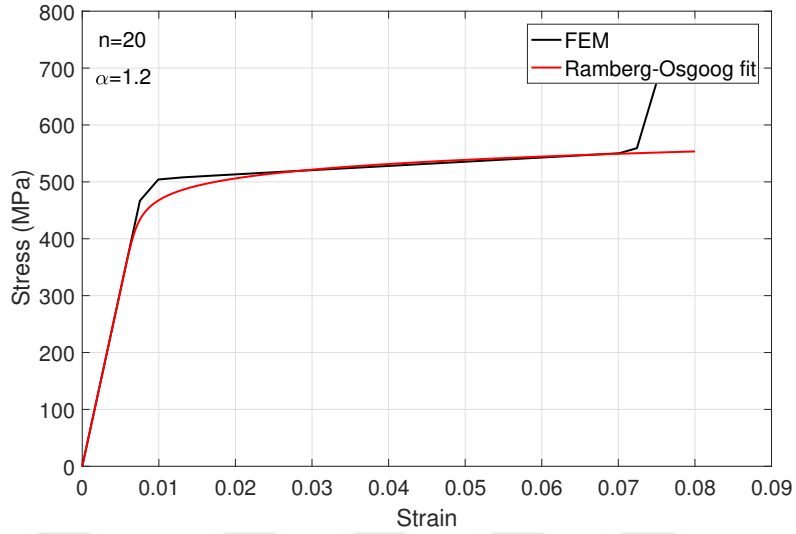

Figure 5.2. Stress-strain diagram of the 1^{st} material

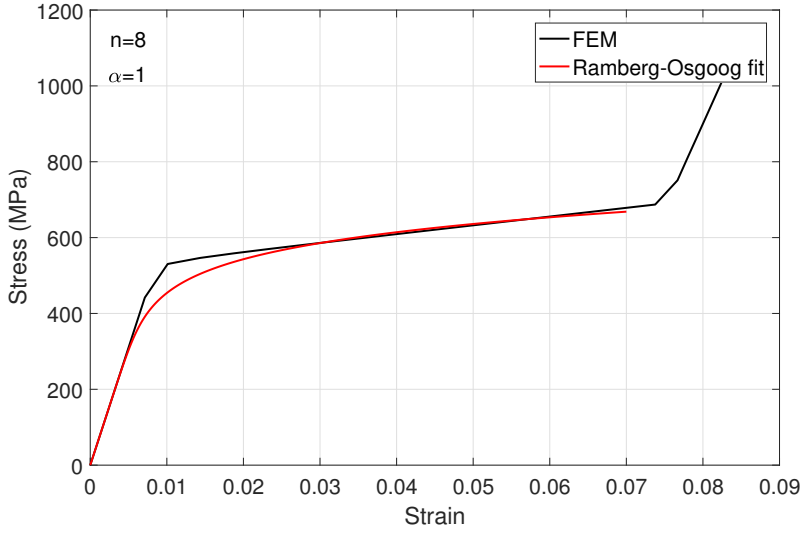

Figure 5.3. Stress-strain diagram of the 2^{nd} material

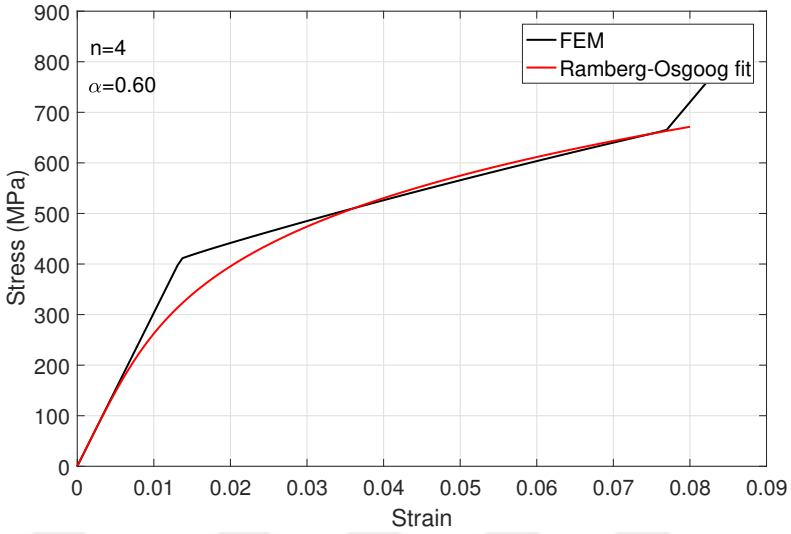

Figure 5.4. Stress-strain diagram of the 3^{rd} material

The transformation plateaus have different slopes as a result of different mechanical properties. The figures shpw that n decreases with increasing slope similar to the effect of the level of hardening on elastic-plastic materials. It is also observed that the representation of the stress-strain relation of an SMA with the Ramberg-Osgood equation is better accomplished for larger ns; in other words, for SMAs with smaller slopes in the transformation plateau. For smaller ns, however, the deviation from the real curve is larger around the transformation start stress (σ^{MS}).

5.2. Computational Modeling of The Edge Cracked Specimen

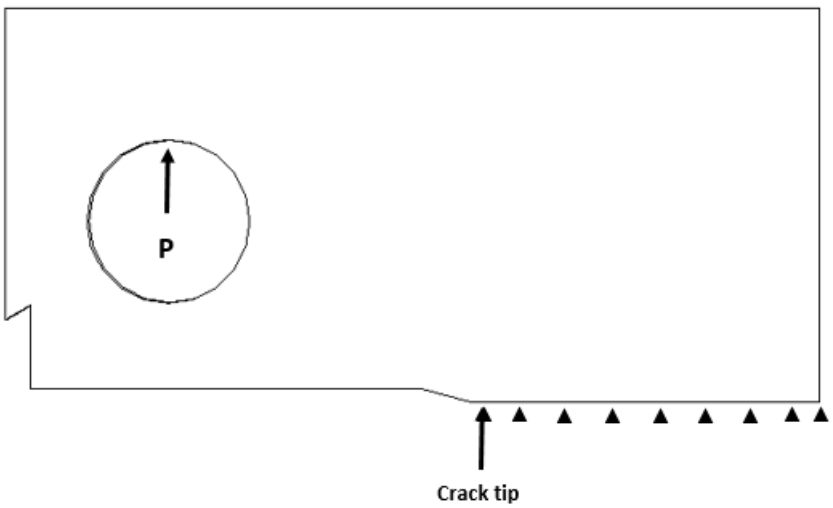

Figure 5.5. Geometry of the finite element model for fracture tests

The SMA plate given in Section 3.4 is modeled using ABAQUS and the UMAT written for the ZM model. Only top-half plate is considered using the symmetry in the model. Material properties in Tables 5.2, 5.3 and 5.4 are used for each CT specimen. $P_1 = 420$ N, $P_2 = 514$ N and $P_3 = 300$ N are applied in the y-direction to the pin hole as shown. Analyses are performed with eight-node thermally coupled brick tri-linear elements. The mesh density increases near the crack tip as shown in Figure 5.6 because pseudoelastic phase transformation occurs in this region. Again, the temperature is kept constant using a very large convection coefficient.

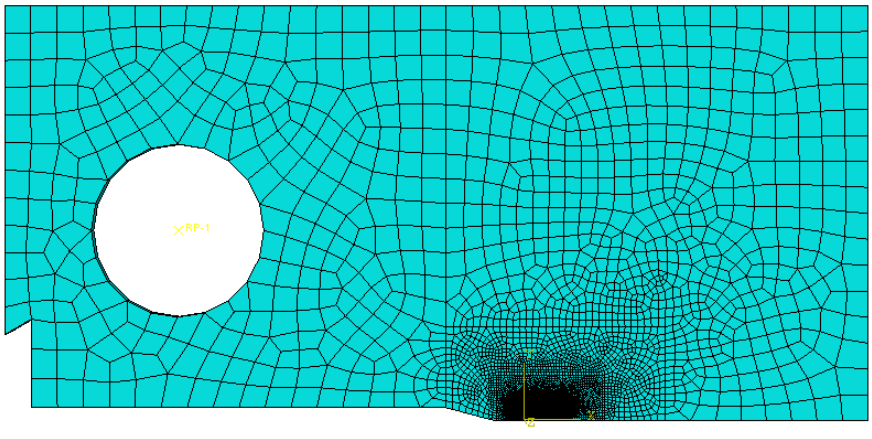

Figure 5.6. Mesh on CT specimen

5.2.1. Evaluation of Fracture Parameters

J-integrals are calculated on different contours around the crack tip using finite elements. Although J is path-independent for nonlinearly elastic materials, J-integral is observed to be path-dependent in the case of Nitinol. The value of it decreases as the distance from the crack tip increases, in other words, as the elastic region dominates. For that reason, averages of the J-integral at the tip (J^{tip}) and far field value (J^{∞}) are used in calculations. The stress intensity factor, K_I, and the amplitude of the stress function in HRR singularity, κ, are calculated using Equations 2.32 and 2.33. As a result, fracture parameters used in asymptotic stress equations are shown in the table below.

Table 5.5. Fracture parameters

	$\frac{(J^{tip}+J^{\infty})}{2}$ (N/m)	K_I $(MPa\sqrt{m})$	κ
Model 1	20	35.92	0.90
Model 2	25	39.37	0.80
Model 3	17.5	23.04	0.65

5.2.2. Evaluation of Crack Tip Fields

Full-field stress distributions are obtained from ABAQUS using both Auricchio and ZM models. As expected, in each model, highest stress values are observed around the crack tip. The equivalent stress distributions around the crack tip obtained from finite elements are compared to the results calculated from asymptotic equations of Williams and HRR.

In Figures 5.7, 5.8 and 5.9 the equivalent stress contours around the crack tip are plotted using the finite element results and the results from asymptotic equations. Crack tip is located at the origin and the crack faces lie on the negative x-axis. The results show that in the transformation zone, the equivalent stress contours obtained from HRR show a good agreement with the results obtained from finite elements. Towards the crack tip, the equivalent stress values calculated using the equations of Williams

increase abruptly. In reality, the phase transformation in SMAs limits the increase in stress around the tip which is also seen in the finite element results. Stresses can raise substantially only in the full martensite region where almost a finite deformation exists.

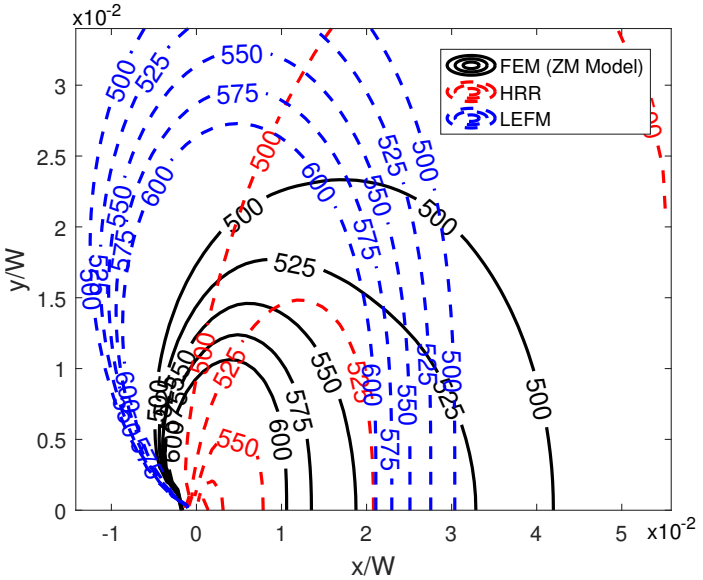

Figure 5.7. Comparison of equivalent stress distribution around the crack tip of the 1^{st} model

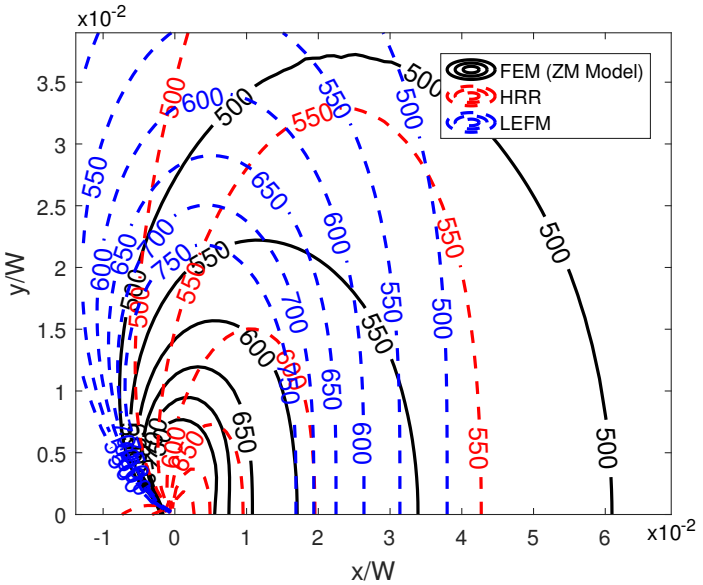

Figure 5.8. Comparison of equivalent stress distribution around the crack tip of the 2^{nd} model

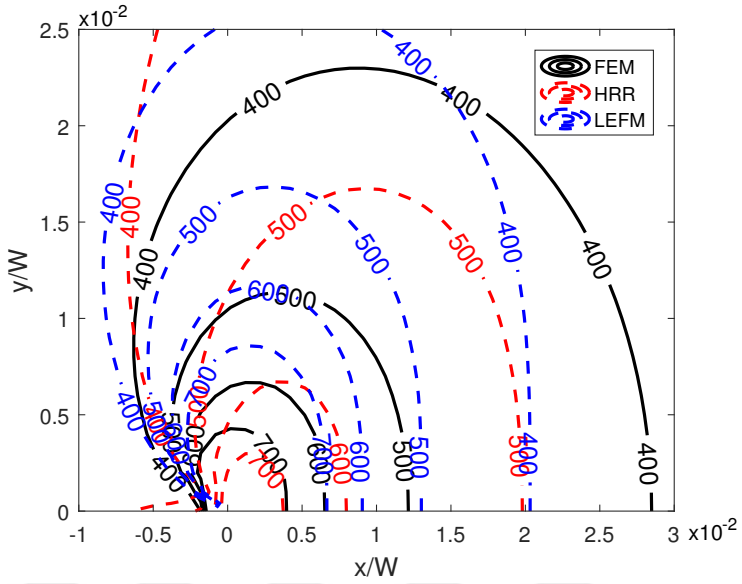

Figure 5.9. Comparison of equivalent stress distribution around the crack tip of the 3^{rd} model

In Figures 5.10, 5.11 and 5.12 opening stress vs distance from the crack tip are plotted; stresses are normalized by the transformation start stresses (σ^{MS}) of each material. It is observed that the results of HRR match with finite element results in the transformation region except for the third model. As noted before, curve fitting of the Ramberg-Osgood equation to stress-strain relation of the third model was less successful than the others. It is also seen that, outside the transformation zone where the material is linearly elastic, finite element results approach the LEFM results. These results are consistent with the ones reported in the literature in case of small scale transformation.

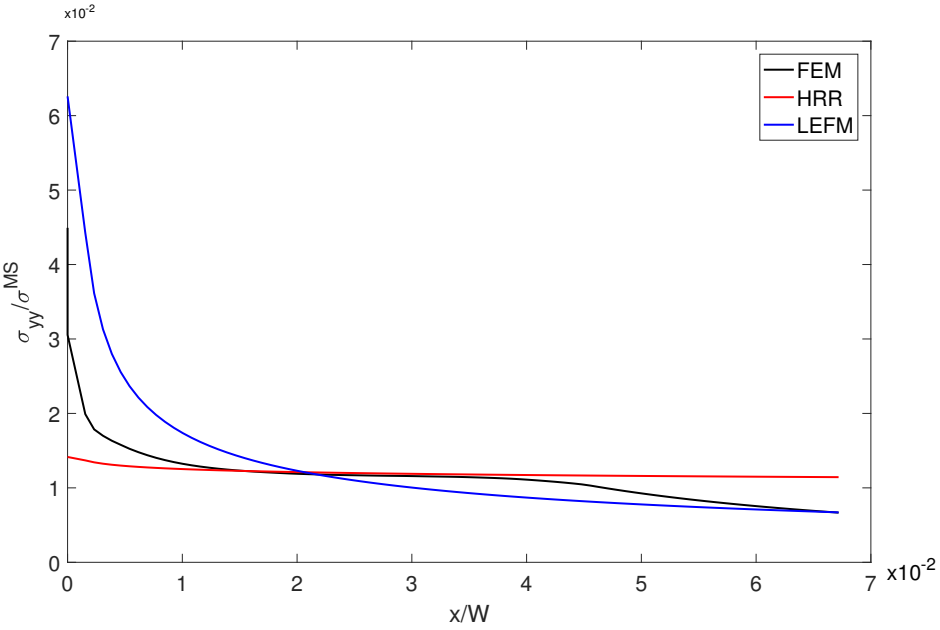

Figure 5.10. Comparison of opening stress distribution ahead of the crack tip, 1^{st} model

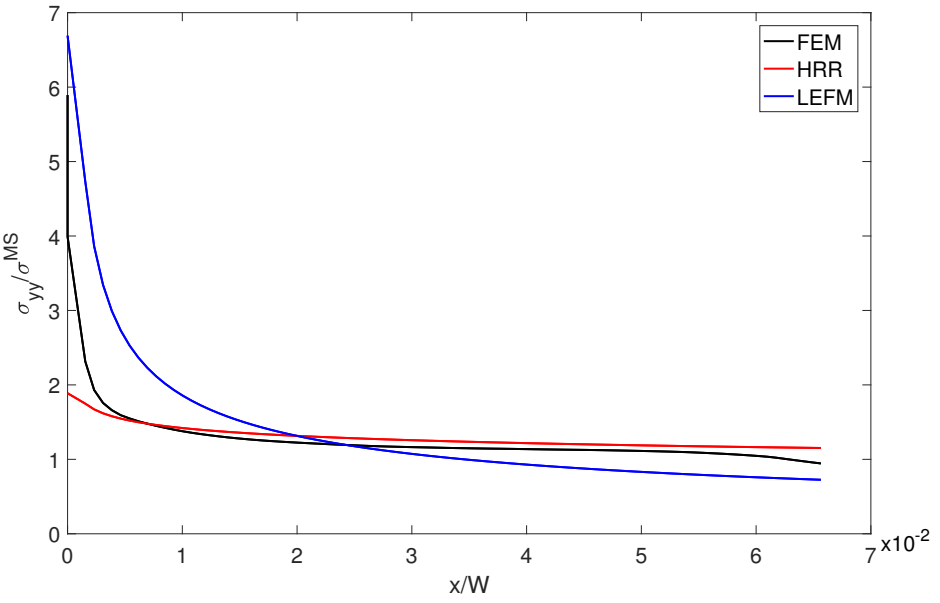

Figure 5.11. Comparison of opening stress distribution ahead of the crack tip, 2^{nd} model

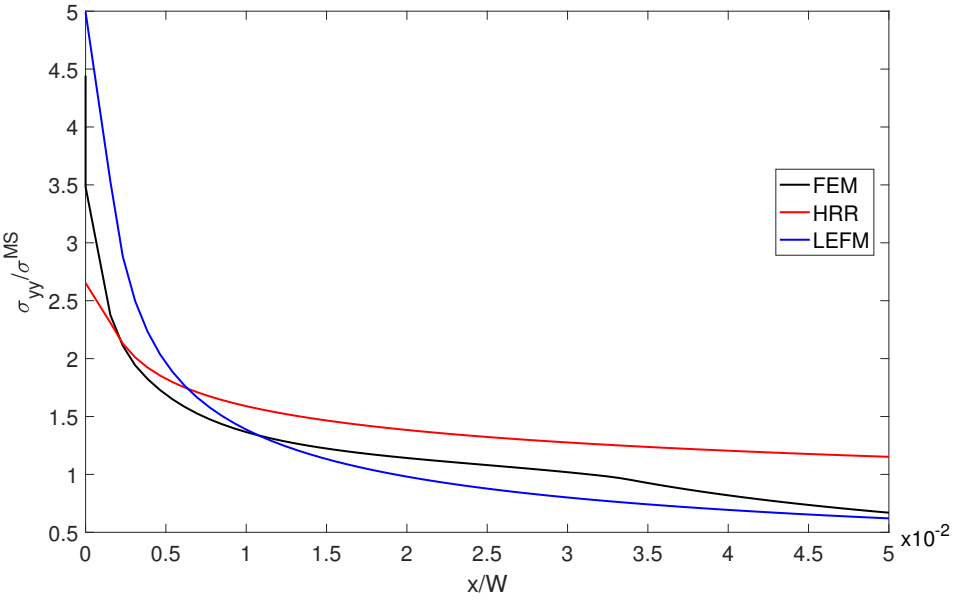

Figure 5.12. Comparison of opening stress distribution ahead of the crack tip, 3^{rd} model

From the results it is possible to note a few remarks on the dominance of asymptotic equations. Figure 5.13 shows the effect of plasticity level on crack tip fields in elastic-plastic materials. Around the crack tip of an SMA, a similar distribution is observed as a result of martensitic transformation as shown in Figure 5.14. In the present study, large strains may generate in the fully transformed region, and asymptotic equations do not work in this region. In the transformation region, it is observed that HRR solution has a strong dominance, therefore this region can be named as the J-dominant region. In addition, K-dominance is observed in the region where the material is in fully austenite (elastic) phase.

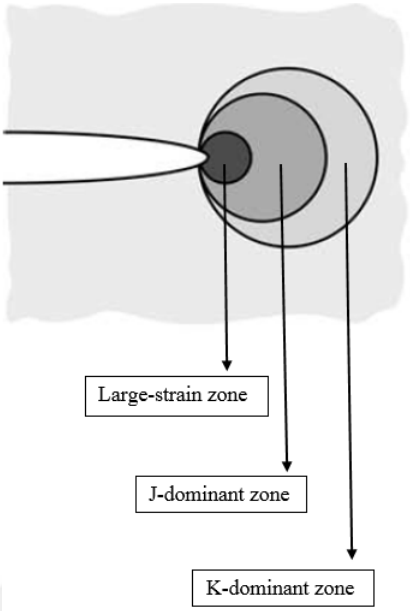

Figure 5.13. Crack tip dominant zones in an elastic-plastic material [5]

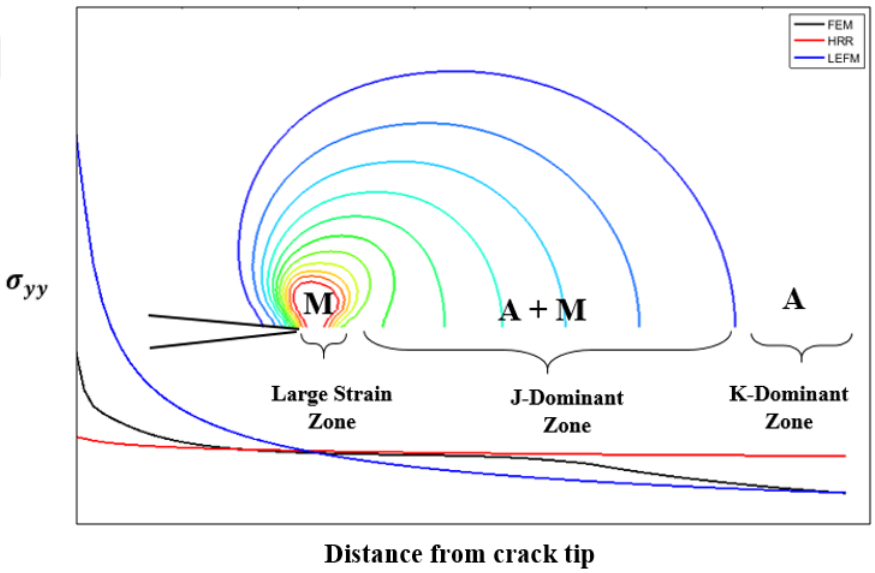

Figure 5.14. Crack tip dominant zones in an SMA

5.2.3. Evaluation of Transformation Regions

Results of transformation and martensitic regions obtained from ABAQUS are compared to the results obtained by using Equations 4.17 and 4.18 (F_z^{LEFM} and F_z^{HRR}). Results of comparison are plotted in Figures 5.15, 5.16 and 5.17. It is ob-

served that the calculation of the transformation region with the implementation of the asymptotic equations of Williams and HRR into the transformation function of ZM model gives reasonable results in the case of the first and the second models. However, there are significant differences when the full martensite region is evaluated using asymptotic equations. As it is seen from the figures, full martensite region sizes obtained from finite elements are very small. Estimation of the full martensite region using F_z^{HRR} gives closer results to the computational ones. Results from F_z^{LEFM} give large martensitic region size compared to the computational results. At the same time, there is a very small difference between the transformation region and the full martensite region sizes when they are calculated with F_z^{LEFM}.

From Figure 5.17, it is observed that the estimation of the transformation region of the third model using F_z^{LEFM} gives a better result than that of F_z^{HRR}. Also, it is seen that the difference between the transformation and the martensite region sizes calculated with F_z^{LEFM} increases from model 1 to model 3. The reason behind that is the increase in the slope of the transformation plateau, in other words, decrease in the value of n. The material behavior converges to the linear-elastic response as n goes to zero. Therefore, HRR performes better for SMAs having smaller slopes during the transformation.

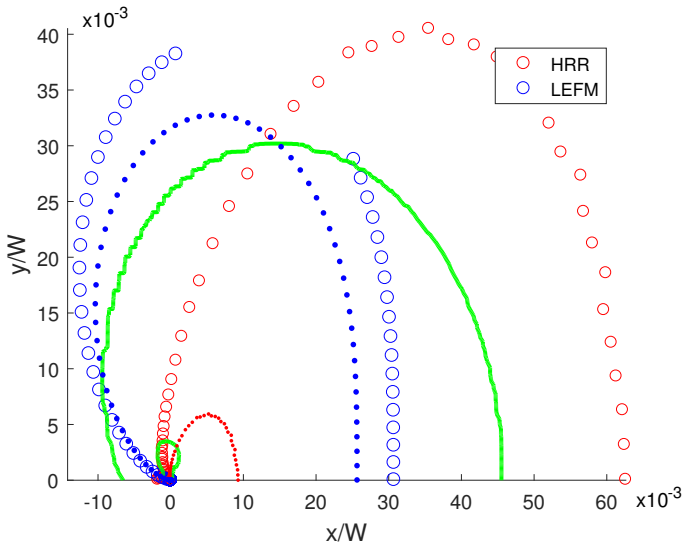

Figure 5.15. Comparison of the transformation and martensitic regions around the crack tip, 1^{st} model (green lines indicate finite element results)

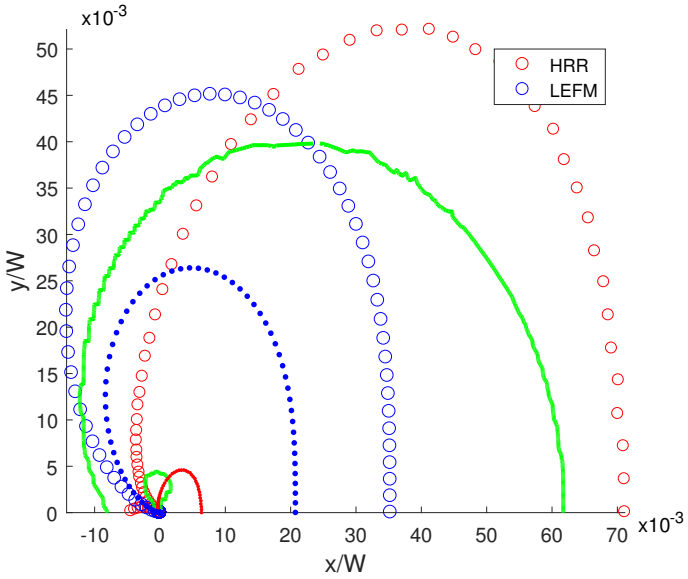

Figure 5.16. Comparison of the transformation and martensitic regions around the crack tip, 2^{nd} model (green lines indicate finite element results)

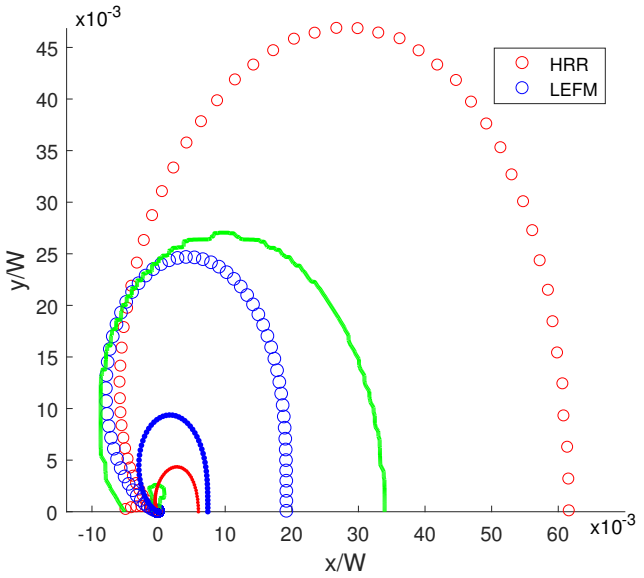

Figure 5.17. Comparison of the transformation and martensitic regions around the crack tip, 3^{rd} model (green lines indicate finite element results)

5.2.3.1. The Effect of Thermomechanical Coupling on Transformation Region. Finite element analyses of the first and the second models are repeated in order to see the effect of thermomechanical coupling on the transformation region size. The edge cracked specimen is loaded following the experimentally applied loading rates provided by

Mutlu [32], and $h = 0.05\ W/m^2K$ is used for the convection coefficient. Figures 5.18 and 5.19 show the heat fluxes in the direction perpendicular to the plate surfaces obtained from ABAQUS. It is observed that there is a substantial difference between heat fluxes around the crack tip when $h = 0.05\ W/m^2K$ and $h = 100\ W/m^2K$ are used.

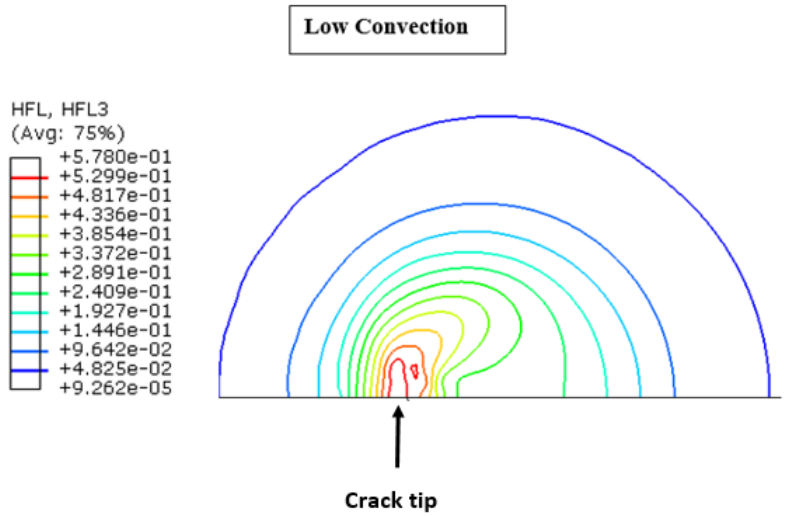

Figure 5.18. Heat flux (mW/mm^2) around the crack tip with $h = 0.05\ W/m^2K$

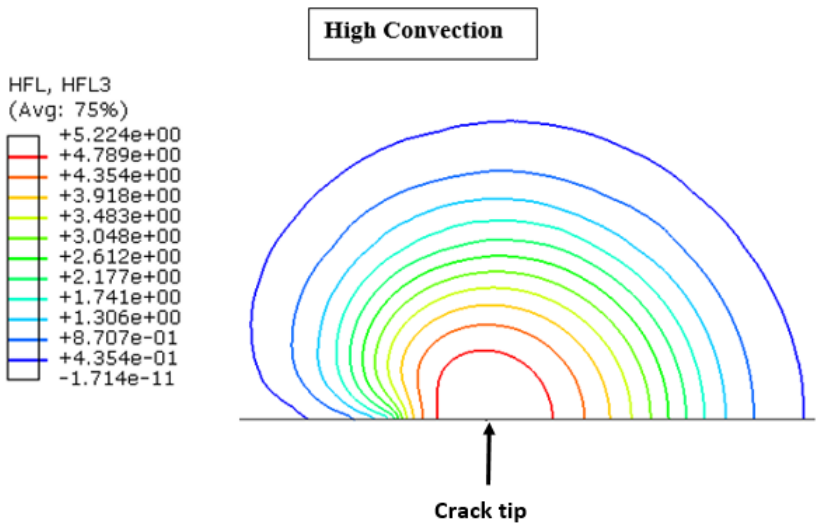

Figure 5.19. Heat flux (mW/mm^2) around the crack tip with $h = 100\ W/m^2K$

When $h = 0.05\ W/m^2K$ is used, the temperature around the crack tip increases. Because an increase in temperature results in an increase in the transformation stresses,

transformation region around the crack tip decreases. Transformation region sizes obtained from the coupled and uncoupled models are listed in Table 5.6. Transformation region decreases with the inclusion of coupling as it is expected. It is observed that the effect of thermomechanical coupling is greater in model 2 because the loading rate in the second model (2 mm/min) is four times the loading rate (0.5 mm/min) in the first model (the effect of thermomechanical coupling is stronger in higher loading rates [32]).

Table 5.6. Effect of thermomechanical coupling on transformation region size

	r_{tr} (Uncoupled)	r_{tr} (Coupled)	Difference
Model 1	1.17 mm	1.12 mm	4.3 %
Model 2	1.61 mm	0.93 mm	42.2 %

The results indicate that equations of HRR can be used in SMAs under quasi-static loading conditions where the change in temperature is small relatively. In higher strain rates, thermomechanical coupling of SMAs has a significant effect on the crack tip fields.

5.2.4. Sensitivity of Transformation Region Estimation on Mechanical Constant n

In computational analysis, mechanical constants, α and n, of the Ramberg-Osgood equation are determined by trying to find the best fit to the stress-strain curve obtained from finite elements and the value of n which better represents the slope in the transformation plateau is chosen; once n is determined α is arranged accordingly. To study the sensitivity of the transformation region calculations on the mechanical constant n, the first and the second models are reconsidered. For the first model, the value of n was found to be 20, on the other hand, it was 8 for the second model. To see the effect of the hardening coefficient, n, on the results, values of n between 15-25 are used for the first model and the resulting transformation and martensitic region sizes are tabulated in Table 5.7. The same is repeated for the second model, for n s between 5 and 11 and the results are presented in Table 5.8.

Table 5.7. Transformation and martensitic region sizes calculated with different n values for the first model ($n = 20$ was used)

n	r_{tr} (mm)	r_m (mm)	% change in r_{tr}	% change in r_m
15	1.397	0.323	3.25	52.36
17	1.416	0.273	1.94	28.77
19	1.437	0.231	0.48	8.96
20	1.444	0.212	-	-
21	1.452	0.194	0.55	8.49
23	1.461	0.163	1.18	23.11
25	1.466	0.136	1.52	35.85

Table 5.8. Transformation and martensitic region sizes calculated with different n values for the second model ($n = 8$ was used)

n	r_{tr} (mm)	r_m (mm)	% change in r_{tr}	% change in r_m
5	0.964	0.195	11.88	95
7	1.057	0.125	3.38	25
8	1.094	0.1	-	-
9	1.126	0.079	2.93	21
11	1.193	0.049	9.05	51

It is observed that the estimation of full martensitic region is more sensitive to the constant n when compared to the estimation of transformation region because the change in n results in a more significant change in stress at the end of the transformation plateau. Figure 5.20 shows the stress-strain curves obtained when $n = 7$, $n = 8$ and $n = 9$ are used in the Ramberg-Osgood equation for the second model. It is also observed that the effect is more crucial for smaller n's; there is no such difference between the stress-strain curves of the first model when $n = 19$, $n = 20$ and $n = 21$ are used. As a result, estimation of the full martensitic region is considerably sensitive to the constant n especially for smaller n's, in other words, for the SMAs having larger slopes in the transformation plateau.

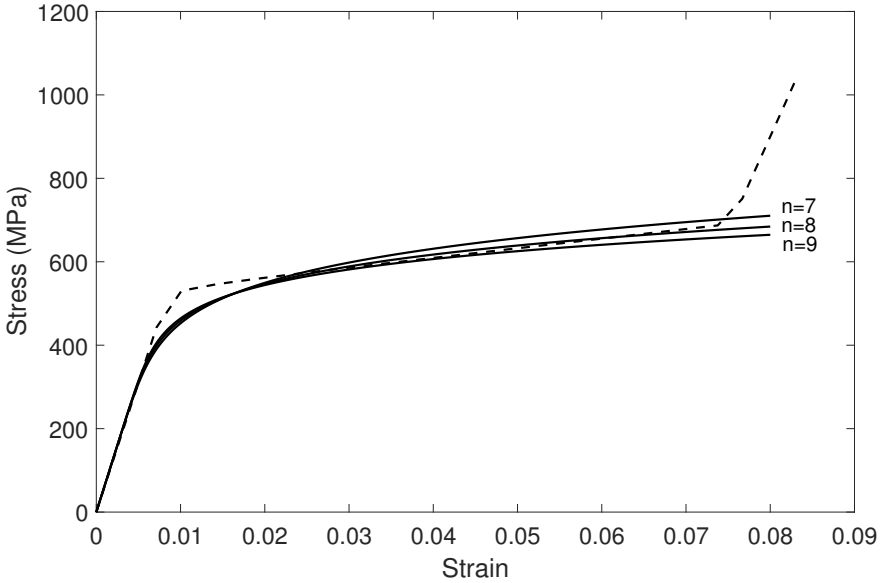

Figure 5.20. Ramberg-Osgood curve fit (solid lines) to stress-strain curve of the second model (dashed line) with different n's

6. ON J-INTEGRAL AND ENERGY DISSIPATION IN SUPERELASTIC SHAPE MEMORY ALLOYS

6.1. Path Independent J Integral

As discussed in Chapter 2, as long as stresses increase monotonically, loading path of an elastic-plastic material is similar to that of a non-linearly elastic material. Therefore, if the deformation of an elastic-plastic material vs loading is considered to evolve like that of a nonlinearly elastic one, the J-integral can be used to characterize the crack tip fields in an elastic-plastic materials assuming that there is small scale deformation around the crack tip. Rice [5, 23] used the J contour integral to evaluate the crack tip fields in nonlinearly elastic materials.

Rice proved that for any homogeneous, elastic or elastic-plastic material treated with deformation theory of plasticity (non-linearly elastic behavior), the J-integral is path-independent [10,23]. To prove the path-independence of the J-integral, consider a closed curve Γ^* enclosing an area A^* as shown in Figure 6.1. Using divergence theorem, the line integral can be written as a surface integral as follows [5]:

$$\int_{\Gamma^*} (W dy - \sigma_{ij} n_j u_{i,x} ds) = \int_{A^*} \big[\frac{\partial W}{\partial x} - \frac{\partial}{\partial x_i}(\sigma_{ij} \frac{\partial u_i}{\partial x})\big] dx dy \tag{6.1}$$

Differentiating the strain energy density W with respect to x, the following relations are obtained:

$$\begin{aligned} \frac{\partial W}{\partial x} =& \frac{\partial W}{\partial \epsilon_{ij}} \frac{\partial \epsilon_{ij}}{\partial x} = \sigma_{ij} \frac{\partial \epsilon_{ij}}{\partial x} \\ =& \frac{1}{2} \sigma_{ij} \big[\frac{\partial}{\partial x}(\frac{\partial u_i}{\partial x_j}) + \frac{\partial}{\partial x}(\frac{\partial u_j}{\partial x_i})\big] \\ =& \sigma_{ij} \frac{\partial}{\partial x_j}\big(\frac{\partial u_i}{\partial x}\big) \quad (Since \quad \sigma_{ij} = \sigma_{ji}) \\ =& \frac{\partial}{\partial x_j}\big(\sigma_{ij} \frac{\partial u_i}{\partial x}\big) \quad (Since \quad \sigma_{ij,j=0}) \end{aligned} \tag{6.2}$$

It is seen from the equation above that the J-integral vanishes for any closed curve Γ^*, in other words $J = 0$ when evaluated on a closed path.

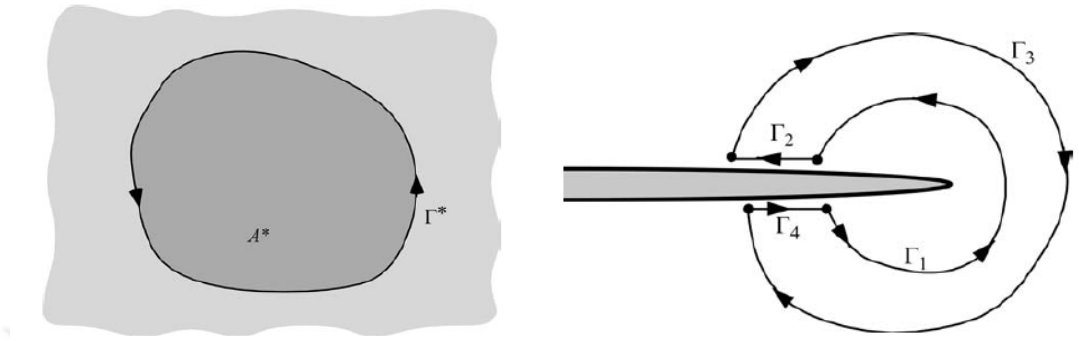

Figure 6.1. Closed J-integral contour around a crack tip [5]

If the J-integral is evaluated on a closed contour as shown in Figure 6.1, it can be written as the sum of each contribution, namely, Γ_1, Γ_2, Γ_3 and Γ_4, and the sum is equal to zero:

$$J = J_1 + J_2 + J_3 + J_4 = 0 \tag{6.3}$$

Since $\sigma_{ij} = dy = 0$ on crack surfaces, $J_2 = J_4 = 0$; as a result, $J_1 = -J_3$, and the path independence is shown.

It is shown in section 2.2.1 that J-integral is not path-independent in the case of an SMA as a result of dissipation and nonhomogeneity. To better understand the domain dependence of the J-integral, an edge cracked plate under tensile loading is modeled using finite elements (ABAQUS). Four different material types are considered: linearly elastic, nonlinearly elastic, plastic and SMA (NiTi). The geometry and the dimensions of the edge cracked specimen are shown in Figure 6.2. A very fine mesh is used around the crack tip as shown in the figure. Figure 6.3 shows the values of the J-integral calculated on different contours around the crack tip in a linearly elastic material. As expected, the J-integral reaches a constant value after a few contours from the crack tip (first 1-2 contours should be ignored due to some numerical problems [43]).

Next, a nonlinearly elastic material is studied using the deformation plasticity model of ABAQUS; J-integral results are shown in Figure 6.4. It is seen that J-integral is path-independent for nonlinearly elastic materials as well.

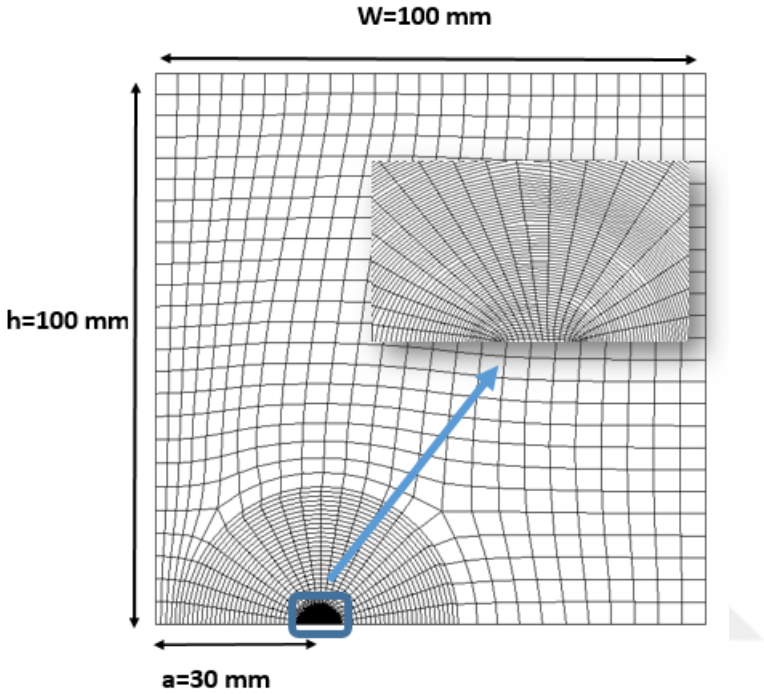

Figure 6.2. Mesh distribution on edge cracked specimen

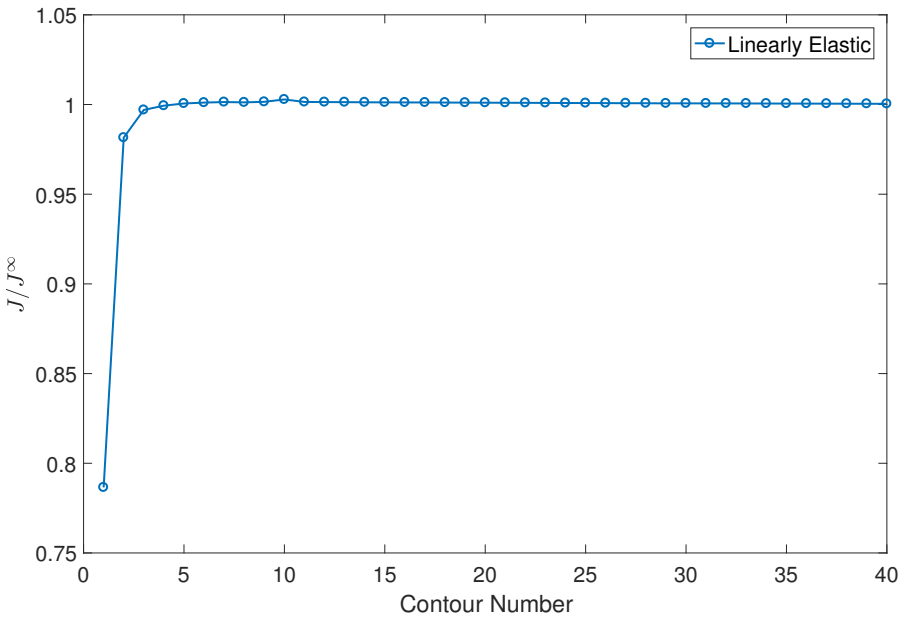

Figure 6.3. J-integral vs contour number in a linearly elastic material

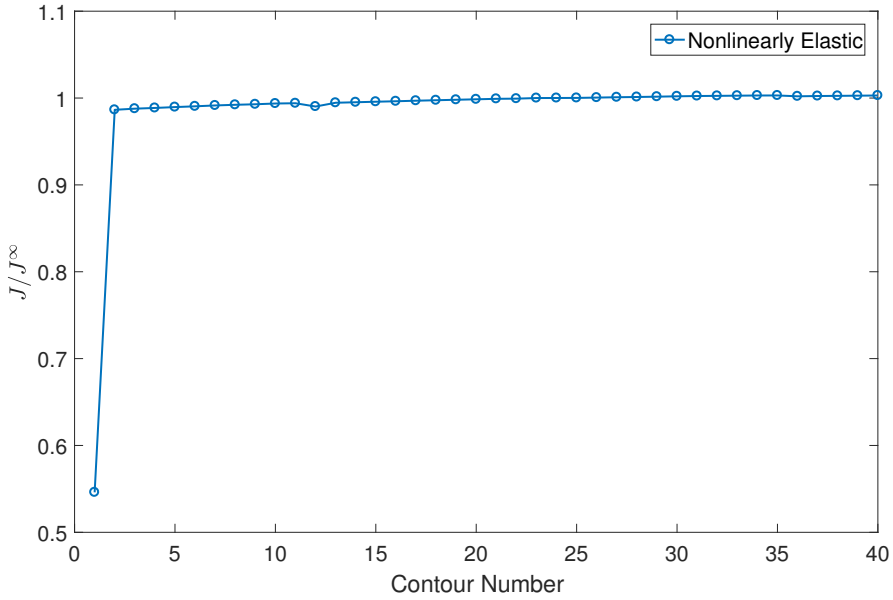

Figure 6.4. J-integral vs contour number in a nonlinearly elastic material

In the case of an SMA, J-integral is path-dependent due to energy dissipation and non-homogeneity resulting from martensitic transformation [44]. Figure 6.5 shows J-integral values around the crack tip in a pseudoelastic NiTi plate obtained using ZM and Auricchio models. It is shown that almost a path-independent J-integral is observed when Auricchio's model is used. It is an expected result because Auricchio model does not include thermomechanical coupling in the SMAs and there is no energy dissipation in the form of heat; free energy density is defined as the elastic strain energy density [45], and stress is derived from the strain energy density as shown by Equation 6.2. Therefore, loading of an SMA using Auricchio's model resembles to the loading of a nonlinearly elastic material. On the other hand, when the ZM model is used there is a fluctuation in the J-integral, especially in the transformation zone. In ZM model, free energy is not equal to strain energy, and stress is not derived from the strain energy density as in the case of an elastic material, in fact, stress is derived from the free energy of the material which is a function of strain, temperature and volume fraction of martensite [26]:

$$\boldsymbol{\sigma} = \frac{\partial \psi(\boldsymbol{\epsilon}, T, z,)}{\partial \boldsymbol{\epsilon}} \tag{6.4}$$

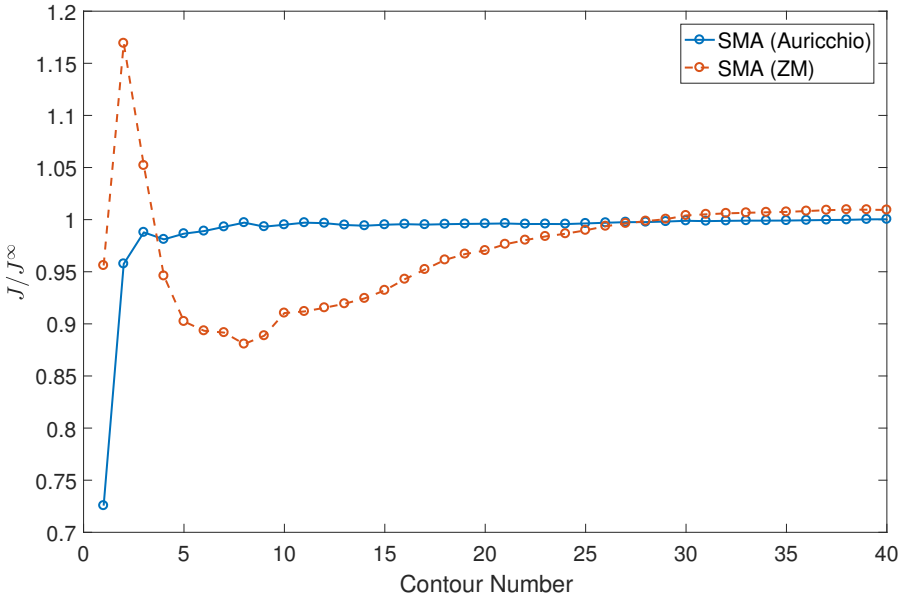

Figure 6.5. J-integral vs contour number in an SMA modeled with thermomechanically coupled ZM and uncoupled Auricchio models

It is shown that the path-dependence of J-integral in SMAs is observed when a thermomechanically coupled model is used. The effect of thermomechanical coupling on the J-integral can also be observed in elastic-plastic materials when an energy dissipation occurs in the form of heat. In order to observe this, an elastic-plastic material is modeled in ABAQUS. ABAQUS allows the user to introduce a heat generation by plastic work which is included by specifying the fraction of the rate of inelastic dissipation that appears as a heat flux per volume. In the material module of ABAQUS, stress-strain relation of the elastic-plastic material is defined using a temperature dependent data. When creating the temperature dependent data, the experimental results of Mutlu [32] in stress-strain relation of NiTi are used to approximate the thermomechanical coupling in the fictitious elastic-plastic material. In Figure 6.6, J-integral vs contour number in the elastic-plastic material is shown. Because plastic work occurs in the vicinity of crack tip, there is a fluctuation in the J-integral of the elastic-plastic material near the crack tip.

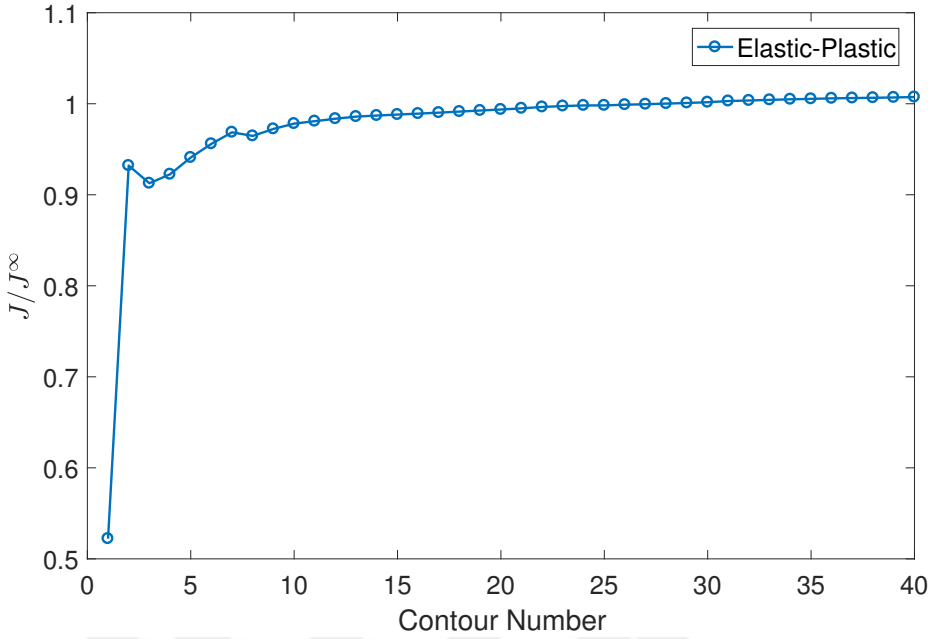

Figure 6.6. J-integral vs contour number in an elastic-plastic material

6.2. Energy Dissipation in SMAs

The first and the second laws of thermodynamics are combined to formulate the energy dissipation. The first law of thermodynamics, the energy balance, is given as follows:

$$\dot{e} = \boldsymbol{\sigma} : \dot{\boldsymbol{\epsilon}} - div\boldsymbol{q} + r \tag{6.5}$$

where e is internal energy per unit volume, $\boldsymbol{q}$ is heat flux and r is heat generation per unit volume. The second law is written as shown below:

$$\dot{s} + div(\frac{\boldsymbol{q}}{T}) - \frac{r}{T} \geq 0 \tag{6.6}$$

where s is entropy per unit volume and T is temperature. Combining the first and the second laws of thermodynamics, the Clausius-Duhem (C-D) inequality that should be

satisfied by any process is obtained:

$$\boldsymbol{\sigma} : \dot{\boldsymbol{\epsilon}} + T\dot{s} - \dot{e} - \frac{\boldsymbol{q}}{T} \nabla T \geq 0 \tag{6.7}$$

The Helmholtz free energy density which is defined as follows is used as the thermodynamic potential :

$$\psi = e - sT \tag{6.8}$$

The first law is then rewritten using the free energy, as follows:

$$T\dot{s} = \boldsymbol{\sigma} : \dot{\boldsymbol{\epsilon}} - \dot{\psi} - s\dot{T} - div\boldsymbol{q} + r \tag{6.9}$$

and the Clausius-Duhem inequality takes the following form:

$$\left(\boldsymbol{\sigma} : \dot{\boldsymbol{\epsilon}} - \dot{\psi} - s\dot{T}\right) - \frac{\boldsymbol{q}}{T} \nabla T \geq 0 \tag{6.10}$$

The left hand side of Equation 6.10 is the total dissipation with,

$$D_1 = \left(\boldsymbol{\sigma} : \dot{\boldsymbol{\epsilon}} - \dot{\psi} - s\dot{T}\right) \tag{6.11}$$

$$D_2 = -\frac{\boldsymbol{q}}{T} . \nabla T \tag{6.12}$$

where D_1 is the intrinsic dissipation and D_2 is the thermal dissipation; both dissipation terms are assumed to be positive [46]. Using Equation 6.11, the first law can be written as:

$$T\dot{s} = D_1 - div\boldsymbol{q} + r \tag{6.13}$$

and D will be used for the sake of simplicity instead of D_1, in the remaining parts of the chapter.

In the case of an SMA, state variables can be chosen as the elastic part of the strain tensor, $\boldsymbol{\epsilon}^e$, the temperature, T, and the volumetric fraction of martensite, z [47, 48]. The C-D inequality, under any loading and temperature, is satisfied with the following relations between the free energy and the state variables [49]:

$$\frac{\partial \psi}{\partial \boldsymbol{\epsilon}^{\boldsymbol{e}}} = \boldsymbol{\sigma} \quad and \quad \frac{\partial \psi}{\partial T} = -s \tag{6.14}$$

and using the chain rule, time derivative of s can be written as:

$$\dot{s} = \frac{\partial s}{\partial \epsilon^e}\frac{\partial \epsilon^e}{\partial t} + \frac{\partial s}{\partial T}\frac{\partial T}{\partial t} + \frac{\partial s}{\partial z}\frac{\partial z}{\partial t} \tag{6.15}$$

Using Equation 6.15, Equation 6.13 is written as follows:

$$-T\psi_{TT}\dot{T} - T\psi_{T\boldsymbol{\epsilon}^{\boldsymbol{e}}}\dot{\boldsymbol{\epsilon}}^{\boldsymbol{e}} - T\psi_{Tz}\dot{z} = D - div\boldsymbol{q} + r \tag{6.16}$$

In the equation above, $T\psi_{T\boldsymbol{\epsilon}^{\boldsymbol{e}}}\dot{\boldsymbol{\epsilon}}^{\boldsymbol{e}}$ is the heating due to thermoelastic effects (will be neglected), $-T\psi_{TT} = \lambda$ is the specific heat capacity per unit volume, and $T\psi_{Tz}\dot{z}$ is the heating due to phase transformation and martensite orientation [47,50]. Because phase transformation is the only source of heat generation, r is removed from the equation. As a result, Equation 6.16 is written as:

$$\lambda\dot{T} = D + T\psi_{Tz}\dot{z} - div\boldsymbol{q} \tag{6.17}$$

or the dissipation is calculated from the following equation:

$$D = \lambda\dot{T} - T\psi_{Tz}\dot{z} + div\boldsymbol{q} \tag{6.18}$$

6.3. Calculation of Energy Dissipation in a Loading-Unloading Cycle

To quantify the energy dissipation in a pseudoelastic loading-unloading cycle, a NiTi bar is modeled in ABAQUS using thermomechanically coupled ZM model. The geometry of the bar is shown in Figure 6.7; the bar is fixed from one side and 5 mm displacement is applied from the other side quasi-statically. The material properties of NiTi are shown in Table 6.1. The analysis is performed with eight-node thermally coupled brick, tri-linear elements and a uniform mesh is applied on the rod. To be able to do a lumped heat transfer analysis, conduction is removed from the model, and the convection coefficient is 0.05 W/Kmm^2 [48].

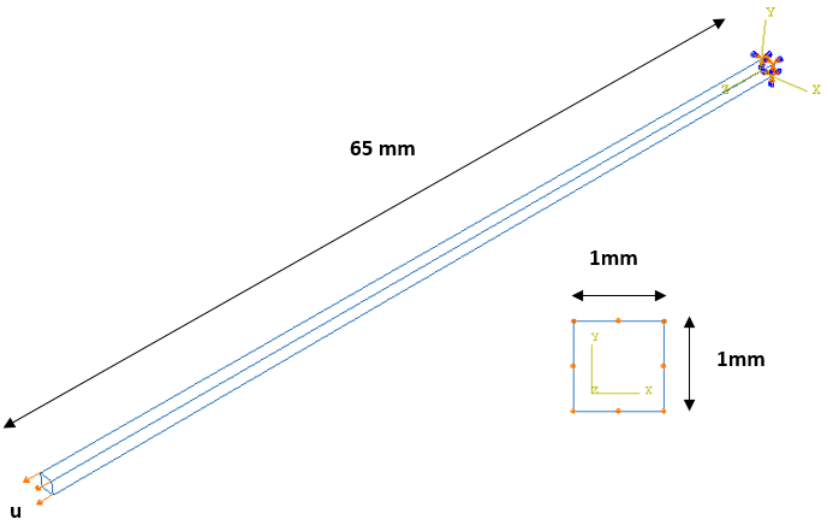

Figure 6.7. Geometry of NiTi rod modeled in ABAQUS

Table 6.1. Material properties used in the ZM model for the NiTi rod

Parameter	Value	Parameter	Value
E_A	62000 MPa	a	6.6154 MPa
E_M	45000 MPa	b	7.1745 MPa
ν	0.33	ϵ_0	0.05
Y	110 MPa	G	6.2644 MPa
α	2200 MPa	β	4400 MPa
ζ	1.1053 MPa K^{-1}	κ	1.1154 MPa
A_f^0	289.25 K	T_0	299.15 K

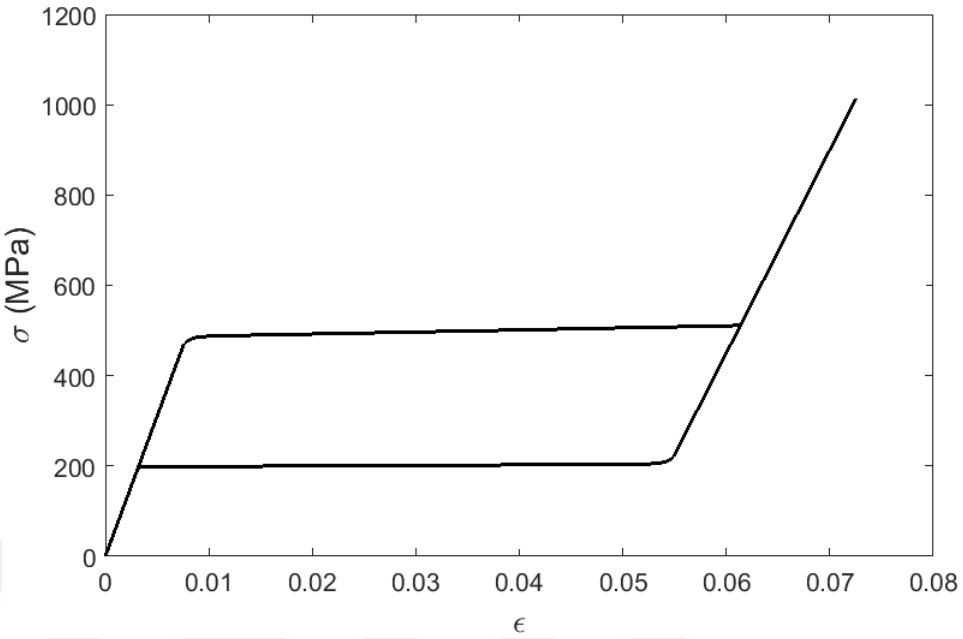

Figure 6.8. Stress-strain diagram of NiTi bar

Stress-strain diagram of the NiTi obtained from ABAQUS is shown in Figure 6.8. Total energy dissipation in a loading-unloading cycle is evaluated by integrating Equation 6.18 over time and volume. It is assumed that the amount of latent heat released during forward transformation is equal to the one absorbed during reverse transformation, therefore the integral of the latent heat term is zero. As a result, the dissipation is calculated using the following equation:

$$D_{cycle} = V_0 \int_t \lambda \frac{\partial T}{\partial t} dt + A_{surf} h \int_0^{t_f} \big(T(t) - T_\infty\big) dt \tag{6.19}$$

where V_0 is constant volume, T_∞ is ambient temperature and A_{surf} is area through which convection occurs. The first term in the right hand side of Equation 6.19 can be written as follows:

$$V_0 \int_t \lambda \frac{\partial T}{\partial t} dt = m C_p \triangle T \tag{6.20}$$

where m is mass and C_p is specific heat capacity per mass.

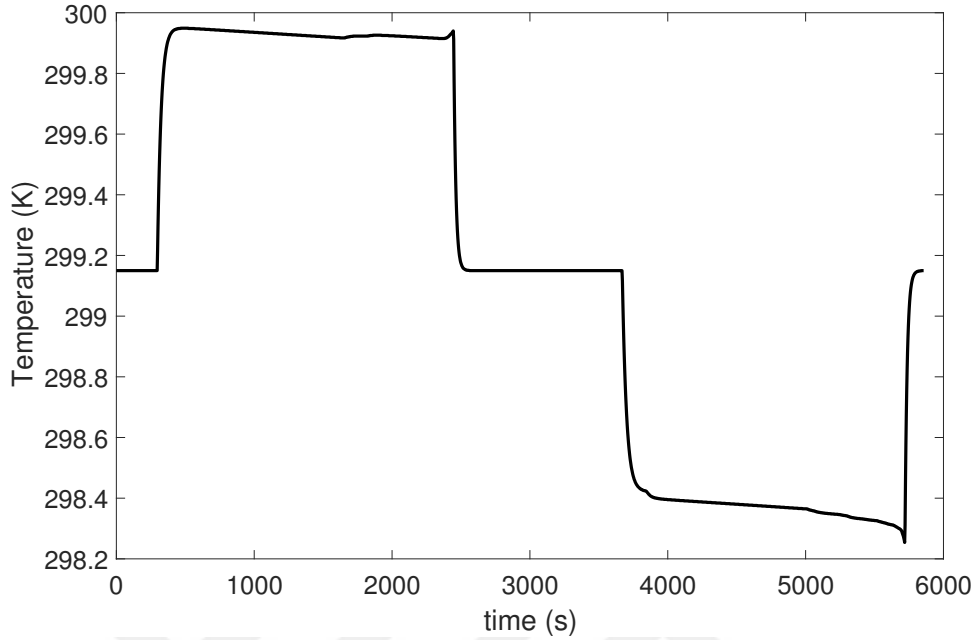

Figure 6.9. Temperature vs time

The temperature vs time plot in Figure 6.9 shows that there is no change in the temperature of the rod at the end of the cycle; the first term in Equation 6.19 is zero. Finally, using the stress, strain and temperature data obtained from ABAQUS, the total dissipation is calculated to be 960 mJ when a 2394 mJ external work is applied to the rod during loading (calculated from the area under the load-displacement curve). It is seen that there is a significant amount of dissipation in NiTi bar as a result of the pseudoelastic loading.

6.4. J-Integral and Energy Release Rate

For an elastic material, J-integral has the same meaning with the energy release rate, G, which is the change in potential energy with an incremental increase in crack area [5]:

$$J = G = -\frac{d\Pi}{dA} \tag{6.21}$$

A is the area of crack surfaces and Π is the potential energy of the cracked body. In an elastic medium, the potential energy is defined as [5]:

$$\Pi = U - F \tag{6.22}$$

where U is strain energy stored and F is external work. In the case of an elastic-plastic material, J-integral has a different interpretation because much of the strain energy stored inside the material is not released with an extension in the crack length due to plastic deformation. For an elastic-plastic material, Equation 6.21 indicates the difference in the energy absorbed between two specimens having neighboring crack sizes [5, 10, 51].

Landes and Begley [10] evaluated the J-integral experimentally: they did displacement controlled tests on same configuration of fracture specimens having different crack lengths. Under displacement controlled loading, $\Pi = U$, and U is equal to the area under a load-displacement curve. They applied the same amount of displacement on the specimens and calculated the strain energy stored by each specimen from the areas under the load-displacement curves. Strain energy per thickness (U/B) vs crack length (a) was plotted as shown in Figure 6.10. For a specific specimen, J-integral is calculated from the negative slope of the curve at the corresponding crack length.

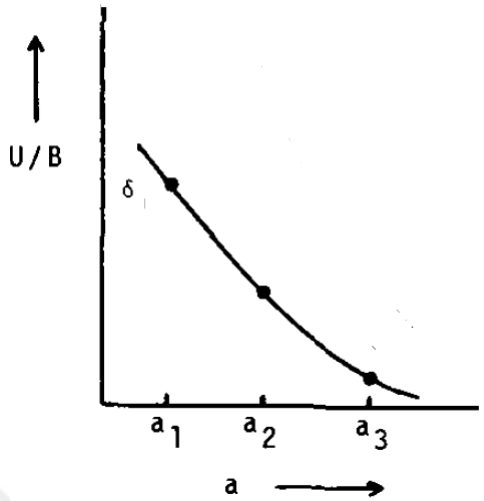

Figure 6.10. Strain energy per unit thickness vs crack length [10]

In the case of a shape memory alloy, strain energy is not the only energy which is stored inside the body. The stored (free) energy density in ZM model [26] was given in Equation 4.1. Although Equation 4.1 has temperature as a state variable, it does not represent the thermomechanical coupling correctly since the temperature was kept constant [48]. In a later work, the free energy is reformulated by Morin *et al.* [48] with the addition of a heat capacity as given below:

$$\psi^c(T, \boldsymbol{\epsilon_A}, \boldsymbol{\epsilon_M}, z, \boldsymbol{\epsilon_{tr}}) = (1-z)\big(\frac{1}{2}\boldsymbol{\epsilon_A} : \boldsymbol{K_A} : \boldsymbol{\epsilon_A}\big) + z\big[\frac{1}{2}(\boldsymbol{\epsilon_M} - \boldsymbol{\epsilon_{tr}}) : \boldsymbol{K_M} : (\boldsymbol{\epsilon_M} - \boldsymbol{\epsilon_{tr}}) + C(T)\big] + G\frac{z^2}{2} + \frac{z}{2}[\alpha z + \beta(1-z)]\big(\frac{2}{3}\boldsymbol{\epsilon_{tr}} : \boldsymbol{\epsilon_{tr}}\big) + \rho C_p\big(T - T_0 - Tln\big(\frac{T}{T_0}\big)\big) \tag{6.23}$$

where C_p is the specific heat capacity which is assumed constant for austenite and martensite, T_0 is a reference temperature and ρ is density.

Following an approach simi oflar to that Landes and Begley [10], the evaluation of J-integral is tried using the free energy density. An edge cracked SMA plate is modeled in ABAQUS using the UMAT written for the thermomechanically coupled ZM model. The geometry of the plate is shown in Figure 6.11 where $W = 100$ mm, $h = 100$ mm

and the thickness (B) is 1 mm with different crack lengths $a_1 = 30$ mm, $a_2 = 35$ mm, $a_3 = 40$ mm. The plate is loaded with 0.3 mm displacement from the top edge, and the analysis is performed with eight-node thermally coupled brick tri-linear elements with the material properties given in Table 5.4.

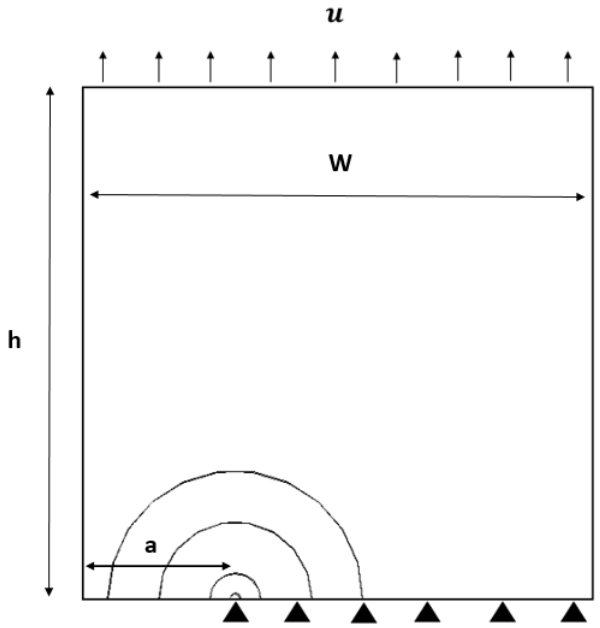

Figure 6.11. Geometry of the edge cracked specimen

All stress components (σ_{ij}), temperature, martensitic volume fraction and volume of each element are obtained from ABAQUS. The total free energy is calculated summing the free energies of each element using the following form for the free energy density: [48]:

$$\begin{aligned}\psi^c = (1-z)\big(\frac{1}{2}(El_A\boldsymbol{\sigma}:\boldsymbol{\sigma} + P_A(tr\boldsymbol{\sigma})^2\big) + z\big(\frac{1}{2}(El_M\boldsymbol{\sigma}:\boldsymbol{\sigma} + P_M(tr\boldsymbol{\sigma})^2 + C_T\big) \\ + G\frac{z^2}{2} + \frac{z}{2}[\alpha z + \beta(1-z)]\big(\frac{2}{3}\boldsymbol{\epsilon_{tr}}:\boldsymbol{\epsilon_{tr}}\big) + \rho C_p\big(T - T_0 - Tln\big(\frac{T}{T_0}\big)\big)\end{aligned} \tag{6.24}$$

where

$$
\begin{aligned}
El_A &= \frac{1+\nu}{E_A} \\
El_M &= \frac{1+\nu}{E_M} \\
P_A &= \frac{-\nu}{E_A} \\
P_M &= \frac{-\nu}{E_M}
\end{aligned}
\tag{6.25}
$$

Total free energy vs crack length is plotted in Figure 6.12, and a second order polynomial is fitted to the data. Derivative of the free energy with respect to crack surface is calculated using from the second order polynomial.

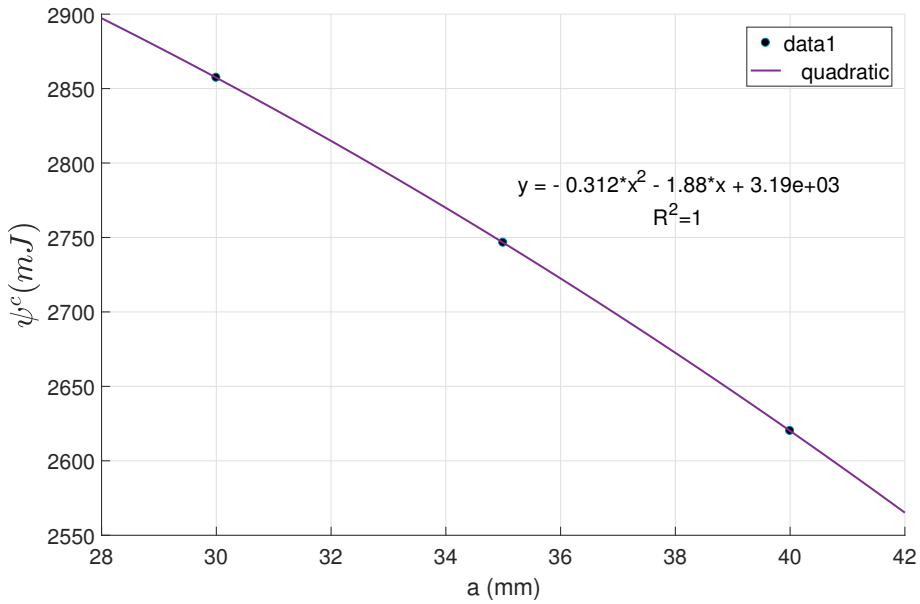

Figure 6.12. Free energy vs crack length

Table 6.2 shows the energy calculation for the edge cracked plate. The results show that transformation region along the crack tip increases with increasing crack length, and the amount of total free energy decreases. Strain energy is also calculated, and it is seen that the ratio of the strain energy to the total free energy decreases with increasing crack length. The reason behind that is the increased effect of the phase transformation.

The results of the derivative of the free energy with respect to crack area, which may be called the free energy release rate, are tabulated in Table 6.2. It is observed that the derivative, $\frac{d\psi^c}{dA}$, gives an estimation about the far-field J-integral obtained from ABAQUS. It is seen that the J-integral in SMAs has an interpretation similar to the J-integral in elastic-plastic materials, however, there is still a need for further discussion on the J-integral evaluated very close to the crack tip.

Table 6.2. Energy calculations on the edge cracked specimen with different crack lengths

	a	r_{tr}	ψ^c	U	$\frac{U}{\psi^c}$	$-\frac{d\psi^c}{dA}$	$-\frac{dU}{dA}$	J^∞
unit	mm	mm	mJ	mJ	-	N/mm	N/mm	N/mm
a_1	30	0.89	2857.3	2513.9	0.88	20.60	28.25	22.75
a_2	35	0.94	2746.5	2368.6	0.86	23.72	29.87	24.40
a_3	40	1	2620.1	2215.2	0.85	26.84	31.49	25.31

7. SUMMARY AND CONCLUSION

The aim of this thesis was to investigate the crack tip fields of pseudoelastic shape memory alloys under Mode I using similarities between martensitic transformation and plastic deformation of strain hardening materials and the martensitic transformation. Hutchinson, Rise and Rosengren independently analyzed crack tip fields of elastic-plastic materials using Ramberg-Osgood model for stress-strain relation. They derived the HRR solution based on total deformation theory of plasticity in which Rice's J-integral is used as a stress amplitude similar to stress intensity factor in LEFM. In Chapter 2, the derivation of the asymptotic stress equations of Williams (in LEFM) and HRR were summarized.

In Chapter 3, crack tip fields of an edge cracked NiTi plate under tensile loading were evaluated using the asymptotic equations of Williams and HRR. First, mechanical constants, α and n, in the Ramberg-Osgood equation were determined using the stress strain diagram. Then, distribution of each stress component around the crack tip was calculated with both asymptotic equations. Results obtained by using the asymptotic equations of Williams and HRR were compared in detail. It was observed that distribution of the asymptotic stresses around the crack tip depended on mechanical properties when HRR was used whereas there is a unique solution proposed by the asymptotic equations of Williams for a specific geometry and loading. Additionally, stresses calculated using HRR increase slowly through the crack tip while there is a substantial increase in the stress values when the equations of Williams are used. In reality, the phase transformation in SMAs limits the increase in stresses near the crack tip. From the stress analysis, it was concluded that HRR solution gives more reasonable results when compared to those of Williams.

In Chapter 4, transformation and martensitic region sizes around the crack tip were calculated analytically. For this purpose, the transformation function (F_z) developed by Zaki and Moumni [26] was used together with the asymptotic stress equations of Williams and HRR; F_z^{LEFM} and F_z^{HRR} were obtained. Both transformation function

estimations agreed with around 1 mm transformation region size on the x-axis which is experimentally observed by Haghgoyan *et al.* [8] as well. On the other hand, there was a significant difference in the estimations of full martensite region. The transformation function modified with the equations of Williams estimated almost the same size for the transformation and the full martensitic regions. A fully martensitic region was observed to be around 0.18 mm from finite elements by Haghgouyan *et al.* [8] although they could not detect it experimentally. 0.4 mm estimation obtained from HRR seems like a more reasonable result. Additionally, the size of the transformation region was also estimated using the equivalent strain distribution around the crack tip. This time, the transformation region was estimated to be around $1.9mm$ when HRR was used, and 0.7 mm from Williams. Also, the martensitic region was estimated to be around 0.3 mm using HRR and it could not be observed using the equations of Williams because strains do not change much for this type of material in the linear range.

In Chapter 5, a computational analysis was performed in ABAQUS using a UMAT subroutine written for the ZM Model. Both tensile test and fracture test simulations were performed for three types of NiTi alloys having different transformation stresses. Material properties were obtained from Mutlu [32] and Gou [33]. In order to obtain a constant temperature distribution, an excessive amount of convection coefficient was used in each model. Stress-strain diagrams were obtained from simulations of the tensile tests in ABAQUS, and corresponding mechanical constants needed for Ramberg-Osgood equation were determined by fitting a curve to stress-strain data; $n = 20$, $n = 8$ and $n = 4$ were obtained to represent the stress-strain relations of the models 1, 2, and 3 respectively. It was observed that representation of the stress-strain relation using Ramberg-Osggod relation is a better choice performed for SMAs with smaller slopes in transformation plateau, in other words, for larger n values.

For simulation of fracture tests, a compact tension (CT) specimen was modeled in ABAQUS using ZM model. The specimen was loaded in the y-direction at different load levels for each model. Crack tip fields were evaluated computationally and compared to the results obtained using the equations of Williams and HRR. Finite element results of J-integrals were found to be path-dependent; as a result an average value calculated

using the far field J-integral and the J-integral at the crack tip was used. Required stress intensity factors were calculated using $J = \frac{K_I^2}{E_A}$. The amplitude of the stress function, κ in HRR, was determined as explained in section 2.3.4. Equivalent stress distribution of each model around the crack tip was plotted using the finite element results and results obtained from asymptotic equations.

It was observed that results obtained using HRR were in good agreement with the finite element results in the transformation region. Equivalent stresses calculated using the asymptotic equations of Williams increased abruptly through the crack tip. In reality, increase in the stress is limited by the transformation mechanism in SMAs. Opening stress values ahead of crack tip were evaluated and it was seen that HRR solution matched with the finite element results in the transformation region except for the third model (Ramberg-Osgood representation of stress-strain relation of the third model was less successful than the others). Around the crack tip there is a small region of fully martensite and the asymptotic equations do not work there. Following the martensitic region, there is a transformation region in which the equations of HRR are dominant. The stress distribution obtained using the equations of Williams matched with the finite element results in the austenitic region. After transformation region, the material is in full austenitic phase and there K_I dominance is observed.

In addition to stress analysis, computational transformation region estimations were also compared to the closed form calculations obtained using transformation functions. The estimation of the transformation region from both asymptotic equations give reasonable results when compared to the finite element ones. There is a small difference between the transformation and martensitic regions when F_z^{LEFM} was used, however, the full martensitic region was better estimated when F_z^{HRR} was used.

The computational analyses of the first and the second models performed using the material properties provided by Mutlu [32] were repeated using a reasonable amount of convection coefficient to see the effect of thermomechanical coupling. The specimens were loaded according to the loading rates specified by Mutlu [32]. Because increasing temperature resulted in an increase in the transformation stresses, the transformation

region size of each model decreased. The change in the transformation region was found to be more significant in the second model subjected to a higher loading rate. The result was found as expected because the effect of themomechanical coupling is stronger in higher loading rates as it was observed by Mutlu [32].

In Chapter 6, J-integral and energy dissipation in the SMAs were studied. To understand the domain dependence of the J-integral, an edge cracked plate was loaded in ABAQUS using different material types. As expected, it was shown that J-integral around the crack tip of an elastic material is path-independent. On the other hand, J-integral was found to be path-dependent in the SMAs as a result of nonhomogeneity and the energy dissipation. It was shown that there is a significant amount of energy dissipation in a loading-unloading cycle of a pseudoelastic SMA.

The J-integral was also tried to be evaluated following the approach proposed by Landes and Begley [51] for elastic-plastic materials. Landes and Begley [51] calculated the strain energy stored inside the edge cracked specimens having neighboring crack sizes when they are subjected to the same amount of displacement loading; the slope on the strain energy vs crack length curve is equal to the J-integral. Similarly, edge cracked SMA plates with different crack lengths were modeled in ABAQUS using thermomechanically coupled ZM Model [26], they were loaded with the same amount of displacement and the energy stored inside each specimen was calculated using the free energy density of the SMAs in the ZM Model. It was observed that the slope on the free energy vs crack length curve gives an estimation about the far-field J-integral obtained from ABAQUS.

REFERENCES

1. Bhattacharya, K., *Microstructure of martensite: why it forms and how it gives rise to the shape-memory effect*, Vol. 2, Oxford University Press, 2003.

2. Lagoudas, D. C., *Shape memory alloys: modeling and engineering applications*, Springer Science & Business Media, 2008.

3. McMeeking, R. and A. Evans, "Mechanics of Transformation-Toughening in Brittle Materials", *Journal of the American Ceramic Society*, Vol. 65, No. 5, pp. 242–246, 1982.

4. Barber, J. R., *Elasticity*, Springer, 1992.

5. Anderson, T. L., *Fracture mechanics: fundamentals and applications*, CRC press, 2017.

6. Maletta, C. and F. Furgiuele, "Analytical modeling of stress-induced martensitic transformation in the crack tip region of nickel–titanium alloys", *Acta Materialia*, Vol. 58, No. 1, pp. 92–101, 2010.

7. Hutchinson, J., "Singular behaviour at the end of a tensile crack in a hardening material", *Journal of the Mechanics and Physics of Solids*, Vol. 16, No. 1, pp. 13–31, 1968.

8. Haghgouyan, B., N. Shafaghi, C. C. Aydıner and G. Anlas, "Experimental and computational investigation of the effect of phase transformation on fracture parameters of an SMA", *Smart Materials and Structures*, Vol. 25, No. 7, p. 075010, 2016.

9. Dowling, N. E., *Mechanical behavior of materials: engineering methods for deformation, fracture, and fatigue*, Pearson, 2012.

10. Bucci, R., P. Paris, J. Landes and J. Rice, "J integral estimation procedures", *Fracture Toughness: Part II*, ASTM International, 1972.

11. Christian, J. W., *The theory of transformations in metals and alloys*, Newnes, 2002.

12. Otsuka, K. and C. M. Wayman, *Shape memory materials*, Cambridge university press, 1999.

13. Patoor, E., D. C. Lagoudas, P. B. Entchev, L. C. Brinson and X. Gao, "Shape memory alloys, Part I: General properties and modeling of single crystals", *Mechanics of materials*, Vol. 38, No. 5, pp. 391–429, 2006.

14. Williams, M., "On the Stress Distribution at the Base of a Stationary Crack", *Journal of Applied Mechanics*, Vol. 24, No. 1, pp. 109–114, 1957.

15. Maletta, C., "A novel fracture mechanics approach for shape memory alloys with trilinear stress–strain behavior", *International journal of fracture*, pp. 1–13, 2012.

16. Maletta, C. and F. Furgiuele, "Fracture control parameters for NiTi based shape memory alloys", *International Journal of Solids and Structures*, Vol. 48, No. 11, pp. 1658–1664, 2011.

17. Birman, V., "On mode I fracture of shape memory alloy plates", *Smart materials and structures*, Vol. 7, No. 4, p. 433, 1998.

18. Yi, S. and S. Gao, "Fracture toughening mechanism of shape memory alloys due to martensite transformation", *International journal of solids and structures*, Vol. 37, No. 38, pp. 5315–5327, 2000.

19. Freed, Y. and L. Banks-Sills, "Crack growth resistance of shape memory alloys by means of a cohesive zone model", *Journal of the Mechanics and Physics of Solids*, Vol. 55, No. 10, pp. 2157–2180, 2007.

20. Baxevanis, T. and D. Lagoudas, "A mode I fracture analysis of a center-cracked infinite shape memory alloy plate under plane stress", *International journal of fracture*, pp. 1–16, 2012.

21. Wang, G., "A finite element analysis of evolution of stress–strain and martensite transformation in front of a notch in shape memory alloy NiTi", *Materials Science and Engineering: A*, Vol. 460, pp. 383–391, 2007.

22. Baxevanis, T., Y. Chemisky and D. Lagoudas, "Finite element analysis of the plane strain crack-tip mechanical fields in pseudoelastic shape memory alloys", *Smart Materials and Structures*, Vol. 21, No. 9, p. 094012, 2012.

23. Rice, J. R. *et al.*, "A path independent integral and the approximate analysis of strain concentration by notches and cracks", ASME, 1968.

24. Falvo, A., F. Furgiuele, A. Leonardi and C. Maletta, "Stress-induced martensitic transformation in the crack tip region of a NiTi alloy", *Journal of materials engineering and performance*, Vol. 18, No. 5-6, pp. 679–685, 2009.

25. Hazar, S., G. Anlas and Z. Moumni, "Evaluation of transformation region around crack tip in shape memory alloys", *International Journal of Fracture*, Vol. 197, No. 1, pp. 99–110, 2016.

26. Zaki, W. and Z. Moumni, "A three-dimensional model of the thermomechanical behavior of shape memory alloys", *Journal of the Mechanics and Physics of Solids*, Vol. 55, No. 11, pp. 2455–2490, 2007.

27. Wang, X., B. Xu, Z. Yue and X. Tong, "Fracture behavior of the compact tension specimens in NiTi shape memory alloys", *Materials Science and Engineering: A*, Vol. 485, No. 1, pp. 14–19, 2008.

28. Standard, A., "E399, Standard Test Method for Linear-Elastic Plane-Strain Fracture Toughness KIC of Metallic Materials", *ASTM book of standards, West Con-*

shohocken, PA. ASTM International, 2012.

29. Daly, S., A. Miller, G. Ravichandran and K. Bhattacharya, "An experimental investigation of crack initiation in thin sheets of nitinol", *Acta Materialia*, Vol. 55, No. 18, pp. 6322–6330, 2007.

30. Robertson, S., A. Mehta, A. Pelton and R. Ritchie, "Evolution of crack-tip transformation zones in superelastic Nitinol subjected to in situ fatigue: A fracture mechanics and synchrotron X-ray microdiffraction analysis", *Acta Materialia*, Vol. 55, No. 18, pp. 6198–6207, 2007.

31. Gollerthan, S., D. Herberg, A. Baruj and G. Eggeler, "Compact tension testing of martensitic/pseudoplastic NiTi shape memory alloys", *Materials Science and Engineering: A*, Vol. 481, pp. 156–159, 2008.

32. Mutlu, F., *Effect of loading rate on fracture of NiTi*, Master's Thesis, Bogazici University, 2016.

33. Gu, X., W. Zaki, C. Morin, Z. Moumni and W. Zhang, "Time integration and assessment of a model for shape memory alloys considering multiaxial nonproportional loading cases", *International Journal of Solids and Structures*, Vol. 54, pp. 82–99, 2015.

34. Williams, M., "Stress singularities resulting from various boundary conditions in angular corners of plates in extension", *Journal of applied mechanics*, Vol. 19, No. 4, pp. 526–528, 1952.

35. Lubliner, J., *Plasticity theory*, Courier Corporation, 2008.

36. Rice, J. and G. F. Rosengren, "Plane strain deformation near a crack tip in a power-law hardening material", *Journal of the Mechanics and Physics of Solids*, Vol. 16, No. 1, pp. 1–12, 1968.

37. Lambros, J. and G. Anlas, "Crack Initiation in Functionally Graded Materials Under Mixed Mode Loading: Experiments and Simulations", *Urbana*, Vol. 51, p. 61801.

38. Jones, R. M., *Deformation theory of plasticity*, Bull Ridge Corporation, 2009.

39. Hutchinson, J., "Fundamentals of the phenomenological theory of nonlinear fracture mechanics", *Journal of Applied Mechanics*, Vol. 50, No. 4b, pp. 1042–1051, 1983.

40. Maletta, C. and F. Furgiuele, "1D Phenomenological Modeling of Shape Memory and Pseudoelasticity in NiTi Alloys", *Smart Actuation and Sensing Systems-Recent Advances and Future Challenges*, InTech, 2012.

41. Qiu, S., B. Clausen, S. Padula, R. Noebe and R. Vaidyanathan, "On elastic moduli and elastic anisotropy in polycrystalline martensitic NiTi", *Acta Materialia*, Vol. 59, No. 13, pp. 5055–5066, 2011.

42. Bewerse, C., K. R. Gall, G. J. McFarland, P. Zhu and L. C. Brinson, "Local and global strains and strain ratios in shape memory alloys using digital imagecorrelation", *Materials Science and Engineering: A*, Vol. 568, pp. 134–142, 2013.

43. ABAQUS, V., "6.14 Documentation", *Dassault Systemes Simulia Corporation*, 2014.

44. Hazar, S., *Theoretical and numerical analysis of fracture of shape memory alloys*, Ph.D. Thesis, Bogazici University, 2014.

45. Auricchio, F., R. L. Taylor and J. Lubliner, "Shape-memory alloys: macromodelling and numerical simulations of the superelastic behavior", *Computer methods in applied mechanics and engineering*, Vol. 146, No. 3-4, pp. 281–312, 1997.

46. Rosakis, P., A. Rosakis, G. Ravichandran and J. Hodowany, "A thermodynamic

internal variable model for the partition of plastic work into heat and stored energy in metals", *Journal of the Mechanics and Physics of Solids*, Vol. 48, No. 3, pp. 581–607, 2000.

47. Zhang, Y., Y. You, Z. Moumni, G. Anlas, J. Zhu and W. Zhang, "Experimental and theoretical investigation of the frequency effect on low cycle fatigue of shape memory alloys", *International Journal of Plasticity*, Vol. 90, pp. 1–30, 2017.

48. Morin, C., *A comprehensive approach for fatigue analysis of shape memory alloys*, Ph.D. Thesis, Ecole Polytechnique, 2011.

49. Zaki, W., *Comportement thermo-mécanique des matériaux à mémoire de forme: modélisation macroscopique, chargement cyclique et fatigue*, Ph.D. Thesis, Ecole Polytechnique, 2006.

50. Morin, C., Z. Moumni and W. Zaki, "A constitutive model for shape memory alloys accounting for thermomechanical coupling", *International Journal of Plasticity*, Vol. 27, No. 5, pp. 748–767, 2011.

51. Begley, J. and J. Landes, "The J integral as a fracture criterion", *Fracture Toughness: Part II*, ASTM International, 1972.

52. Ugural, A. C. and S. K. Fenster, *Advanced strength and applied elasticity*, Pearson Education, 2003.

APPENDIX A: STRESS FUNCTION FORMULATION

In the absence of body forces, equilibrium equations in Cartesian coordinates are as follows:

$$\begin{aligned} \frac{\partial \sigma_{xx}}{\partial x} + \frac{\partial \tau_{xy}}{\partial y} &= 0 \\ \frac{\partial \tau_{yx}}{\partial x} + \frac{\partial \sigma_{yy}}{\partial y} &= 0 \end{aligned} \tag{A.1}$$

which are identically satisfied by the stress function related to stresses as follows:

$$\begin{aligned} \sigma_{xx} &= \frac{\partial^2 \phi}{\partial y^2} \\ \sigma_{yy} &= \frac{\partial^2 \phi}{\partial x^2} \\ \sigma_{xy} &= -\frac{\partial^2 \phi}{\partial x \partial y} \end{aligned} \tag{A.2}$$

$\phi(x, y)$ is the Airy stress function introduced by G. B. Airy. It is a scalar function which enables the solution of two dimensional problems in elasticity [52].

For 2D problems, compatibility equation is:

$$\frac{\partial^2 \epsilon_{xx}}{\partial y^2} + \frac{\partial^2 \epsilon_{yy}}{\partial x^2} = \frac{\partial^2 \gamma_{xy}}{\partial x \partial y} \tag{A.3}$$

and the constitutive relations for plane stress are given as follws:

$$\begin{aligned} \epsilon_{xx} = \epsilon_{xx}(x, y) &= \frac{1}{E}[\sigma_{xx} - \nu \sigma_{yy}] \\ \epsilon_{yy} = \epsilon_{yy}(x, y) &= \frac{1}{E}[\sigma_{yy} - \nu \sigma_{xx}] \\ \gamma_{xy} = \gamma_{xy}(x, y) &= \frac{1}{\mu}\sigma_{xy} \\ \epsilon_{zz} &= -\frac{\nu}{E}(\sigma_{xx} + \sigma_{yy}) \end{aligned} \tag{A.4}$$

If the constitutive equations for plane stress are submitted into the compatibility equation, the following equation is obtained:

$$\frac{\mu}{E}(\frac{\partial^2\sigma_{xx}}{\partial y^2}+\frac{\partial^2\sigma_{yy}}{\partial x^2})-\frac{\mu\nu}{E}(\frac{\partial^2\sigma_{yy}}{\partial y^2}+\frac{\partial^2\sigma_{xx}}{\partial x^2})=\frac{\partial^2\sigma_{xy}}{\partial x\partial y} \tag{A.5}$$

Differentiating equilibrium equations with respect to x and y respectively gives:

$$\frac{\partial^2\sigma_{xx}}{\partial x^2}+\frac{\partial^2\sigma_{xy}}{\partial x\partial y}=0 \tag{A.6}$$

$$\frac{\partial^2\sigma_{xy}}{\partial x\partial y}+\frac{\partial^2\sigma_{yy}}{\partial y^2}=0 \tag{A.7}$$

and summing the two equations above:

$$2\frac{\partial^2\sigma_{xy}}{\partial x\partial y}=-\frac{\partial^2\sigma_{xx}}{\partial x^2}-\frac{\partial^2\sigma_{yy}}{\partial y^2} \tag{A.8}$$

is obtained. Submitting Equation A.8 into the right hand side of Enq. A.5 and simplifying:

$$\nabla^2\left(\sigma_{xx}+\sigma_{yy}\right)=0 \tag{A.9}$$

is obtained. Now, stresses are written in terms of stress function and it gives:

$$\frac{\partial^4\phi}{\partial x^4}+2\frac{\partial^4\phi}{\partial x^2\partial y^2}+\frac{\partial^4\phi}{\partial y^4}=0 \tag{A.10}$$

or

$$\nabla^4\phi=0 \tag{A.11}$$

According to Equation A.11, stress function satisfies the biharmonic equation. In polar coordinates it is written as:

$$\nabla^4\phi = \left(\frac{\partial^2}{\partial r^2} + \frac{1}{r}\frac{\partial}{\partial r} + \frac{1}{r^2}\frac{\partial^2}{\partial \theta^2}\right)\left(\frac{\partial^2\phi}{\partial r^2} + \frac{1}{r}\frac{\partial\phi}{\partial r} + \frac{1}{r^2}\frac{\partial^2\phi}{\partial \theta^2}\right) = 0 \tag{A.12}$$